

Micromagnetic Sensors and  
Dirac Fermions in HgTe Heterostructures



Dissertation

zur Erlangung des  
naturwissenschaftlichen Doktorgrades  
der Bayerischen Julius-Maximilians-Universität Würzburg

vorgelegt von  
Bastian Büttner  
aus Bad Neustadt a. d. Saale.

Würzburg 2012

Eingereicht am: 16.03.2012

bei der Fakultät für Physik und Astronomie

Gutachter der Dissertation:

1. Gutachter: Prof. Dr. L. W. Molenkamp
2. Gutachter: Prof. Dr. L. Worschech

Prüfer im Promotionskolloquium:

1. Prüfer: Prof. Dr. L. W. Molenkamp
2. Prüfer: Prof. Dr. L. Worschech
3. Prüfer: Prof. Dr. B. Trauzettel

Tag des Promotionskolloquiums: 06.08.2012

Doktorurkunde ausgehändigt am: ...

# Contents

<b>Zusammenfassung</b>	<b>1</b>
<b>Summary</b>	<b>4</b>
<b>1 Introduction</b>	<b>9</b>
<b>2 Micromagnetic sensors</b>	<b>13</b>
2.1 Micromagnetism . . . . .	16
2.1.1 Ferromagnetism . . . . .	16
2.1.2 Magnetization and Hysteresis . . . . .	18
2.1.3 Magnetic Energies . . . . .	19
2.1.4 Domains and Domain Walls . . . . .	22
2.1.5 Domains in an External Field . . . . .	24
2.1.6 Stray Field of a Rectangular Bar . . . . .	25
2.1.7 Stray Field of a Particle . . . . .	30
2.2 Micro-Hall Magnetometry . . . . .	32
2.2.1 2D Electron Gas . . . . .	32
2.2.2 Electronic Transport . . . . .	36
2.2.3 Quantum Hall Effect . . . . .	40
2.2.4 Local Hall Effect . . . . .	45
2.2.5 Fabrication . . . . .	52
2.2.6 Experimental Setup . . . . .	55
2.2.7 Measurements and Discussion . . . . .	58
2.3 Micro-SQUID Sensors . . . . .	72
2.3.1 Basics of Micro-SQUID Operation . . . . .	73
2.3.2 Fabrication of Micro-SQUIDs . . . . .	81
2.3.3 Measurement Setup . . . . .	83
2.3.4 Resolution of a Micro-SQUID . . . . .	86
2.3.5 Investigation of a Nanomagnet . . . . .	88
2.4 Conclusion . . . . .	90

<b>3</b>	<b>Dirac Fermions in HgTe Heterostructures</b>	<b>93</b>
3.1	Properties of (Hg,Cd)Te Quantum Wells . . . . .	93
3.2	Single Valley Dirac Fermions in Zero-Gap HgTe Quantum Wells . . . . .	99
3.2.1	Energy Dispersion for $\mathcal{M} = 0$ . . . . .	99
3.2.2	Fabrication and Measurement Setup . . . . .	101
3.2.3	Identification of the Energy Gap Using the Quantum Hall Effect . . . . .	102
3.2.4	Characterization of the Zero-Gap Sample . . . . .	107
3.2.5	Measurements Without Magnetic Field . . . . .	113
3.3	Weak Anti-Localization Effect in HgTe Nanostructures . . . . .	116
3.3.1	One-Dimensional Conductance . . . . .	116
3.3.2	Parabolic Background . . . . .	117
3.3.3	Universal Conductance Fluctuations . . . . .	120
3.3.4	Localization . . . . .	124
3.3.5	WAL and UCF for an Ensemble on Inverted HgTe QW . . . . .	134
3.3.6	WAL and UCF for Zero Rashba . . . . .	138
3.3.7	WAL for Normal Quantum Well . . . . .	141
3.3.8	Conclusion . . . . .	142
<b>A</b>	<b>Fabrication Processes</b>	<b>145</b>
A.1	Macro-Hall Bar on InAs 2DEG . . . . .	145
A.2	Micro-Hall Bar on InAs 2DEG . . . . .	146
A.3	Macro-Hall Bar on HgTe 2DEG . . . . .	148
A.4	Micro-Hall Bar on HgTe 2DEG . . . . .	149
A.5	Micro-SQUID Fabrication . . . . .	150
<b>B</b>	<b>Substrates and Samples</b>	<b>153</b>
<b>C</b>	<b>Magnetic Materials</b>	<b>155</b>
	<b>Abbreviations</b>	<b>156</b>
	<b>Bibliography</b>	<b>158</b>
	<b>List of Figures</b>	<b>167</b>
	<b>List of Tables</b>	<b>169</b>
	<b>Publications</b>	<b>170</b>

# Zusammenfassung

Im Rahmen dieser Arbeit wurden zwei Themenbereiche bearbeitet: die Untersuchung von mikromagnetischen Sensoren und der Transport von massiven und masselosen Dirac Fermionen in HgTe Quantenwällen.

Für die Untersuchung von lokalisierten, inhomogenen Magnetfeldern wurde die Herstellung und Charakterisierung von zwei unterschiedlichen nicht-invasiven und hochempfindlichen Sensoren am Lehrstuhl für Experimentelle Physik III der Universität Würzburg etabliert. Der erste Sensor beruht auf der noch recht jungen Methode der Mikro-Hall-Magnetometrie. Die dafür notwendigen Halbleiterbauteile (Hallkreuzstrukturen) wurden mit höchstauflösender Elektronenstrahlithografie auf Basis von zwei verschiedenen zweidimensionalen Elektronengasen (2DEGs) hergestellt, genauer InAs/(Al,Ga)Sb- und HgTe/(Hg,Cd)Te- Halbleiterheterostrukturen. Nachfolgend wurden deren Charakteristika auf zwei verschiedene Arten untersucht. Messungen in homogenen Magnetfeldern dienen der Charakterisierung der Sensoren, während die Untersuchung von künstlich hergestellten sub-Mikrometermagneten die Eignung der Bauteile für die Detektion neuartiger magnetischer Materialien auf der Nanoskala (z.B. Nanodrähte) nachweist. Systematische Messungen an Magneten unterschiedlicher Ausdehnungen stimmen mit theoretischen Vorausbetrachtungen in Bezug auf Einzeldomänenteilchen und Formanisotropie überein.

Die höchste Empfindlichkeit für stark lokalisierte Magnetfelder wurde mit einem  $(200 \cdot 200) \text{ nm}^2$  großen Hallkreuz - hergestellt aus einem oberflächennahen, hochbeweglichen HgTe 2DEG - bei einer Temperatur von 4.2 K erreicht. Obwohl die Feldauflösung lediglich  $\delta B \approx 100 \mu\text{T}$  betrug, konnte auf Grund der Miniaturisierung der Sensorfläche eine beein-

druckende Flusssensitivität von  $\delta\Phi \approx 2 \cdot 10^{-3} \Phi_0$  erreicht werden, wobei  $\Phi_0 = h/2e$  das Flussquant darstellt. Wenn man diese Auflösung in Bezug auf die Magnetisierung betrachtet, ermöglicht der Sensor die Detektion von Magnetisierungsänderungen eines Teilchens auf der Mitte des Sensors in Höhe von  $\delta M \approx 10^2 \mu_B$  mit dem magnetischen Moment eines Elektrons, dem Bohrschen Magneton  $\mu_B$ .

Die weiteren Untersuchungen eines Permalloy-Nanomagneten mit einer Querschnittsfläche von  $(100 \cdot 20) \text{ nm}^2$  bestätigt die erwartete Auflösungsfähigkeit, die aus dem Rauschen des Sensors hervorgeht. Das beobachtete hohe Signal/Rausch-Verhältnis attestiert, dass die Detektionsgrenze eines Magneten gleichen Materials mit quadratischer Querschnittsfläche bei einer Kantenlänge von 3.3 nm liegt. Weiterhin konnte die Einsatzfähigkeit des Bauteils in einem breiten Temperaturbereich ( $T = \text{mK} \dots > 200 \text{ K}$ ) und bei hohen Magnetfeldern bestätigt werden.

Bei dem zweiten mikromagnetischen Sensor handelt es sich um das Mikro-SQUID (Mikro-Superconducting-QUantum-Interference-Device) basierend auf Niob. Die Sensorfläche der in dieser Arbeit hergestellten Mikro-SQUIDs betrug typischerweise  $(1.0 \cdot 1.0) \mu\text{m}^2$  mit Einschnürungen im Bereich von 20 nm.

Die Charakterisierung dieses Bauteils zeigt eine beeindruckende Magnetfeldauflösung von  $\delta B < 1 \mu\text{T}$ , besonders hinsichtlich der minimalen Ausdehnung des Bauteils. Obwohl die Sensorfläche 25 mal größer als die des Mikro-Hallsensors war, wurde so eine höhere Flusssensitivität von  $\delta\Phi \approx 5 \cdot 10^{-4} \Phi_0$  und eine ähnliche magnetische Momentauflösung von  $\delta M \approx 10^2 \mu_B$  erreicht. Des weiteren konnte mit der Einbringung eines ellipsoidalen Permalloy-Magneten (Achsen: 200 und 400 nm, Dicke: 30 nm) die Eignung zur Detektion winziger lokaler Magnetfelder konkretisiert werden.

Im zweiten Teil der Arbeit sind die besonderen Transporteigenschaften von HgTe Quantenwällen, die auf dem linearen Anteil in der Bandstruktur beruhen, untersucht worden. Das System kann mit einem Dirac Hamiltonian beschrieben werden, dessen Diracmasse durch Variation der Quantenwalldicke beeinflusst werden kann.

Im Verlauf der Arbeit konnte durch Herstellung und Charakterisierung einer system-

atischen Serie von Substraten ein System mit verschwindender Diracmasse (Energilücke gleich 0) bestätigt werden. Diese Halbleiterheterostruktur gleicht damit Graphen (eine Monolage von Graphit), mit dem Unterschied, dass es in der Brillouinzone nur eine Elektronensenke aufweist und demzufolge keine störende Intervalley-Streuung auftreten kann. Die Existenz dieses Systems konnte durch die Übereinstimmung von Vorhersagen aus theoretischen Bandstrukturrechnungen mit dem Experiment (Verlauf der Landauniveaus, Leitfähigkeit) bestätigt werden. Außerdem konnte die Besonderheit der Bandstruktur - der Übergang von linearem zu quadratischem Charakter - anhand der Plateauweiten im Quanten-Hall-Effekt veranschaulicht werden.

Im weiteren Verlauf wurde der Transport von "massiven" Dirac Fermionen (mit einer endlichen Diracmasse) untersucht. Im Besonderen führt der beschreibende Dirac Hamiltonian in Abhängigkeit von der Diracmasse zu schwachen Lokalisierungseffekten, die bis dato noch nicht beobachtet wurden und im Vergleich zu typischen Mechanismen bis zu weit höheren Temperaturen überleben.





# Summary

Within the scope of this thesis two main topics have been investigated: the examination of micromagnetic sensors and transport of massive and massless Dirac fermions in HgTe quantum wells.

For the investigation of localized, inhomogeneous magnetic fields, the fabrication and characterization of two different non-invasive and ultra sensitive sensors has been established at the chair "Experimentelle Physik" of the University of Würzburg.

The first sensor is based on the young technique named micro-Hall magnetometry. The necessary semiconductor devices (Hall cross structures) were fabricated by high-resolution electron beam lithography based on two different two dimensional electron gases (2DEGs), namely InAs/(Al,Ga)Sb- and HgTe/(Hg,Cd)Te- heterostructures. The characteristics have been examined in two different ways. Measurements in homogeneous magnetic fields served for characterization of the sensors, whereas the investigation of artificially produced sub- $\mu\text{m}$  magnets substantiates the suitability of the devices for the study of novel nanoscale magnetic materials (e.g. nanowires). Systematic experiments with various magnets are in accordance with the theory of single-domain particles and anisotropic behavior due to shapes with high aspect ratio.

The highest sensitivity for strongly localized fields was obtained at  $T = 4.2$  K for a  $(200 \cdot 200)$  nm<sup>2</sup> Hall cross - made from shallow, high mobility HgTe 2DEG. Although the field resolution was merely  $\delta B \approx 100 \mu\text{T}$ , the nanoscale sensor size yields an outstanding flux resolution of  $\delta\Phi = 2 \cdot 10^{-3} \Phi_0$ , where  $\Phi_0 = h/2e$  is the flux quantum. Translating this result in terms of magnetic moment, the sensitivity allows for the detection of magnetization changes of a particle centered on top of the sensor as low as  $\delta M \approx 10^2 \mu_B$ , with the

magnetic moment of a single electron  $\mu_B$ , the Bohr magneton.

The further examination of a permalloy nanomagnet with a cross-section of  $(100 \cdot 20) \text{ nm}^2$  confirms the expected resolution ability, extracted from the noise of the sensor. The observed high signal-to-noise ratio validates the detection limit of this sensor in terms of geometry. This would be reached for a magnet (same material) with quadratic cross-section for an edge length of 3.3 nm. Moreover, the feasibility of this sensor for operation in a wide temperature range ( $T = mK \dots > 200 K$ ) and high magnetic fields has been confirmed.

The second micromagnetic sensor is the micro-SQUID (micro-**S**uperconducting-**Q**uantum-**I**nterference-**D**evice) based on niobium. The typical sensor area of the devices built in this work was  $(1.0 \cdot 1.0) \mu\text{m}^2$ , with constrictions of about 20 nm. The characterization of this device demonstrates an amazing field sensitivity (regarding its size) of  $\delta B < 1 \mu\text{T}$ . Even though the sensor was 25 times larger than the best micro-Hall sensor, it provided an excellent flux resolution in the order of  $\delta\Phi \approx 5 \cdot 10^{-4} \Phi_0$  and a similar magnetic moment resolution of  $\delta M \approx 10^2 \mu_B$ . Furthermore, the introduction of an ellipsoidal permalloy magnet (axes: 200 nm and 400 nm, thickness 30 nm) substantiates the suitability for the detection of minuscule, localized magnetic fields.

The second part of the thesis deals with the peculiar transport properties of HgTe quantum wells. These rely on the linear contribution to the band structure inherent to the heterostructure. Therefore the system can be described by an effective Dirac Hamiltonian, whose Dirac mass is tunable by the variation of the quantum well thickness.

By fabrication and characterization of a systematical series of substrates, a system with vanishing Dirac mass (zero energy gap) has been confirmed. This heterostructure therefore resembles graphene (a monolayer of graphite), with the difference of exhibiting only one valley in the energy dispersion of the Brillouin zone. Thus parasitical intervalley scattering cannot occur. The existence of this system has been proven by the agreement of theoretical predictions, based on widely accepted band structure calculations with the experiment (Landau level dispersion, conductivity). Furthermore, another particularity of the band structure - the transition from linear to parabolic character - has been illus-

---

trated by the widths of the plateaus in the quantum Hall effect.

Finally, the transport of "massive" Dirac fermions (with finite Dirac mass) is investigated. In particular the describing Dirac Hamiltonian induces weak localization effects depending on the Dirac mass. This mechanism has not been observed to date, and survives in higher temperatures compared to typical localization mechanisms.



# Chapter 1

## Introduction

In recent decades, processing and storage of information has become a growing part of everyday life. That is why ferromagnetism on the nanoscale and novel transport phenomena are the key for the development of future technologies.

In view of storage the increase of storage density is necessary to suffice the exploding amount of information that flows between humans. And that is not only due to increased knowledge of mankind which obviously grows exponentially with world population but, moreover, rather because of the transition to a globalized world. An integral part is the internet that serves for communication and to share information. This led to the revolution of the so called social media. This might look simple at first sight. But recent years have shown that the possibility for news and knowledge to spread freely can support independent, responsible and liberal thinking - and, hopefully, a better world for everyone.

Associated with higher density is the reduction of dimensions. Therefore the understanding of matter on the nanoscale, alongside the ability to predict and control, is of utmost importance to succeed. Since the main storage medium up to now is based on ferromagnetic materials, this goal can be achieved by sensing miniaturized magnets while applying external forces. That is the motivation for the first part of this thesis - the development of micromagnetic sensors that facilitates insights into the magnetic properties of tiny magnetic particles.

This chapter is organized as follows: After a discussion of ferromagnetism on the

micrometer scale the up-to-date two most sensitive non-invasive micromagnetic sensors - the micro-Hall magnetometry and the micro-SQUIDs will be presented. Thereby the sections for both sensors first start with the underlying theory that will be summarized in order to understand the peculiarities of each approach. Subsequently, the fabrication of the sensors is dealt with as they have been established during this work. Thus produced devices are then examined in various measurements proving theoretical predictions and calculating the sensitivity limits of each device. In conclusion, a comparison of the two methods will be given, discussing the pros and cons.

But information not only needs to be stored, it must also be processed. That takes place in computers, smartphones, cars and many more places. Electronics is currently conquering everyone's daily life.

The driving force for the underlying semiconductor physics has been Moore's law since it was published by Gordon E. Moore [Moo65] - even though (back then) he did not know which dimensions his publication would take. However, the shrinking of semiconductor devices will foreseeably reach a limit in atomic dimensions (even though shrinking survived much longer as expected). That will be the end of the evolution of highly perfected silicon transistors. Thus a revolution, a different approach, needs to be found and is the driving force for the research of novel transport phenomena.

Lately, the most famous example has been graphene (a sheet of graphite) whose discoverers only recently have been awarded by the Nobel Prize [GNY<sup>+</sup>07]. Unfortunately, its lack of a band gap is a hindrance for the development of economical power-saving devices.

Another uprising class of materials are topological insulators. They behave as an insulator in the bulk while exhibiting conducting surface states. This new class of materials may in future find uses in technological applications (e.g. spintronics). The quantum spin hall effect predicted by [BHZ06] and experimentally measured on HgTe [KBMH08] boasts dissipationless current and is the two dimensional version of topological insulators. Therefore the high quality system of HgTe quantum wells is the ideal model system to investigate novel transport phenomena that may later be available in high quality topo-

logical insulators.

That is why the transport properties in this material system are investigated in the second part of this thesis. The outline of this part is as follows. In the beginning the band structure which is the reason for the unique transport properties will be described. Then, by tuning the band gap, a zero-gap quantum well has been fabricated and proved by experiment. Concluding the thesis, measurements of the weak anti-localization effect arising in this material by a novel mechanism will be discussed.





## Chapter 2

# Micromagnetic sensors

Ferromagnetism has been known to mankind for a long time. Chinese drawings from <2000 BC exist that confirm their knowledge about some compass-like instrument. Later the Greeks found minerals that had an attracting force to iron. A name was finally given to that kind of force since these minerals were found close to the city Magnesia in what is today Turkey. It took a long time until 1000 AD for this phenomenon to be used in a real application [Sch96], when the first magnetic needle was used as a compass. An invention which spread very fast and revolutionized seafaring.

Nowadays magnetism is used extensively by everyone in the whole world. Especially in data storage, magnetism is the ultimate basis for the storage of information. IBM started out in 1952 with data tapes offering 1.4 MB on a 720 m long tape, followed in 1956 by the first hard disc storage RAMAC 305 with a data density of 100 bits/inch [ND57]. To date the evolution of storage surpassed even the Moore's law for integrated circuits that foresee a doubling of storage density every 18 months. The orientation of the magnetization serves as the information where parallel (antiparallel) to a preferential direction is the bit 1 (or 0). The steady decrease of the size of magnetic bits enabled to suffice the increasing demand of mass storage.

The revolution in spintronics took place in 1988 when Grünberg and Fert simultaneously discovered the giant-magnetoresistance-effect GMR [BBF<sup>+</sup>88, BGS<sup>+</sup>89]. It appears in a ferromagnetic multilayer with a nonmagnetic metal interlayer and gives rise to re-

sistance states depending on the relative magnetic orientation of the ferromagnetic films. The high value of GMR is reflected in the rapid introduction to the market as read/write heads in hard discs. Enabling even higher densities of  $> 100$  Gbit/inch<sup>2</sup>, the tunnel magnetoresistance effect TMR followed based on ferromagnetic thin films.

Except for hard discs in the beginning of the 21st century the idea evolved to develop an MRAM cell (magnetic random access memory [GP06]) that, contrary to DRAM (dynamic random access memory, extensively used in computers), does not lose its information when switched off. Moreover, it is supposed to feature higher operation speeds. The single memory cell exhibits dimensions down to the nanoscale. This only serves as an example that the proper understanding and control of magnetization in submicron magnets is of uttermost importance for many applications.

However, the characterization of single nanomagnets is not possible with the standard methods such as magneto-optic Kerr effect or SQUID-magnetometry due to the small number magnetic moments. Measurements in arrays with moderate filling factors cannot circumvent this problem because of interfering magnetic dipole interactions.

The domain structure and/or hysteresis behavior of single particles is therefore investigated by new techniques as for example magnetic-force-microscopy (MFM [LCKW01]), Lorentz-microscopy [RPS<sup>+</sup>00], micro-SQUID magnetometry [WHM<sup>+</sup>95] or micro-Hall magnetometry [MJR97].

The first part of this thesis deals with the two noninvasive magnetic sensors for nanomagnets, namely the micro-Hall Magnetometry (MHM) and the technique using micro-SQUIDs. Both offer high resolution while not interfering with the investigated matter as for example the ferromagnetic tip of MFM would.

MHM allows the investigation of the magnetic switching over a wide temperature range. Here the nanomagnet is placed on the middle of a Hall cross fabricated from a semiconductor heterostructure. Applying a current through the structure, the stray field of the nanomagnet gives rise to a Hall voltage which can be seen as a mirror of the magnetization. The resolution limit of this technique due to [GDL<sup>+</sup>97] was found to be a magnetization change in order of  $10^3 \mu_B$ . However, the theoretical resolution limit was

predicted in 2005 to be in the order of only  $1 \mu_B$  [JL05].

The micro-SQUID technique uses the fundamental principle of superconducting rings. Since electrons in superconductors are described by macroscopic wave functions, only multiples of a flux quantum can pass through this ring. Therefore applying an external magnetic field flux which penetrates the ring area leads to an additional ring current to preserve the quantization condition. This current is then a measure of the stray field. The resolution is predicted to enable the detection of a small number of spin-flips [GJFD<sup>+</sup>02]. The only drawback is the need for superconductivity thus restricting the usable temperature range to the critical temperature of the superconductor.

This part of the thesis is structured as follows: At first the basics for the magnetism of microscopic particles will be discussed. Subsequently the theory of MHM is introduced comprising charge transport in two-dimensional electron gases in the presence of external fields. The preparation of the experiment by sputtering a nanomagnet on the Hall cross and the measurements carried out at different temperatures and various sized magnets is the subject of the next chapter. In the end of this block the resolution limit for the sensor obtained is derived.

In the second part of this chapter the basic functionality of micro-SQUID is covered. Then follows an experimental section discussing the process development during this thesis in order to obtain a fully functional micro-SQUID. Subsequently, measurements of such a device in an external field are presented and the resolution limit of the device is determined. Finally, a micro-SQUID with an attached nanomagnet will be the topic of the next section, discussing the magnetization reversal of the nanoparticle. A comparison of the two sensors developed during this thesis will conclude the chapter of micromagnetic sensors.

## 2.1 Micromagnetism

This chapter will give a basic understanding of the physics of the investigated magnetic structures. In the first part a short introduction into ferromagnetism will be given. Then follows a discussion of magnetic domains and the energies involved in the magnetization behavior leading to the characteristic single domain state for very small particles. The next section deals with the calculation of the stray field of a single domain particle in the dipole approximation.

### 2.1.1 Ferromagnetism

Ferromagnetism is the most prominent representative of magnetism which is characterized by the parallel alignment of permanent magnetic moments below a critical temperature - the so called Curie temperature  $T_C$ . The known attraction or repulsion for specific materials has been a miracle to mankind for a long time. It took until the 19th century for scientists to understand the basic characteristics of magnetism based on the idea of elementary magnets [Wil62]. The saturation magnetization could be understood as a state of fully parallel aligned magnets and the inseparability of the north and south poles was obvious. A huge step for the further understanding was given by P. Weiss in the beginning of the 20th century. He managed to describe ferromagnetism with an effective average field created by the elementary magnets and called it "mean field theory" [Wei07]. While the time dependence of the magnetization depending on temperature could be described, the origin of the huge magnetic field needed to align all elementary magnets remained unclear.

Not until quantum mechanics was developed could the source for the molecular field be found. It is the interplay of the Pauli-principle and Coulomb-interaction. Heisenberg finally succeeded in giving a quantitative description of the exchange interaction [Hei28]. The Heisenberg Hamiltonian for spins  $S_{ij}$  located on a lattice with the exchange integral  $J_{ij}$  is:

$$H_{ij} = - \sum_{i=j} J_{ij} \mathbf{S}_i \mathbf{S}_j = -2 \sum_{i>j} J_{ij} \mathbf{S}_i \mathbf{S}_j \quad (2.1)$$

This leads to the following expression for the exchange energy  $E_J$  between the spins  $S_i$  and  $S_j$ :

$$E_{J,ij} = -2J_{ij} \mathbf{S}_i \cdot \mathbf{S}_j = -2J_{ij} S_i S_j \cos(\phi) \quad (2.2)$$

The energy  $E_{J,ij}$  describes a ferromagnetic interaction if the exchange integral  $J_{ij} > 0$ . Then the energy is minimized for all spins being aligned in parallel. Hence one can interpret the magnetic field of the spins  $S_{i \neq j}$  acting on spin  $S_j$  as a mean field which imposes a torque on the corresponding magnetic moment  $\mu_j$ .

Classic ferromagnetic metals as iron, cobalt and nickel belong to the group of the 3d transition metals. Their ferromagnetic behavior relies on the nearly free 3d electrons. The density of states of the 3d bands is very high und the band is not fully occupied. The energy shift between the spin-up and -down 3d-bands leads to a net magnetization because the opposite aligned spins cannot be compensated.

The magnetization  $\mathbf{M}$  is defined as the magnetic moment per volume and has the dimension  $[\frac{A}{m}]$ . Neglecting defects in the material, its absolute amount  $M_S$  is independent of the position on the sample. The saturation magnetization  $M_S$  is specific for each material. Generally the direction of the magnetization depends on time and position.

$$\mathbf{M}(\mathbf{r}, t) = M_S \mathbf{m}(\mathbf{r}, t) \quad (2.3)$$

where  $\mathbf{m}(\mathbf{r}, t)$  is the unity vector. The magnetic polarization  $\mathbf{J}$  (dimension:  $V_S/m^2 = T$ ) is connected to the magnetization by  $\mathbf{J} = \mu_0 \mathbf{M}$  and therefore

$$\mathbf{J} = J_S \mathbf{m}(\mathbf{r}, t) \quad \text{with } J_S = \mu_0 M_S \quad (2.4)$$

where  $\mu_0$  is the permeability of the vacuum and equals  $\mu_0 = 4\pi \cdot 10^{-7} \text{ Vs/Am}$ .

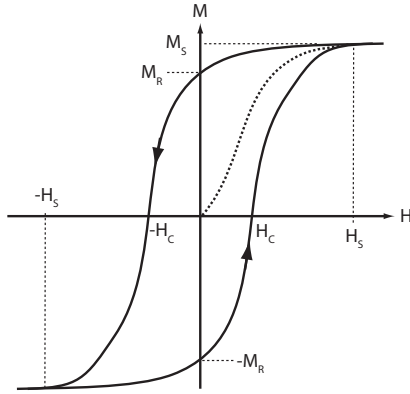


**Fig. 2.1:** Sketch of the magnetization progression of a magnet without history.  $M$  follows first the dashed initial magnetization curve and progresses in a hysteresis loop. The characteristic parameters are shown as well: saturation magnetization  $M_S$ , remanent magnetization  $M_R$ , coercivity  $H_C$ , saturation field  $H_S$ .

The equation

$$\mathbf{B} = \mu_0(\mathbf{H}(\mathbf{r}) + \mathbf{M}(\mathbf{r})) \quad (2.5)$$

expresses that the magnetic flux density  $\mathbf{B}$  consists of the external field  $\mathbf{H}(\mathbf{r})$  and the magnetization  $\mathbf{M}(\mathbf{r})$ . The magnetic flux density has the dimension of  $1 \text{ Vs/m}^2 = 1 \text{ T}$  (Tesla). The external field has the same dimension as the magnetization. In the magnetic community the use of the cgs-unit  $\text{Oe}$  is widely used and can be converted as:  $1 \text{ A/m} = 4\pi/10^3 \text{ Oe} \approx 0.013 \text{ Oe}$ . The conversion of the SI-unit T is much easier:  $1 \text{ T} = 10^4 \text{ Oe}$ . In this work the external magnetic fields will be described in the unit of the magnetic flux density (Tesla).

### 2.1.2 Magnetization and Hysteresis

Fig. 2.1 shows the typical behavior of the magnetization in an external field. It starts from  $M = 0$  and increases slowly. This curve is called the initial magnetization curve. At the magnetic field  $H_S$  the sample reaches the saturation magnetization  $M_S$  where all spins are aligned parallel. The remanent magnetization  $M_R$  is obtained by subsequently lowering the magnetic field back to zero. With further decrease the macroscopic magnetization of 0 is achieved for the coercive field  $-H_C$ . For  $-H_S$  the negative saturation magnetization is obtained. Lowering the field back to zero yields  $-M_R$  and further increase gives  $M = 0$  for  $H_C$ .

Therefore for one specific field two different magnetization states are achievable, depending on the "history" of the material. This progression curve is called *hysteresis* and

forms the basis of magnetic storage devices.

### 2.1.3 Magnetic Energies

Like all entities magnetic systems tend to minimize their energy. The energy itself consists of several contributions. Therefore the stable magnetization configuration is an interplay of all contributions. The systems will stay in the local minimum of the whole energy which mainly consists of the exchange interaction  $E_{ex}$  and the stray field energy  $E_d$  for the magnets investigated in this work.

Even though the Heisenberg interaction is isotropic, most ferromagnets show a preferred orientation of their magnetization. In the case of a zero external field the magnet tends to orient its magnetization to this direction - the so called easy axis. The contributions of Zeeman energy and magnetostriction are negligible for the matter discussed here.

#### 2.1.3.1 Exchange Energy

As mentioned before, the exchange interaction is the mechanism leading to magnetic interactions between the spins and relies on a quantum mechanical description. A quantitative description can be derived by Taylor expansion of the isotropic Heisenberg interaction (2.1) taking only next neighbors into account. The exchange energy can then be rewritten to:

$$E_{ex} = A \int (\nabla \mathbf{m})^2 dV \quad (2.6)$$

The introduced exchange stiffness constant  $A$  depends only on material and temperature and has the following relation with the Curie temperature  $T_C$  and the lattice constant  $a$ :

$$A(T = 0K) = k_B T_C / a \quad (2.7)$$

with the Boltzmann constant  $k_B$ . Even though this model has its limitations due to the assumption of localized spins it can be used in first approximation for the basic understanding of metallic ferromagnets.

### 2.1.3.2 Stray Field Energy

The next energy contribution for a magnetic body is the stray field energy that comes into existence due to the magnetization of the magnetic body. This stray field  $\mathbf{H}_d$  interacts in the same way with the body as an externally applied field. Inside the sample the stray field is opposite to the magnetization and is therefore called the demagnetizing field  $\mathbf{H}_d$ .

According to the potential theory the stray field  $\mathbf{H}_d$  can be derived in terms of a scalar potential  $U_d$  (for a detailed discussion see [Aha00, HS98]):

$$\mathbf{H}_d(\mathbf{r}) = -\nabla U_d(\mathbf{r}) \quad (2.8)$$

The existence of the stray field is connected to a stray field energy which is determined by the integral:

$$E_d = \frac{\mu_0}{2} \int \mathbf{H}_d^2 d^3r = -\frac{\mu_0}{2} \int_{magnet} \mathbf{M} \cdot \mathbf{H}_d dV \quad (2.9)$$

According to equation 2.9 it is obvious that the energy of the stray field is always positive, and vanishes only if there is no stray field at all. This occurs when the magnetic configuration in the sample forms a closed loop.  $\mathbf{M} \cdot \mathbf{H}$  describes the interaction of the field on the magnetization, and the factor 1/2 arises in order not to count interactions twice. The geometry of the sample plays an important role for the magnetic behavior.

Typically, the stray field of samples with any shape are very complicated and cannot be solved analytically. The demagnetizing field, in fact, is only homogeneous inside the whole magnet volume for ellipsoids. However, many bodies can be approximated by ellipsoidal shapes. In this case the demagnetizing field  $\mathbf{H}_d$  can be described by the symmetrical demagnetizing tensor  $\hat{N}_d$  and the magnetization  $\mathbf{M}$  of the ellipsoid:



$$\mathbf{H}_d = -\hat{N}_d \mathbf{M}. \quad (2.10)$$

This equation reflects that the demagnetizing field acts against the magnetization of the magnet, and depends strongly on the geometry of the magnet. With homogeneous  $\mathbf{H}_d$  inside the ellipsoid equation 2.9 can be written as:

$$E_d = \frac{\mu_0}{2} V (\hat{N}_d \cdot \mathbf{M}) \mathbf{M} \quad (2.11)$$

In case of an "egg"-shaped ellipsoid, two axes are equal ( $a = b$ ) and one axis is longer than the other two ( $c > a$ ). This form is named prolate spheroid. Then equation 2.11 can be written as:

$$E_d = \frac{\mu_0}{2} V (N_a - N_c) M^2 \sin^2 \theta \quad (2.12)$$

$$E_d/V = K_s \sin^2 \theta \quad (2.13)$$

with the shape anisotropy constant  $K_s$ , the two demagnetizing factors  $N_a (= N_b)$  and  $N_c$  for the semiminor (a and b) and semimajor axes (c) and the angle  $\theta$  between the magnetization  $\mathbf{M}$  and the semimajor axis c. Considering energy minimization of this term the magnetization will align with the semimajor axis c - the easy axis of this system ( $N_a > N_c$ ). In general, one can draw the conclusion that the shape anisotropy tends to orient the magnetization along the long axis of a body. This is plausible because any other orientation would lead to more magnetic surface charges and therefore to a higher stray field which substantially increases the total energy.

Another interesting shape is the uniformly magnetized, infinite plate. For a magnetization perpendicular to the plane (very unfavorable) the stray field energy equals [HS98]:

$$K_d = \frac{J_S^2}{2\mu_0} \quad (2.14)$$

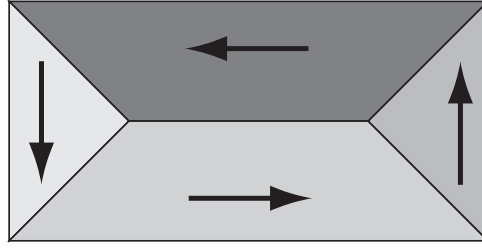


**Fig. 2.2:** Example of a Landau domain structure with the magnetization forming a closed loop.

$K_d$  is a material parameter, and is a measure for the maximum energy density due to stray fields.

It is noteworthy, that shape anisotropy is not an intrinsic property of the magnetic material (as it is the case, e.g., for crystalline anisotropies). Speaking of those, due to the non-crystalline, polymorphic structure of the magnets used in this thesis, there is no anisotropy due to that term and thus will be disregarded.

#### 2.1.4 Domains and Domain Walls

A macroscopic ferromagnet itself typically possesses very little magnetic moment, even though neighboring magnetic moments are pointing in the same direction. Weiss explained this by randomly oriented homogeneous magnetized areas which are called Weiss domains.

The reason is that the stray field energy (2.9) shows a maximum for homogeneously magnetized bodies. Due to minimization of the total energy it is favorable for the sample to build a domain structure.

Landau predicted these domains form in a way to minimize the total magnetic energy of the system, inhibiting stray fields by forming closed loops of the magnetization inside the sample [LL35]. An example for such a structure is depicted in fig 2.2.

The domain structure of a real ferromagnet is more complicated and depends on the balance of the exchange and anisotropy energy terms.

Bloch proposed the term domain wall (DW) for the border between two regions of different magnetization. The orientation in the border does not change abruptly but by a rotation of the magnetization. The energy necessary to nucleate a domain wall is called the domain wall energy  $E_{DW}$ . The domain wall's width is determined by minimization

of exchange and anisotropy energy. The first contribution leads to small rotating angles whereas the latter favors a thin transition area. The DW thickness is therefore an interplay of the total anisotropy constant  $K$  (here the shape anisotropy constant  $K_S$ ) and the exchange stiffness constant  $A$ :

$$\delta_{Bloch} \propto \sqrt{\frac{A}{K}} \quad (2.15)$$

$\delta_{Bloch}$  is the Bloch wall width. In a Bloch wall the magnetization rotates parallel to the domain wall. This wall exists typically in thick magnetic structures. On the contrary, if the thickness of the magnet is in the order of  $\delta_{Bloch}$ , a Néel wall is energetically more favorable. Hence the rotation occurs in the plane of the magnet.

The characteristic length for Néel walls equals:

$$\delta_{Néel} = \sqrt{\frac{A}{K_d}} \quad (2.16)$$

with  $K_d$  from (2.14). In macroscopic samples, the long-range dipole-interaction wins over the short range exchange-interaction. In small samples, on the contrary, the energy contribution of the domain walls  $E_{DW}$  overcomes the stray field energy up to the point when a single domain configuration is the energetic lowest state. The critical length scale for this phenomenon has been found to be in the order of  $10 \delta_{Néel}$  [Sch91, HK02]. When introducing the material parameters for permalloy (Py, see C.1)  $\delta_{Néel}$  equals  $5.7 \text{ nm}$  and thus a nearly uniform magnetization is achieved for a cube with edges in the order of  $50 \text{ nm}$ . When the length scale  $\delta_{Bloch}$  is surpassed, multi-domain configurations come into existence. In the intermediate regime, the magnetization configuration flows continuously (e.g. vortex states [Rah05]). In thin ferromagnetic Py-films in the order of  $50 \text{ nm}$  and below, the magnetization lies inside the plane of the ferromagnet and the typical domain walls are of the Néel-type. The single domain state occurs here as well when the domain wall energies exceed the stray field energy.

### 2.1.5 Domains in an External Field

While applying an external field to a magnet, the domain configuration is altered compared to the remanent state. The domain walls with parallel orientation to the external field grow while antiparallel ones shrink. This happens first reversibly, and later irreversibly (when the slope becomes steep in the hysteresis curve 2.1). With continuous increase of the external field the last remaining domains are forced into a parallel orientation. One can say a single domain state comes into existence for the saturation magnetization. This explains the flat slope in the end of the hysteresis because the high stray field energy must be overcome.

In principle, the energy for the movement of domain walls in an ideal ferromagnet is minuscule. However, this is not true for real ferromagnets. Here, domain walls get pinned at defects, constrictions and other errors in the structure. Therefore an external field is needed for depinning domain walls which is an abrupt process (Barkhausen jumps).

Another situation occurs for single domain particles. Here, in the remanent state, the magnetization lies in the direction of the easy axis of the particle and equals the saturation magnetization. In the case of uniaxial easy axis the magnetization therefore has exactly two antiparallel states for its orientation. The Stoner-Wohlfarth-model [SW48] describes the movement of the magnetization in an external field. It predicts a coherent rotation of all magnetic moments in an external field that is not parallel to the magnetization and an abrupt switching to the symmetric state. For a parallel configuration the hysteresis loop of the single-domain particle becomes rectangular with two states.

The coercive field of these single-domain particles depends strongly on the geometry. In the case of a rectangular bar (slab), the magnetization reversal can be seen as the nucleation of a domain wall which afterwards penetrates the whole magnet. The nucleation energy is given by eq (2.9) but cannot be calculated analytically. Brown [Bro64] performed numerical calculations and was able to obtain upper and lower bounds for the dependence of the nucleation field on the geometry of an infinite rectangular bar. The nucleation field is given by equation (2.17)

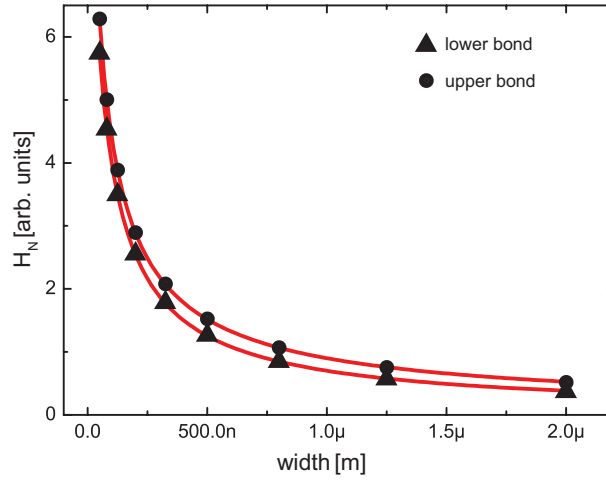


**Fig. 2.3:** Upper (square) and lower (triangle) bonds for the expected progression of the coercive field due to [Bro64]; The depicted fits serve for comparison with the experiment.

$$-H_n M_S = g + \rho M_S^2 \quad (2.17)$$

where  $g$  is an anisotropy constant and  $\rho$  is a numerical factor. The calculations yield values for the upper and lower bonds of  $\rho$  which depends on the thickness and width of the slab. Therefore the progression of the nucleation field (coercive field) can be derived and is shown in fig. 2.3 in arbitrary units.

The fits confirm a hyperbolic-like increase of the nucleation field for decreasing widths. A similar  $1/w$  dependence can be derived with the Stoner-Wohlfarth-model for an infinite cigar-shaped ferromagnet [Hoc03].

### 2.1.6 Stray Field of a Rectangular Bar

This section deals with the investigation of the stray field of magnetic particles. Its two dimensional progression as well as the strength of the z-component will be discussed. The latter component is the field measured by planar sensors. That is because these are insensitive to the magnetic field components parallel to the plane. The model for ferromagnetic stripes is based on the dipole model. The geometry used assumes parallel alignment of the magnetization to the plane of the magnetic field sensor. Furthermore,

a single domain particle behavior is implied (due to strong shape anisotropy) with full magnetization switching of the whole ferromagnet. That means domain structures inside the material are absent.

### 2.1.6.1 Dipole Model

In this section the external magnetic field produced by a ferromagnet will be calculated. One of Maxwell's equations in absence of any currents equals:

$$\nabla \times \mathbf{H} = 0 \quad (2.18)$$

One way to suffice this equation is to introduce a vector potential  $\mathbf{A}$  as  $\mathbf{B} = \nabla \times \mathbf{A}$ . However, the magnetostatics investigated in this thesis are better described by a scalar potential  $U$  which also is a solution to (2.18) and is given by:

$$\mathbf{H} = -\nabla U \quad (2.19)$$

In analogy to electric dipoles, the potential  $U$  for a magnetic dipole is as follows:

$$U(\mathbf{r}) = \frac{\mathbf{m}}{4\pi} \nabla_{r'} \frac{1}{|\mathbf{r} - \mathbf{r}'|} \quad (2.20)$$

$$U(\mathbf{r}) = \frac{\mathbf{m}}{4\pi} \frac{(x\hat{x} + y\hat{y} + z\hat{z})}{[(x - x')^2 + (y - y')^2 + (z - z')^2]^{3/2}} \quad (2.21)$$

where  $\mathbf{m}$  is the magnetic dipole moment of the system and  $\mu_0$  is the vacuum permeability.

The geometry used for the following calculations is adjusted to allow for calculations of the stray field of ferromagnetic rods and is depicted in fig. 2.4. It is assumed that the ferromagnetic rod exhibits the saturation magnetization under absence of domain walls. The magnetostatic potential can then be calculated by integrating over all infinitesimal small magnetic moments  $d\mathbf{m}$  in the volume of the ferromagnet. The magnetic moments are all aligned in the x-direction, so  $d\mathbf{m} = dm\hat{x}$ . A similar approach has been used before to calculate the magnetic stray field of ferromagnetic thin film in [SAT<sup>+</sup>97].

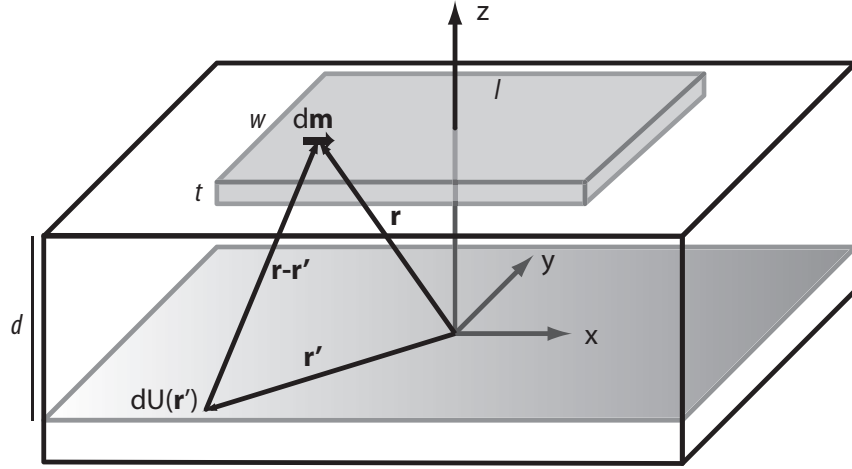


**Fig. 2.4:** Description of the geometry used for the calculation of the stray field of the magnetic nanoparticle. The plane consists of numerous infinitesimal magnetic dipole moments located at  $(x, y, z)$ .

The infinitesimal potential  $dU$  at the position  $(x', y', z')$  created by  $d\mathbf{m}$  at  $(x, y, z)$  can be written as:

$$dU(\mathbf{x}', \mathbf{y}', \mathbf{z}') = \frac{\mu_0}{4\pi} \frac{dm(x - x')}{[(x - x')^2 + (y - y')^2 + (z - z')^2]^{3/2}} \quad (2.22)$$

The following integration leads to:

$$U(x', y', z') = \int_{-w/2}^{w/2} \int_{-l/2}^{l/2} \int_d^{d+t} \frac{\mu_0}{4\pi} \frac{dm(x - x')}{[(x - x')^2 + (y - y')^2 + (z - z')^2]^{3/2}} dx dy dz \quad (2.23)$$

Here  $w$  and  $l$  are the corresponding width and length of the ferromagnetic rod and  $t$  is its thickness. The zero of the  $z$  axis lies within the sensor area and consequently the distance to the sensor is  $d$  and the integration boundaries for the  $z$ -value range from  $d$  to  $d+t$ .

For applications in planar sensors, one is interested in the component of the magnetic field flux perpendicular to the surface of the sensor. With the definition given in (2.19) the  $z$ -component of the magnetic field flux  $B$  at the position  $(x', y', z')$  is:

$$B_z = -\frac{\partial U}{\partial z'} = -\frac{\partial}{\partial z'} \int_V dU dV \quad (2.24)$$

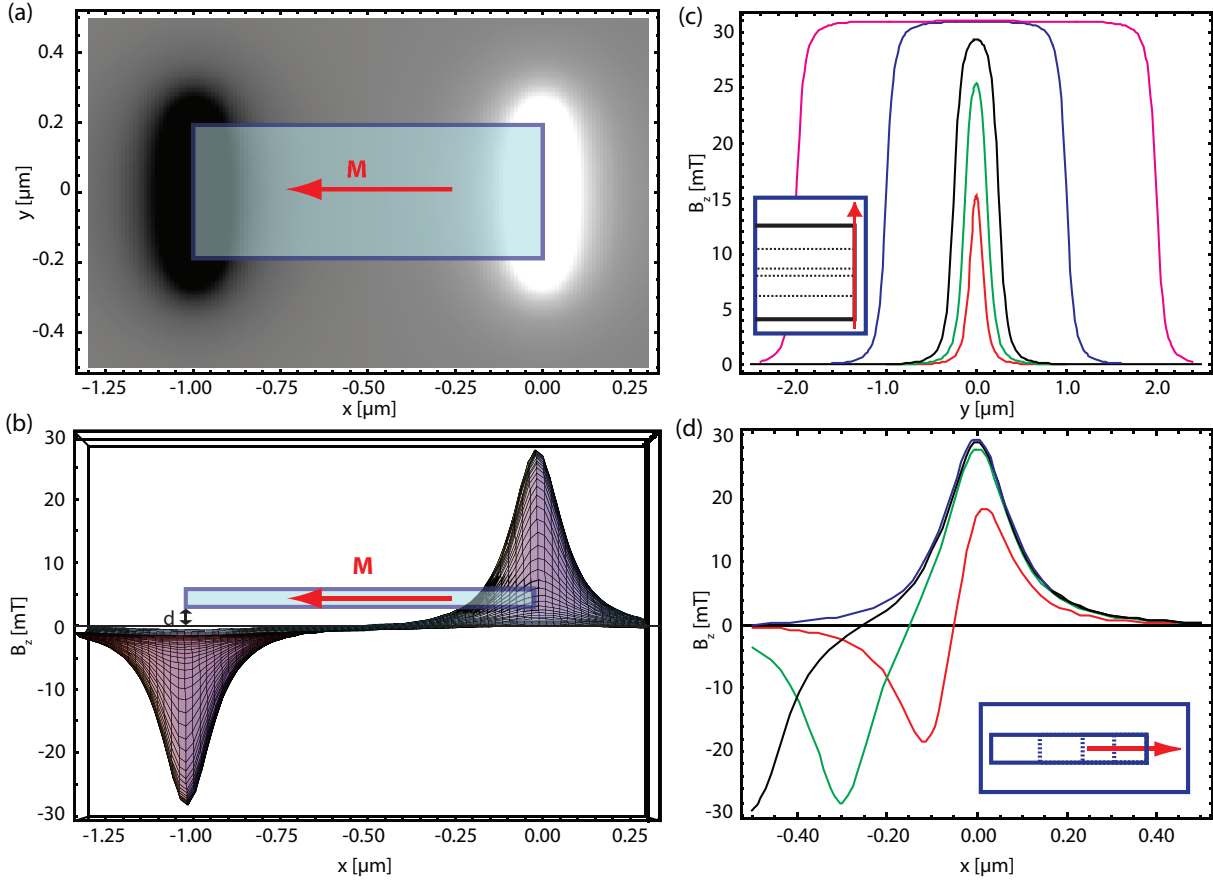


**Fig. 2.5:** Calculations of the  $B_z$ -component in a plane  $80\text{ nm}$  below a single-domain permalloy rod with a thickness  $t$  of  $20\text{ nm}$ . (a) maps the stray field of a  $400\text{ nm}$  wide and  $1\text{ }\mu\text{m}$  long rod in the  $x$ - and  $y$ -direction; gray scale coding for  $B_z$ ; (b) 3D side view of (a) showing the different signs of  $B_z$  and visualizing the depth below the ferromagnet where  $B_z$  is calculated. (c) cut at the rod's edge in  $y$ -direction for variation of the rod's width showing stable saturation  $> 1\text{ }\mu\text{m}$  of about  $30\text{ mT}$  (length as in (a)); (d) cut in the middle of the stripe in  $x$ -direction with a saturation for lengths  $> 300\text{ nm}$  (width as in (a)).

The solution of this equation is lengthy and has been obtained using Mathematica<sup>TM</sup>. In the following section the strength of the stray field of a ferromagnetic rod has been calculated in order to understand the consequences for building planar magnetic sensors.

### 2.1.6.2 Estimation of the Stray Field

The model drawn in the previous section will now be used to calculate the  $z$ -component of the stray field strength of a ferromagnetic rod at the surface of a planar sensor. It lies in distance  $d$  below the ferromagnet. In fig. 2.5 the stray field of a  $20\text{ nm}$  thick permalloy



nanorod is depicted. For fig. 2.5a and b the width and length of the wire are  $400\text{ nm}$  and  $1\ \mu\text{m}$ , respectively. The depth of the sensor is assumed to be  $80\text{ nm}$  - well in accordance with sensors introduced later. The studied nanorod is sketched as a blue rectangle to give an idea of its dimensions. The magnetization is homogeneous and parallel to the minus x-direction. The gray scale coding in fig 2.5a shows the magnetic field flux  $B_z$  of the stray field and the two ellipsoidal shapes reflect a strong localization under the edge of the wire.

Remarkably, the maximum of the magnetic field reaches about  $30\text{ mT}$  in this configuration (see fig. 2.5b), a value commonly measurable in the case of a homogeneous magnetic field. The depth of the sensor plane is sketched in fig. 2.5b in a way that the blue rectangle floats above the zero value of  $B_z$ , using the x-axis scale to visualize the depth  $d$ . As expected, the stray field is point-symmetrical to the middle of the magnet. That means the magnetic field on one edge is the inverse of the one at the other end. The influence of the width and length of the magnet on the stray field is calculated in the other two subfigures. In fig. 2.5c the length is kept constant at  $1\ \mu\text{m}$  and the calculations are performed for widths of  $100, 300, 500\text{ nm}$ ,  $1$  and  $2\ \mu\text{m}$  (red, green, black, blue and magenta).  $B_{z,max}$  increases for widths up to  $500\text{ nm}$  and reaches a saturation for  $w > 1\ \mu\text{m}$ . This is reasonable since the dipole density is kept constant. In fig. 2.5d simulations for the x-axis progression are performed with a constant width of  $400\text{ nm}$  and lengths of  $100, 300, 500$  and  $1000\text{ nm}$  (red, green, black and blue). A noteworthy fact is that  $B_{z,max}$  is constant for a length of  $200\text{ nm}$  already. So, keeping the cross-section  $w \cdot t$  constant, the length of the rod does not alter the signal for  $l > 200\text{ nm}$ .

When looking at the  $100\text{ nm}$  long wire one instantly understands the important role the active section of the magnetic sensor plays for nanomagnets. These sensors usually give a signal somewhat proportional to the average magnetic flux in their active area  $A_S$  which describes the sensitive part of the sensor:

$$\text{signal} \propto \langle B_z \rangle = \frac{1}{A_S} \int_{A_S} B_z(x, y) dx dy \quad (2.25)$$

The average magnetic field  $\langle B_z \rangle$  of the magnet from 2.5a equals  $9.1\text{ mT}$  ( $2.8\text{ mT}$ ) for a quadratic sensor with edge length of  $0.5 \cdot 0.5\ \mu\text{m}^2$  ( $1.0 \cdot 1.0\ \mu\text{m}^2$ ). Therefore two conclusions

can be drawn: the average field strength is significantly lower than the maximum strength of  $30 \text{ mT}$  from fig. 2.5c, and depends on the sensor area. Thus the latter must be adjusted to the presumed extension of the localized field in order to resolve magnetization changes of small nanoparticles.

### 2.1.7 Stray Field of a Particle

Because the rectangular bar does not give an intuitive idea of the sensitivity in the sense of magnetic moment resolution, the stray field of a single domain magnetic spheroid will be discussed here. The particle has a radius  $R$ , a magnetic moment  $m$  and is situated at a distance  $d$  above the center of the sensor area. The particles' magnetization is assumed to point perpendicular to the sensor plane.

The magnetic field distribution  $B_z(x, y)$  of such a particle centered above the sensor can be calculated analytically (see for example [Mih06]):

$$B_z(x, y) = \frac{\mu_0 m}{4\pi} \frac{2z^2 - x^2 - y^2}{(x^2 + y^2 + z^2)^{5/2}} \quad (2.26)$$

where  $z = R + d$  is the distance from the center of the particle to the sensor. For the average field it follows with equation 2.25:

$$\langle B_z \rangle = \frac{\mu_0 m}{4\pi w^2} \int_{-\frac{w}{2}}^{\frac{w}{2}} \int_{-\frac{w}{2}}^{\frac{w}{2}} \frac{2z^2 - x^2 - y^2}{(x^2 + y^2 + z^2)^{5/2}} \quad (2.27)$$

$$= \frac{4\mu_0 m}{\pi} \frac{\sqrt{\frac{w^2}{2} + z^2}}{w^4 + 6w^2 + z^2 + 8z^4} \quad (2.28)$$

This result allows for the derivation of magnetic moment resolution of magnetic sensors. This is a better figure of merit for determining strongly localized magnetic fields than the magnetic field sensitivity because it takes the advantage of small sensor areas for high flux sensitivity into account.

This chapter has given a brief overview of general ferromagnetism and insights to the world of micromagnetism. The next chapters deal with the micromagnetic sensors

fabricated during this thesis. They will be explained theoretically and corresponding measurements will be shown, starting with micro-Hall magnetometry.

## 2.2 Micro-Hall Magnetometry

This section deals with the micro-Hall magnetometry (MHM). Due to its sensitivity MHM is a very powerful technique to investigate the magnetization behavior of nanoparticles [MJR97, GDL<sup>+</sup>97].

Hall sensors consist of a conductive layer in the x-y-plane which is structured in a cross-like shape. In order to achieve high magnetic field sensitivities the conductive layer is a two-dimensional-electron gas (2DEG) with high mobility electrons which are confined in the z-direction.

In general, electric transport in 2DEGs can be described using the Drude model. This is because these systems with their parabolic energy dispersion resemble the nearly free electron gas. The model is sufficient to describe the general properties of the following Hall sensors. However, the limits of the Drude model are reached when high magnetic fields are applied and the density of states forms Landau levels. The same is true when the sample dimensions are in the order of the mean free path of the electrons. In that case they mainly scatter at the boundaries of the sample and behave ballistically. Here, the Hall voltage depends strongly on the shape of the cross.

The purpose of this chapter is to give an overview of the possibilities and limits of micro-Hall magnetometry by describing the key properties of the sensor. Subsequently, the fabrication on the two different 2DEGs of InAs and HgTe will be explained. Their high-field properties are used for characterization. Hysteresis curves of deployed CoFe, CoFeB and NiFe magnets at 4.2 K up to room temperature will be presented. Furthermore the change in coercivity for magnets with different aspect ratios (shape anisotropies) is shown. The resolution limit in terms of field flux and magnetic moment is determined in the end of this section.

### 2.2.1 2D Electron Gas

The highest sensitivity for MHM sensors can be achieved using high mobility and reasonable low carrier-concentration materials. Metal films offer too high densities and the mobility in standard doped semiconductors is too low. However, the two-dimensional

electron gas - a semiconductor heterostructure - offers both high mobility and low carrier density. Thus 2DEGs are the material of choice for high sensitive MHM sensors.

### 2.2.1.1 InAs and HgTe Heterostructures

2DEGs come into existence when the movement of electrons is constricted in one dimension, leaving the remaining two dimensions for transport. This can be achieved in the form of triangular potential that e.g. develops due to band bending at the interface of the (Al,Ga)As/GaAs heterostructure. The 2DEGs used in this work, however, are created by the quantum well (QW) heterostructures. There are three different kinds of quantum wells which are classified due to their valence band offset and energy gaps. The type-I quantum well is typical for an (Al,Ga)Ga/GaAs/(Al,Ga)As heterostructure. The energy gap of (Al,Ga)As is much higher than the one of GaAs and the valence band offset (VBO) is positive. Therefore electrons and holes are trapped in the same layer - the quantum well structure. In a type-II QW the energy gap of the barrier and QW material are of similar order and the VBO between the chosen materials determines whether electrons or holes are located in the quantum well, while the other charge carrier type can move free in the "barrier" material. The QW of type-III comes into existence when a semimetal is combined with a semiconductor. Here the bands between the barrier and QW cross because the QW material exhibits a negative band gap.

In this thesis two types of quantum wells have been used, namely InAs and HgTe 2DEGs. InAs belongs to the type-II QWs where electrons are trapped in the well. The samples were grown by molecular beam epitaxy (MBE) in the MBE cluster owned by the chair Experimentelle Physik III of the University of Würzburg. The MBE cluster offers ultra-high-vacuum (UHV) at a base pressure in the order of  $10^{-10}$  mbar and transport between different MBE chambers without breaking the vacuum. This enables the deposition of many different materials at high crystalline quality. The grown stack with a sketch of the band structure is depicted in fig. 2.6.

The complex heterostructure stack below the actual QW on the right side of fig. 2.6 was introduced in order to minimize dislocations and prevent parallel conductivity via the

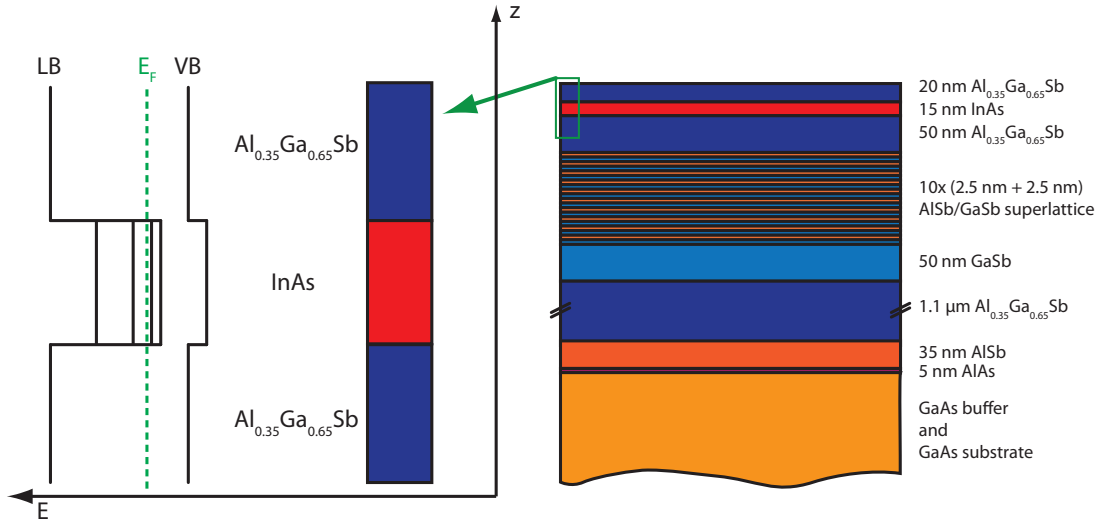


**Fig. 2.6:** The InAs 2DEG structure - on the left the schematic band structure (without taking band bending into account), on the right the grown stack of semiconductor materials in order to achieve high electron mobilities with few dislocations.

substrate. For particulars on the growth, see [Gra05] where the process is explained in detail. There is no doping layer present so the electrons of the InAs 2DEG originate from surface states of the cap layer and deep donors from the interfaces. A very important property of InAs is that the Fermi level of the InAs surface is pinned by about 130 meV above the minimum of the conduction band [BBNK97]. This situation has two important influences on the fabrication process:

First, ohmic contacts can be achieved without alloying but rather depositing the contact metal directly on top of the InAs layer - in absence of a Schottky barrier. Secondly, the confining potentials at the edge of the 2DEG is abrupt for electrons (in other words: of rectangular shape). Thus the geometrical width of the processed devices is the same as the one which is experienced by the wave function of the electrons [CYY00]. This enables the possibility to fabricate sub- $\mu\text{m}$  sensors.

The HgTe 2DEG on the other hand belongs to the type-III quantum wells. The particulars of its band structure will be explained in section 3.1. Here we are only interested in the conduction band that is depicted in fig. 2.7. An exemplary stack is also drawn, where the buffer is visible as well as the two iodine modulation doped layers. These are separated by two spacers from the quantum well in order to achieve high

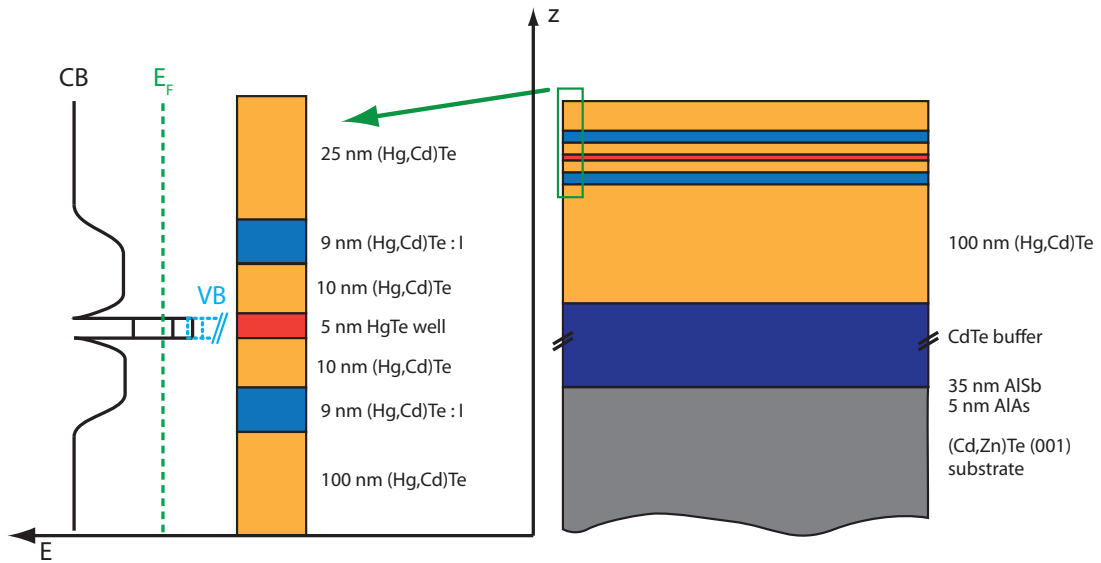


**Fig. 2.7:** An exemplary stack for the grown HgTe heterostructure with a quantum well width of 5 nm. The energy dispersion for the conduction band is depicted on the left. The crossing of the valence band is sketched as well. Here the quantized conduction band states are above the valence band states due to quantum confinement. The Fermi energy is adjusted by the doping layers to lay above the first subband.

mobilities. The growth of the mercury based heterostructure is not straightforward compared to other heterostructures. For the peculiarities on the growth of this 2DEG, refer to [GGPJ+98, ZPJO+01, Brü07].

In both types, potential constrictions cause a quantization of energy in z-direction, while energies in the x-y plane are continuous. The Fermi energy is either natural or adjusted by external doping in such a way that only one subband is populated. This is the favorable case since there is no ambiguity in the energy dispersion and measurements do not bear a superposition of energy bands.

### 2.2.1.2 Properties of the 2DEG

The energy dispersion of the  $n$ th-quantized level of the 2DEG in the periodic potential of the crystal can be approximated by a parabolic dispersion (see [BvH91, Dat95] for a detailed discussion):

$$E_F - E_n = \frac{\hbar^2 k_F^2}{2m_{\text{eff}}} \quad (2.29)$$

with the effective mass  $m_{\text{eff}}$  which will be described in (2.34). Using the two dimensional density of states  $\frac{m_{\text{eff}}}{\pi\hbar^2}$  the carrier concentration is then given by

$$n_e = \frac{m_{\text{eff}}}{\pi\hbar^2}(E_F - E_0) \quad (2.30)$$

The periodic potential of the crystal leads to the substitution of the electron mass by the effective mass while the density of states in 2D is constant.  $E_F$  is the Fermi energy and  $E_0$  is the energy of the lowest subband for  $k=0$ . Typical values for both 2DEGs are in the order of about  $1 \cdot 10^{12} \text{cm}^{-2}$ . By knowing just the carrier concentration the characteristic wavevector  $k_F$ , the Fermi wavelength  $\lambda_F$  and the Fermi velocity  $v_F$  of the electrons can be derived:

$$k_F = \sqrt{2\pi n_e} \quad (2.31)$$

$$\lambda_F = \frac{2\pi}{k_F} = \sqrt{2\pi/n_e} \quad (2.32)$$

$$v_F = \hbar \frac{\partial E}{\partial k} = \frac{\hbar}{m_{\text{eff}}} \quad (2.33)$$

A good approximation for the transport in 2DEGs is the Drude model which will be discussed in the next section. Furthermore the experimental methods to determine the carrier concentration as well as the mobility will be discussed.

### 2.2.2 Electronic Transport

The very first and simultaneously very successful model of electronic transport was developed by Drude in 1900 [Dru00]. He treated the carriers as a free electron gas consisting of hard spheres with electronic charge  $e$  and mass  $m_e$  which obey Newton's laws. Furthermore, he assumed they travel in a direct line, before experiencing a scattering event at an



average time  $\tau$ , when the velocity is abruptly changed. This time is called the relaxation time.

The electrons do not move in vacuum but in a periodic potential of the crystal. This circumstance is incorporated into the theory by introducing the effective mass  $m_{\text{eff}}$  into the Drude theory. The effective mass reflects the band structure and is given by

$$m_{\text{eff}}(k) = \hbar^2 \left( \frac{\partial^2 E}{\partial k^2} \right)^{-1} \quad (2.34)$$

This is the bending of the energy band, and will be approximated here as a scalar factor, independent of  $k$ . This is because the energy dispersion in most 2DEGs is parabolic and symmetric in  $k$ -space. Thus  $m_{\text{eff}}$  carries all the information about the band structure. The values for  $m_{\text{eff}}$  in the used materials are:  $m_{\text{eff,InAs}} = 0.023 m_e$  [Kit05] and  $m_{\text{eff,HgTe}} = 0.030 m_e$  [PSH<sup>+</sup>87].

Based on the observation that applying a force (e.g. an electric field) the current does not increase to infinity but moreover reaches a state of equilibrium, we can assume a compensation of the external force by collisions within the relaxation time  $\tau$ :

$$\left( \frac{d\mathbf{p}}{dt} \right)_{\text{force}} = \left( \frac{d\mathbf{p}}{dt} \right)_{\text{scatter}} = \frac{\mathbf{p}}{\tau} \quad (2.35)$$

The force acting on charge carriers by external fields is given by the Lorentz force:

$$\mathbf{F}_L = q(\mathbf{E} + \mathbf{v} \times \mathbf{B}) \quad (2.36)$$

Given that only an electric field exists we obtain:

$$q\mathbf{E} = \frac{m_{\text{eff}}\mathbf{v}_D}{\tau} \quad (2.37)$$

where  $q$  is the charge of the particle and  $\mathbf{v}_D$  is the drift velocity which can be interpreted as the average velocity of the ensemble. The average distance between two scattering processes then equals the mean free path  $l_e$ :

$$l_e = v_D \tau \sqrt{2\pi n_e} \quad (2.38)$$

Dividing the modulus of the drift velocity by the modulus of the electric field the effect of the electric field on the velocity is quantified.

$$\mu = \frac{v_D}{E} \quad (2.39)$$

This ratio is the mobility and plays an important role for the electronic transport. For electrons with charge  $q = -e$ , using the definition of the current density:  $\mathbf{j} = -ne\mathbf{v}_D$  and drift velocity from (2.37) leads to

$$\mathbf{j} = \left( \frac{ne^2\tau}{m_{\text{eff}}} \right) \mathbf{E} = \sigma \mathbf{E} \quad (2.40)$$

This relation exhibits a linear dependence of  $\mathbf{j}$  on  $\mathbf{E}$  with conductivity  $\sigma_0$ , the Drude conductivity. Despite the simplicity of this model, it is quite intuitive and serves as a valuable start for estimations of basic transport properties.

In case a homogeneous magnetic field  $\mathbf{B}$  is applied, the electron's path deviates from the direction of the electric field due to the Lorentz force. This effect is the well-known classical Hall effect discovered by Edwin Hall in 1879 [Hal79]. Given an applied electric field  $\mathbf{E} = E_x(1, 0, 0)$  and a magnetic field  $\mathbf{B} = B_z(0, 0, 1)$  the equation of motion equals:

$$m_{\text{eff}} \left( \frac{d}{dt} + \frac{1}{\tau} \right) \mathbf{v} = q (\mathbf{E} + \mathbf{v} \times \mathbf{B}) \quad (2.41)$$

For the equilibrium state ( $\frac{d\mathbf{v}}{dt} = 0$ ), we can rearrange (2.41) to the form:

$$\begin{bmatrix} m_{\text{eff}}/e\tau & -B_z \\ +B_z & m_{\text{eff}}/e\tau \end{bmatrix} \begin{pmatrix} v_x \\ v_y \end{pmatrix} = \begin{pmatrix} E_x \\ E_y \end{pmatrix} \quad (2.42)$$

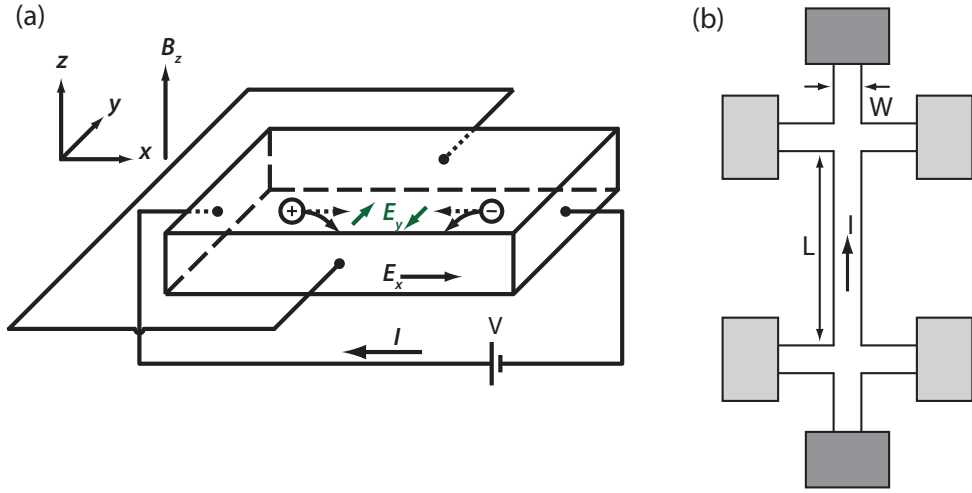


**Fig. 2.8:** Sketch of the Hall effect (a) applied voltage  $V$  causes current in  $+x$  direction; electrons travel left to right (holes vice versa). Lorentz force bends initial path, deflects both carrier types to  $-y$  direction, giving rise to positive (negative) Hall voltage for holes (electrons) (b) typical Hall bar geometry (channel width  $W$ , length  $L$ ) with 2 current contacts (dark gray) and 4 voltage contacts (light gray). Enables measurement of longitudinal  $V_x$  and transversal  $V_H$ .

Here only two dimensions are considered due to confinement in the  $z$ -direction.  $\mathbf{v}_{x,y}$  is the drift velocity of the electrons in the  $x, y$  plane and  $\mathbf{E}_{x,y}$  are the components of the electric field in the  $x$ - and  $y$ - direction. Introducing the current density  $\mathbf{j}$ :

$$\begin{pmatrix} E_x \\ E_y \end{pmatrix} = \sigma_0^{-1} \begin{bmatrix} 1 & -\mu B \\ \mu B & 1 \end{bmatrix} \begin{pmatrix} j_x \\ j_y \end{pmatrix} = \begin{bmatrix} \rho_{xx} & \rho_{xy} \\ \rho_{yx} & \rho_{yy} \end{bmatrix} \begin{pmatrix} j_x \\ j_y \end{pmatrix} \quad (2.43)$$

with its definition 2.39 the mobility  $\mu = |q|\tau/m_{\text{eff}}$ .  $\hat{\rho}$  is the resistivity tensor from Ohm's law  $\mathbf{E} = \hat{\rho}\mathbf{j}$  and  $\sigma_0 = n|q|\mu$  is the Drude conductivity from (2.40). We now deduct for low magnetic fields  $B\tau \ll 1$  from (2.43):

$$\rho_{xx} = \rho_{yy} = \sigma^{-1} = \frac{m_{\text{eff}}}{ne^2\tau} \quad (2.44)$$

$$\rho_{xy} = -\rho_{yx} = \frac{\mu B}{\sigma_0} = \frac{1}{nq}B \quad (2.45)$$

Thus the Drude model gives two results for the transport in a perpendicular magnetic field: the longitudinal resistivity is constant and the Hall resistivity shows a linear dependence in a magnetic field.

The carrier concentration and the mobility of the 2DEG can be determined with these results. With the chosen sample geometry (as in fig. 2.8b) the current can only flow along the x- and not in the y-direction. With  $j_x = I/W$  and  $j_y = 0$  it follows that:

$$E_y/W = V_H = \frac{IB}{qn} = R_H IB \quad (2.46)$$

$$E_x/L = V_x = \frac{I}{\mu n |q|} \frac{L}{W} \quad (2.47)$$

with the Hall constant  $R_H$  and therefore:

$$n = \frac{I/|q|}{dV_H/dB} \quad (2.48)$$

$$\mu = \frac{I/|q|}{nV_x} \frac{L}{W} \quad (2.49)$$

The MBE-grown 2DEGs in this work were characterized by Hall bar samples fabricated by standard photolithography and etching. With equations 2.48 and 2.49 it is straightforward to obtain the characteristic quantities  $n$  and  $\mu$  of the 2DEG by measuring  $V_H$  and  $V_x$  simultaneously in a swept magnetic field.

It must be stated that the Drude approximation in 2DEGs only holds true if the dispersion remains parabolic and low electric and magnetic fields are applied. In the case of high magnetic fields the transverse and longitudinal resistances show a very peculiar behavior that is not covered in the Drude model. This is due to the formation of Landau levels which lead to the quantum Hall effect.

### 2.2.3 Quantum Hall Effect

The quantum Hall effect (QHE) appears in systems where electrons are described by a 2DEG. The characteristic QHE curve for InAs 2DEGs is depicted in fig. 2.9. The Hall resistance  $R_{xy} = V_H/I$  increases linearly for low magnetic fields as expected from the Drude theory. At about 2 T, forming of plateaux with constant resistances takes place. The longitudinal resistance  $R_{xx} = V_x/I$  is starting at 0 T more or less constant as

expected by the Drude model (the increase for  $B = 0$  T is due to quantum interference effects and shall be discussed later). At a magnetic field of about 1 T, the resistance starts to oscillate with growing amplitude. Comparing with the Hall resistance, the peaks occur between the plateaux. The observation of plateaux in  $R_{xy}$  has been discovered by Klaus von Klitzing in 1980 [KDP80] and is called the quantum Hall effect. Not much later, in 1985, he was awarded the Nobel Prize for this discovery. The second observation is Shubnikov-de Haas oscillations. These and the quantum Hall effect can be described by the edge channel model [Dat95, BvH91], which will be briefly discussed below.

For sufficient low temperature and high mobility electrons the plateaux in the Hall resistance occur exactly at values of

$$R_{xy} = \frac{V_H}{I} = \frac{1}{\nu} \frac{h}{e^2} = \frac{1}{\nu} R_K \quad (2.50)$$

$$R_K = 25812,8074434 \Omega$$

with the number of occupied Landau levels (LL)  $\nu$  ( $\nu = 1, 2, 3, \dots$ , see below). The Klitzing constant  $R_K$  is extremely precise and thus now used as the standard for resistance measurements. In order to understand the quantization in magnetic fields one first needs the time-independent Schrödinger equation for a two-dimensional electron system:

$$\hat{H}\Psi = \left[ -\frac{\hbar^2}{2m} \left( \nabla - \frac{e\mathbf{A}}{i\hbar} \right)^2 \right] \Psi = E\Psi \quad (2.51)$$

with the vector potential  $\mathbf{A}$  which must fulfill the requirement  $\mathbf{B} = \text{rot}\mathbf{A}$ . Solving this eigenvalue problem for two dimensional systems leads to the problem of a harmonic oscillator and the Hermite polynomials as solution. The energy eigenvalues are given by:

$$\epsilon_n = \hbar \frac{eB}{m} \left( n + \frac{1}{2} \right) = \hbar\omega_c \left( n + \frac{1}{2} \right) \quad (2.52)$$

with ( $n = 0, 1, 2, 3 \dots$ ) and thus the zero-point energy  $\frac{1}{2}\hbar\omega_c$  for  $n = 0$  where  $\omega_c = \frac{eB}{m}$  is the cyclotron frequency. Taking the spin into account the eigenvalues equal [BvH91]:

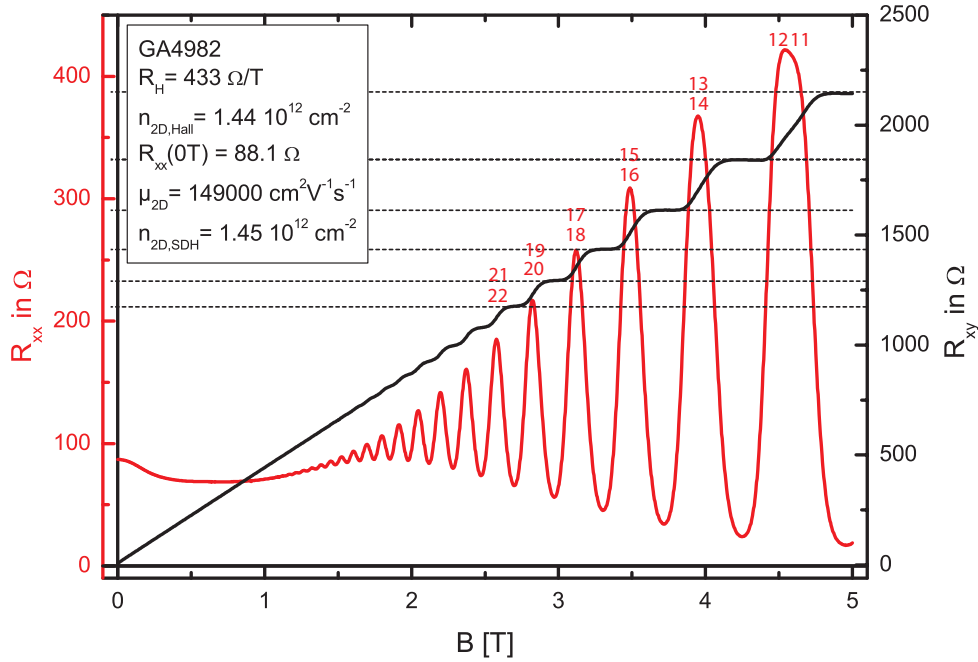


**Fig. 2.9:** Characterization measurement on standard Hallbar with  $W=200 \mu\text{m}$  and  $L=600 \mu\text{m}$ ; carrier concentration has been determined by the slope of  $R_{xy}$  as well as the periodicity of the Shubnikov-de Haas oscillations with conformal results. Red numbers represent filling factors  $\nu$  derived from  $R_{xy}$ .

$$\epsilon_n = \hbar\omega_c \left( n + \frac{1}{2} \right) \pm \frac{1}{2}g\mu_B B \quad (2.53)$$

where  $\frac{1}{2}g\mu_B B$  is due to the Zeeman spin splitting which increases linearly with the magnetic field.  $\nu = 2(n + 1)$  is the number of the spin-degenerated Landau level. With quantization in a magnetic field, the density of states changes from the constant value without a magnetic field into a sequence of  $\delta$ -functions at the eigenenergies (see fig 2.10a). These  $\delta$ -peaks widen due to nonzero temperature and imperfections. In case of giant Zeeman splitting or very high fields, the Landau level  $n$  splits into two separate levels with filling factors  $\nu = 2n + 1$  and  $2n + 2$ . Compare in fig. 2.9 the broadening of the last peak which is a sign of beginning spin splitting.

The quantization can be understood as if the electrons are moving on cyclotron paths which are only stable if the circumference is a multiple of the Fermi wavelength. This picture also gives an idea of the length scale when Shubnikov-de Haas oscillations occur. Here the scattering length must be long enough that the electron can propagate some

cyclotron paths before scattering occurs. That means that the time for one cyclotron propagation must be smaller than the relaxation time, which leads to the simple equation:

$$\frac{2\pi}{\omega_c} < \tau \rightarrow \frac{2\pi m_{\text{eff}}}{eB} < \frac{\mu m_{\text{eff}}}{e} \Rightarrow \mu B > 2\pi \quad (2.54)$$

The amount of states inside an LL depends on the magnetic field. Basically, the DOS of the 2DEG condensates in the  $\delta$ -potentials and the states inside the Landau level can be estimated by multiplying the energy difference of two Landau levels with the DOS:

$$\frac{m_{\text{eff}}}{\pi \hbar^2} \cdot \hbar \omega_c = \frac{2eB}{h} \quad (2.55)$$

With successive increase of the magnetic field the highest, not fully occupied LL loses electrons to the next lower Landau level. When the level is emptied the Fermi energy first jumps between the two levels, leading to localized states, before reaching the next LL. The distance between the LLs increases with rising B, thus Landau levels move successively through the Fermi energy.

The important factor for the transport is the bending at the edges (see fig 2.10c). As long as the Fermi energy lies between the LL, no states are available for propagation *inside* the sample. However, at the edge the bands must bend upwards (otherwise the solid would "lose" electrons). Doing so, the bands hit the Fermi energy and enable transport. These states can be pictured as skipping orbits at the edge of the sample. Thus electrons are hopping along the edge of the sample and are localized (circling) inside the sample. The transport only takes place in the edge channels that carry the current in opposite directions. And due to the spatial separation of the edge channels the current flows dissipationless and the longitudinal resistance vanishes [Hal82].

Only when one Landau level is lifted to the Fermi energy, do free states become available over the whole sample. Therefore transport and scattering is enabled, giving rise to nonzero longitudinal resistance. This explains the observed Shubnikov-de Haas oscillations in the 2DEG. When a maximum occurs, a Landau level has hit the Fermi energy. For the minima,  $E_F$  lies between two Landau levels. The plateaux observable in

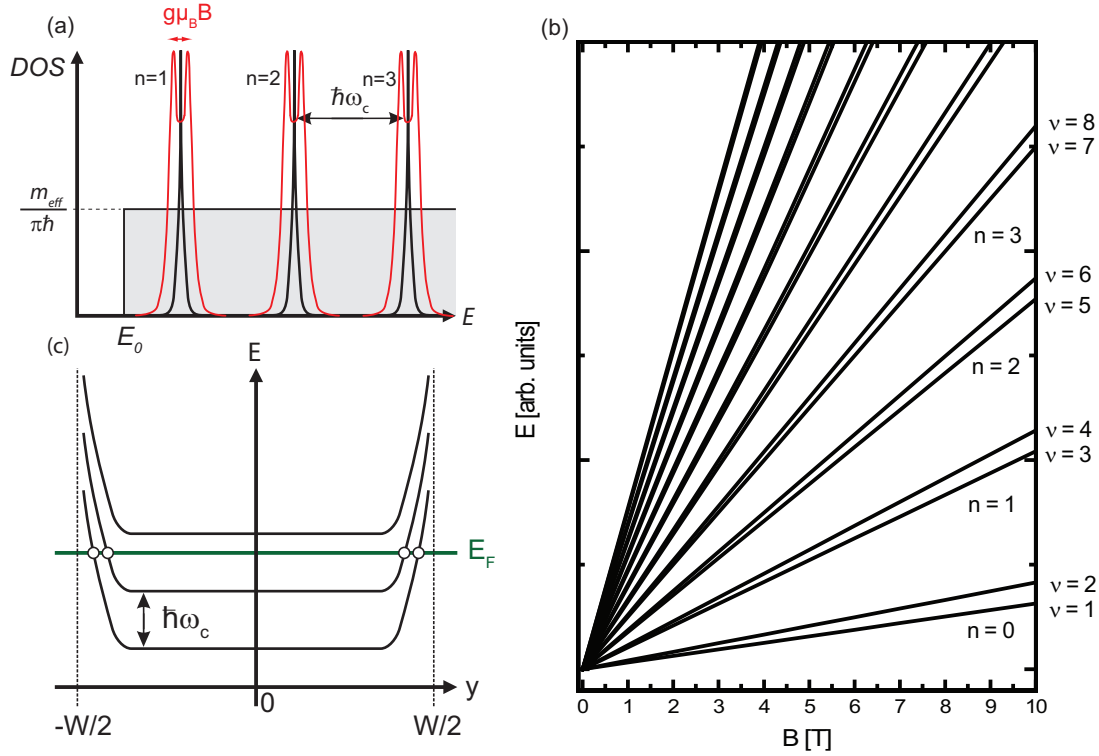


**Fig. 2.10:** (a) Density of states in the first subband of the 2DEG without a magnetic field (grey area) and with magnetic field (black peaks). For high  $g$ -factors and/or high fields the Landau levels split according to the spin direction (red lines); (b) exemplary Landau level chart with observable spin splitting, (c) the band bending at the edges of the sample leads to a crossing of the fermi energy at the edge of the sample.

the Hall voltage reflect the quantized conductance of the edge channels. Each channel can carry one conductance quantum which is  $2e^2/h$  for spin-degeneracy, and  $e^2/h$  otherwise. Due to the fact that the number of edge channels coincides with the number of occupied Landau levels, we obtain the Hall resistance as in (2.51).

From this follows that in fig 2.9 the plateau at  $R_{xy} = 2.151k\Omega = \frac{h}{(2.6)e^2}$  corresponds to 6 filled, spin-degenerated Landau levels and this Landau level furthermore hits the Fermi energy at about 4.5 T, where the maximum occurs in the longitudinal resistance.

Moreover the Shubnikov-de Haas oscillations offer an additional possibility to determine the carrier concentration. Dividing the carrier concentration by the number of states that each Landau level can carry (2.55) the amount of Landau levels is given. The amount of LL is decreased by one with the magnetic field increasing from one maximum to the next:



$$1 = \frac{n}{2eB_1/h} - \frac{n}{2eB_2/h} \quad (2.56)$$

$$n = \frac{2e}{h} \frac{1}{1/B_1 - 1/B_2} \quad (2.57)$$

Plotting the longitudinal resistance over  $1/B$  therefore gives an equal spacing between the Landau levels. Using FFT enables a very precise determination of carrier concentration. Especially useful is that the occurrence of a second subband or spin-orbit interaction can be ascertained because the LLs split separately and give two periodic functions in  $1/B$ .

#### 2.2.4 Local Hall Effect

The principle of the micro-Hall magnetometry relies on the classical Hall effect as described in chapter 2.2.2. The magnetic field penetrating the active Hall region can be determined when the electron density of the material is known. This allows for sensitive magnetic flux measurements of homogeneous magnetic fields as well as for strongly inhomogeneous fields (e.g. magnetic nanoparticles). For the latter the nanomagnet is typically prepared on the Hall cross that the emanating stray field penetrates the Hall cross area. In fig. 2.11 a sketch of such a device is depicted.

The current is driven in the x-direction and opposing probes detect the voltage in the y-direction. The z-component of the stray field emanating from the nanomagnet acts on the electrons moving with the drift velocity  $v_D$  by the Lorentz force and deflects them into the voltage leads. This results in a measurable Hall voltage  $V_H$  perpendicular to the current. The Hall voltage detects the changes in the stray field and can be seen as a "mirror of the magnetization" of the particle - thus magnetic hysteresis curves can be performed. The magnetic poles in the nanomagnet serve as the sources of the stray field. This penetrates the sensitive layer of the device - the two dimensional electron gas. The nanoparticle itself can be manipulated by an external magnetic field parallel to the 2DEG-plane since the Lorentz force vanishes in this configuration. Due to inhomogeneity of the magnetic field the equation for the Hall voltage (2.46) needs to be rewritten in the

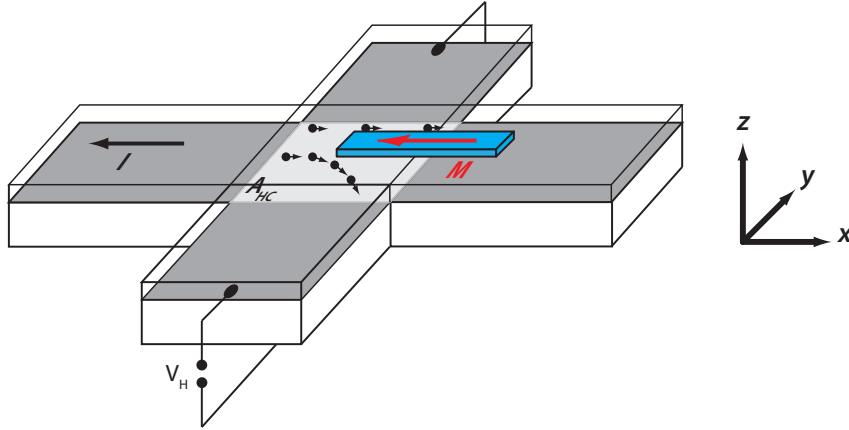


**Fig. 2.11:** Basic principle of a sensor based on micro-Hall magnetometry. The sensor area  $A_{HC}$  is in the plane of the current. The object of interest is placed in a way to force a deviation of the electron trajectories due to its stray field. Electrons passing at a decent distance are not affected.

following way:

$$V_H = -\frac{1}{ne}IB_{z,\text{eff}} \quad (2.58)$$

Here  $B_{z,\text{eff}}$  is called the effective field of the nanomagnet. This field is proportional to the integral of the  $z$ -component of the stray field over the sensor area as:

$$B_{z,\text{eff}} \propto \langle B_z \rangle = \frac{1}{A_{HC}} \int_{A_{HC}} B_z(x, y) dx dy \quad (2.59)$$

with the Hall-cross size  $A_{HC}$ . The Hall resistance  $R_{xy}$  then equals:

$$R_{xy} = \frac{V_H}{I} = -\frac{1}{ne}B_{z,\text{eff}} \quad (2.60)$$

with the electron density  $n$  of the 2DEG. The effective magnetic field (2.59) is not equal to the average field. The proportionality constant, however, depends on transport properties and can be determined. The next section gives an overview of this factor for different regimes and shall show how to achieve best signals for existing inhomogeneous stray fields.

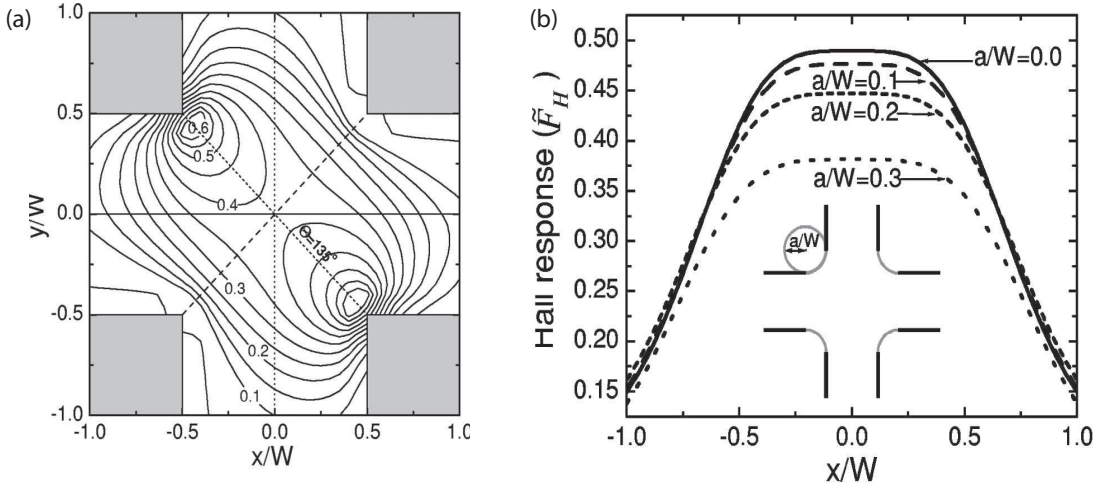


**Fig. 2.12:** Hall response functions taken from [CP02]; (a) exemplary contour plot of  $\tilde{F}_H$  for a weak magnetic dot, (b) Hall response along the center of the voltage probes for a magnetic dot placed in the center of the sensor for different radii of the circular corners.

### 2.2.4.1 Response Function $F_H$

Depending whether the mean free path is larger or smaller than the Hall cross geometry ( $l_e > W$ ,  $l_e < W$ ), two regimes have to be taken into account - the ballistic and diffusive, respectively.

For the diffusive regime, the Hall voltage does not reflect the average field  $\langle B_z \rangle$  from (2.59) for localized magnetic fields. Rather a reduced answer has been observed. This can be understood because the current reaches inside the voltage probes and thus effectively enlarges the sensor area.

The reduction can be incorporated in (2.60) by introducing the so called Hall response function  $F_H(x, y)$ , which is defined through the following formula:

$$R_{xy} = -\frac{1}{ne} \frac{\int \int dx dy F_H(x, y) B_z(x, y)}{\int \int dx dy F_H(x, y)} \quad (2.61)$$

$$= -\frac{1}{ne} \int \int dx dy \tilde{F}_H(x, y) B_z(x, y) \quad (2.62)$$

$\tilde{F}_H(x, y)$  is the normalized response function and exhibits the dimension  $m^{-2}$ .

Several groups performed numerical calculations [CP02, LGK<sup>+</sup>98, BO97] to determine  $\tilde{F}_H(x, y)$  for 2DEG-based MHM by scanning the diffusive sensor area with a magnetic

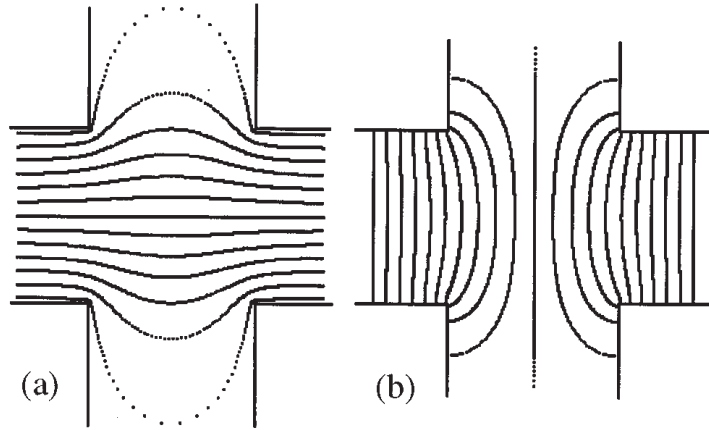


**Fig. 2.13:** Analytical calculation without a magnetic field of (a) the current density and (b) equipotential lines in the Hall cross. Figure taken from [TBM<sup>+</sup>97].

dot and calculating the arising  $R_{xy}$ . The Hall response function is a two-dimensional distribution function and shows the effective response to a magnetic field. It is, in general, a complicated function (see fig. 2.12a) and depends on the field strength as well as on the form of the localized magnetic field.

Remarkably,  $\tilde{F}_H$  is a smooth function which is constant only in the center of the Hall cross. As depicted in fig. 2.12b it decays from the constant value in the middle towards the edges of the sensor. For a corner radius  $a/W = 0$  of the Hall cross  $\tilde{F}_H$  equals about 0.5 in the center. This means that the Hall response in the diffusive regime is reduced by one half compared to homogeneous fields. Increased corner radii substantially lower the response (e.g. for  $a/W=0.3$  the signal is about 25% lower). For a radius of  $a/W$  of 0.1 the response function is not changing significantly from 0.5. As a result, the edges of MHM devices should be fabricated with  $a/W \leq 0.1$  or as abrupt as possible.

Asymmetric Hall crosses affect the signal as well. For a width ratio 0.3 of the voltage vs. the current leads, the response at the edge is enhanced by up to 300 % while the center loses sensitivity. This can be understood in the diffusive regime due to the scattering events which the electrons undergo. The result is that the current density is highest in the leads and widens into the voltage leads (compare fig. 2.13). Round corners lead to the same result - a lower current density.

However, a position independent signal is desirable for measurements. Therefore sym-

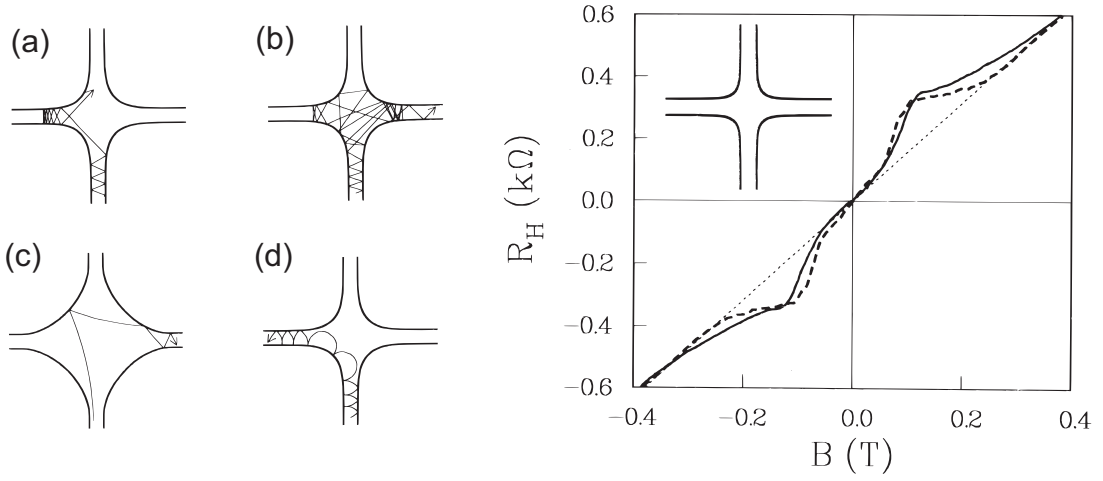


**Fig. 2.14:** (a)-(d) trajectories for electrons that experience only sidewall scattering exhibit different transmission probability only depending on the shape of the corner. Right:  $R_{xy}$  (here denoted as  $R_H$ ) for round corners exhibiting a last plateau. Taken from [BvH91].

metric Hall crosses were chosen in this work.

Calculating the average magnetic field flux over the area of the Hall cross  $w^2$ :  $\langle B_z \rangle = \frac{1}{A_{HC}} \int \int B_z(x, y) dx dy$  the gained Hall voltage is reduced to  $V_H = R_H I \langle B_z \rangle / 2$ . This can be understood as an effective increase of the Hall cross size due to the current distribution which protrudes into the voltage leads as well (see fig. 2.13).

The Hall response in the pure ballistic regime is different when the mean free path exceeds the size of the Hall cross area. Using the theory of Landauer-Büttiker formalism Peeters et al. [PL98] analyzed the response of the device to inhomogeneous fields. They found out that the Hall voltage is fully determined by the average magnetic field over the cross - no matter what the magnetic field flux distribution looks like. Therefore - using the formulation in (2.62) we can state that the Hall response function equals 1 inside and 0 outside the Hall cross. That means the signal in the ballistic regime is at least twice as high as in the diffusive regime. This is because in ballistic transport electrons do not undergo any scattering events. Then the current density will not be distributed into the voltage leads, entailing a homogeneous current distribution over the full Hall cross.

Due to the above, asymmetric Hall cross shapes do not affect the operation either and rounded corners down to  $a/W = 0.2$  have nearly no effect - by means of current distri-

bution. But the electrons can undergo complicated scattering events for round corners as it has been described by the billiard-model [BVH89]. These scattering events at round corners were responsible for deviations of the Hall resistance from linear in B behavior (see fig. 2.14). Thus it is obvious that large radii also decrease the performance of the micro magnetic sensor in the ballistic regime.

#### 2.2.4.2 Magnetic Field Flux and Flux Resolution

In this section the possible magnetic field flux and flux resolution shall be discussed. The resolution is determined by the electronic noise on the measurement signal - the Hall voltage. It can be written as:

$$V(t) = V_H(t) + V_N(t) \quad (2.63)$$

where  $V(t)$  is the measured time-dependent voltage and consists of the Hall voltage and a noise voltage  $V_N(t)$ . The absolute theoretical limit of  $V_N(t)$  is the intrinsic voltage noise of the sample. It consists mainly of temperature-dependent Johnson noise [OBH96]:

$$V_N = \sqrt{4k_B T R_S \Delta f} \quad (2.64)$$

$k_B$  is the Boltzmann constant,  $R_S$  is the series resistance of the Hall sample and the measurement bandwidth  $\Delta f$ . This holds true for currents below  $I_{crit}$ , where the sample is substantially heated up.

The signal to noise ratio (SNR) is then is the quotient of the noise over the signal:

$$\text{SNR}(T) = \frac{I R_H B_{z,eff}}{\sqrt{4k_B T R_S \Delta f}} \quad (2.65)$$

For an SNR of 1 the minimum detectable signal change is obtained. Therefore the ultimate limit for the magnetic field resolution is:

$$B_{min} = \frac{\sqrt{4k_B T R_S \Delta f}}{R_H j_{max} w} \quad (2.66)$$

The current  $j_{max}$  is limited by the Joule heating of the device and is given as  $\rho_{xx}j_{max}^2 = p_{max} = const.$  Here  $p_{max}$  is the maximum amount of heat that the device can deduct per unit area and is a constant. When substituting  $R_S = \frac{1}{ne\mu} \frac{l}{w}$ ,  $R_H = (ne)^{-1}$  and  $j_{max} = \sqrt{ne\mu p_{max}}$  the minimum detectable magnetic flux is:

$$B_{min} = \frac{1}{\mu w} \sqrt{\frac{4k_B T \Delta f l}{p_{max} w}} \quad (2.67)$$

Investigating (2.67) it is obvious that the best field resolution is achieved for a large Hall cross area, high electron mobility material and low distances between the contacts.

It must be noted, though, that additional noise in micrometer-sized Hall crosses arises due to generation recombination and 1/f-noise, which can excel the thermal noise as investigated in [Rah05, Mih06]. Experimentally  $B_{min}$  is derived by the noise of the measurement. Nevertheless, the main aspects of this short discussion hold true for the different noise sources: the higher the electron mobility and the larger the Hall cross size, the lower the  $B_{min}$  - the higher the field resolution.

But this conclusion is only correct for homogeneous fields and fails for localized ones. As already mentioned in (2.25) the average magnetic field is proportional to the inverse area  $A_{HC}$  of the Hall sensor:

$$\langle B_z \rangle = \frac{1}{A_{HC}} \int_{A_{HC}} B_z(x, y) dx dy \quad (2.68)$$

Thus smaller Hall sensors optimize flux trapping and are preferably suited to measure strongly localized fields. One possible figure of merit is the flux sensitivity. With the magnetic flux  $\Phi = B \cdot A$ , the sensor area is taken into account and the magnetic flux sensitivity can be expressed in units of flux quanta  $\Phi_0 (= h/2e \approx 2.07 \cdot 10^{-15} Tm^2)$ . The minimum detectable flux penetrating the sensor area then equals:

$$\Phi_{min} = B_{min} \cdot A_{HC} \quad (2.69)$$

Another possibility to express the capability to detect inhomogeneous fields is in respect to the magnetic moment resolution. Here the average magnetic field emanating from a spheroid particle with magnetization  $m$  (2.28) is set in relation to  $B_{min}$ . In this factor not only the Hall cross area but also the distance  $z$  to the sensor is implemented. Therefore the minimum magnetic moment resolution  $m_{min}$  can be determined in units of elementary magnetic moments  $\mu_B$ .

$$m_{min} = \frac{\mu_0}{4\pi B_{min}} \frac{w^4 + 6w^2 + z^2 + 8z^4}{\sqrt{\frac{w^2}{2} + z^2}} \quad (2.70)$$

Using these three figures of merit for sensitivities, the following sensors will be characterized.

Summarizing, this section dealt with the theory and yielded important parameters for the investigation of small nanomagnets (corner radii, ballistic transport, small  $A_{HC}$ ). The next section will describe the fabrication of the produced micro-Hall sensors.

## 2.2.5 Fabrication

In the beginning macro-Hall bars based on InAs 2DEG were fabricated to get an idea of the sample fabrication and measurement method. After successful tests, the flux sensitivity and magnetic moment resolution was optimized by decreasing the Hall cross area using high resolution ebeam lithography. Subsequently, high quality HgTe 2DEGs were also tested for MHM suitability. Here the fabrication of the sensors on the two different semiconductor heterostructures will be discussed.

### 2.2.5.1 InAs 2DEG Macro-Hall Bars

The macro-Hall bars were fabricated by an all optical lithography process (the process parameters are listed in A.1 in detail).

The first optical lithography step was carried out using a positive-tone resist to prepare the contacts. InAs has the unique property of the Fermi energy lying within the conduction band. This was exploited in order to obtain ohmic contacts on this material.



First the cap layer made of (Al,Ga)Sb is etched with high selectivity against InAs by tetramethylammoniumhydroxide (a typical developer). Subsequently the exposed InAs-2DEG layer is protected against oxidation by sulfuric passivation using ammonium sulfide [LBH95, PYW03]. The obtained contacts were investigated before and exhibit ideal ohmic behavior [Bib00]. The contacts are deposited by electron beam evaporation of Ti/Au in UHV and subsequent lift-off. In the next step the Hall bar mesa is fabricated with a current channel width of 100  $\mu\text{m}$  and voltage probe width of 30  $\mu\text{m}$ . The distance  $L$  between the voltage probes was 300  $\mu\text{m}$ . The following wet chemical etching of the Hall bar mesa used the same etchant for AlGaSb and following succinic acid for the InAs 2DEG. Due to the position of the Fermi level, prior to applying the magnets an insulating layer needed to be incorporated in order to inhibit parallel conductance via the magnet. The insulator is deployed using PECVD (plasma-enhanced-chemical-vapor-deposition) of 25 nm  $\text{Si}_3\text{N}_4$ . Subsequently CoFe-magnets with a Pt capping layer (to prevent oxidation) are sputtered on the Hall bar, using a two-layer image reversal process to provide an unproblematic lift-off. In the last fabrication step the sample is glued inside a chip carrier using GI-Varnish and contacted by ultrasonic bonding using Au-wire.

### 2.2.5.2 InAs 2DEG Micro-Hall Bars

After successful measurements the next step was the miniaturization, using high resolution electron beam lithography (EBL) and highly anisotropic etching processes, in order to obtain sensors with increased sensitivity for localized fields. The EBL facility is based on a scanning electron microscope (SEM) Leo 1525 from Zeiss equipped with a pattern generator from Raith (for details see [Büt05]). The process flow is sketched in fig. 2.15. At first the contacts are performed in the same way as for the macro-Hall bars using a mask that offered alignment marks for EBL. The PMMA (polymethyl metacrylate) etch mask for the Hall bar was structured by positive EBL. Therefore the resist was exposed around the Hall bar structure in order to minimize disturbance of the 2DEG. Following the Hall bar mesa is fabricated by dry etching in order to obtain the smallest possible radii for better sensitivity as discussed in (2.12). After deploying the  $\text{Si}_3\text{N}_4$ -insulator via

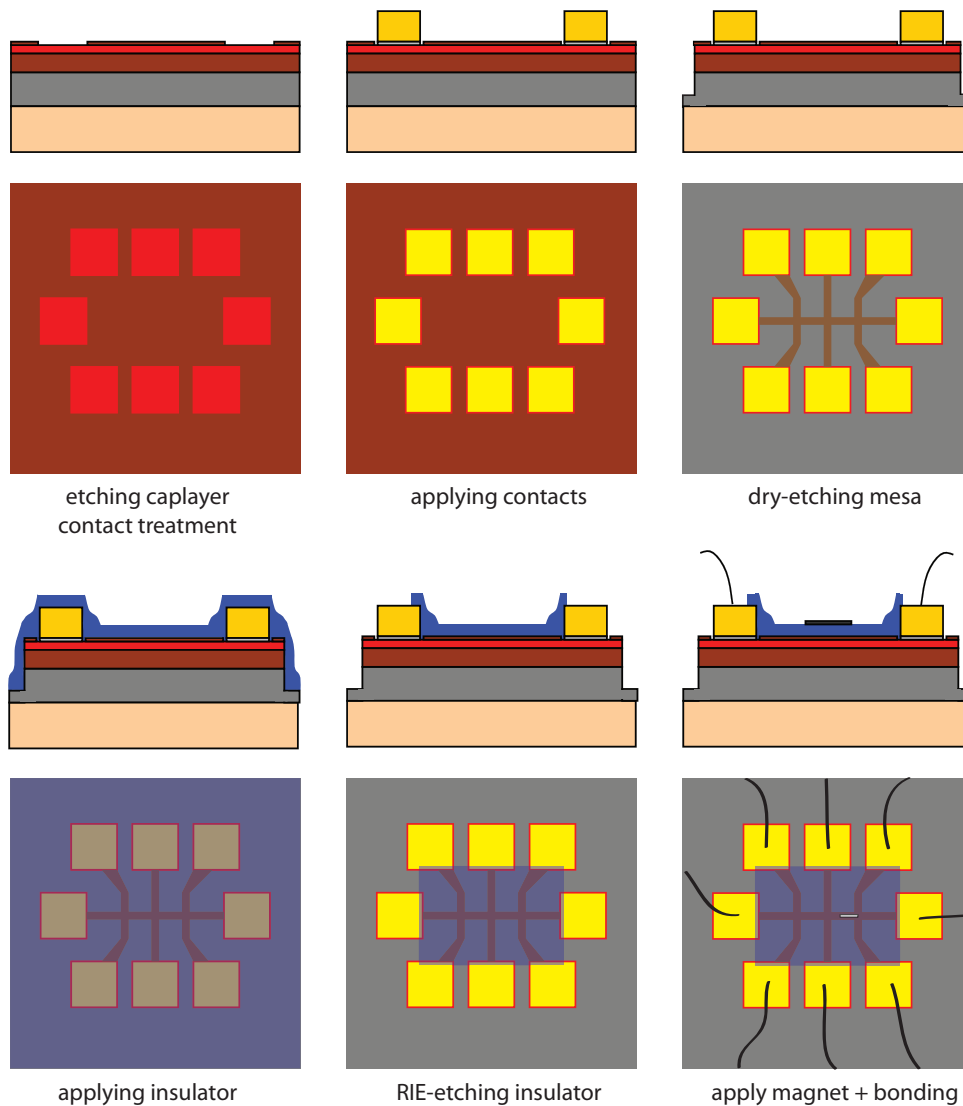


**Fig. 2.15:** Process flow for the fabrication of MHM sensors on InAs 2DEG.

PECVD the micromagnets with sizes of e.g.  $500 \text{ nm} \times 30 \text{ nm} \times 5 \text{ }\mu\text{m}$  were deposited on Hall bars with high alignment accuracy. Similar to the optical two-layer resist system for the macro-Hall bars the magnet was sputtered using a PMMA bilayer system as a mask to ensure an undercut. The sample fabrication finishes with gluing the sample inside a chip carrier using GI-Varnish and ultrasonic bonding.

### 2.2.5.3 HgTe 2DEG Micro-Hall Bars

The process for the fabrication of Hall-sensors based on HgTe differs from the one before (InAs). This is because ohmic contacts are carried out in the last step here (see fig. 2.16). After cleaning and spinning PMMA resist on the 3 x 5 mm sample the micro-Hall bar is defined using a positive low-voltage (2.5 keV) electron beam lithography exposure. Then the etch mask (15 nm of Ti) was deployed by lift-off in order to achieve good contrast for the alignment in the mask aligner. The subsequent cleaning of the samples in warm methylisobutylketone (MIBK) and isopropanol (IPA) was found to be crucial to facilitate reproducible contacts. After deploying the etch mask of the inside mesa, the outer etch mask was produced by a low temperature optical lithography process, evaporation of 10 nm Ti and lift-off. The structure transfer was carried out by dry etching in a self-built Ar-sputtering facility. Diluted hydrofluoric acid was then used for stripping the etch mask. In case of HgTe the insulator was unnecessary because the capping layer of the MBE-grown sample ensured good electronic insulation against the 2DEG. Therefore the last step is the fabrication of the magnet via EBL. Contrary to the bilayer system before, a thin single layer PMMA resist and low voltage exposure (2.5 keV) ensures easy lift-off. Due to changes in the sputtering targets the magnetic material was changed to Permalloy (NiFe), exhibiting saturation magnetizations of the same order.

Additionally, one sample was equipped with a gate to investigate the effect of various carrier concentrations. Therefore a 110 nm thick insulator consisting of a superlattice of  $Si_3N_4/SiO_2$  was deployed by PECVD. The same optical lithography process as for the outer etchmask provided the gate structure.

After gluing the sample inside the chip carrier the ohmic contacts were performed by thermal In bonding.

## 2.2.6 Experimental Setup

The chip carrier used offers a maximum of 18 contacts for the external measurement setup. A sample holder is depicted in fig. 2.17, where the 18 contact pads can be addressed. According to the contacts, a cable with 18 shielded lines is drawn to the computer-based mea-

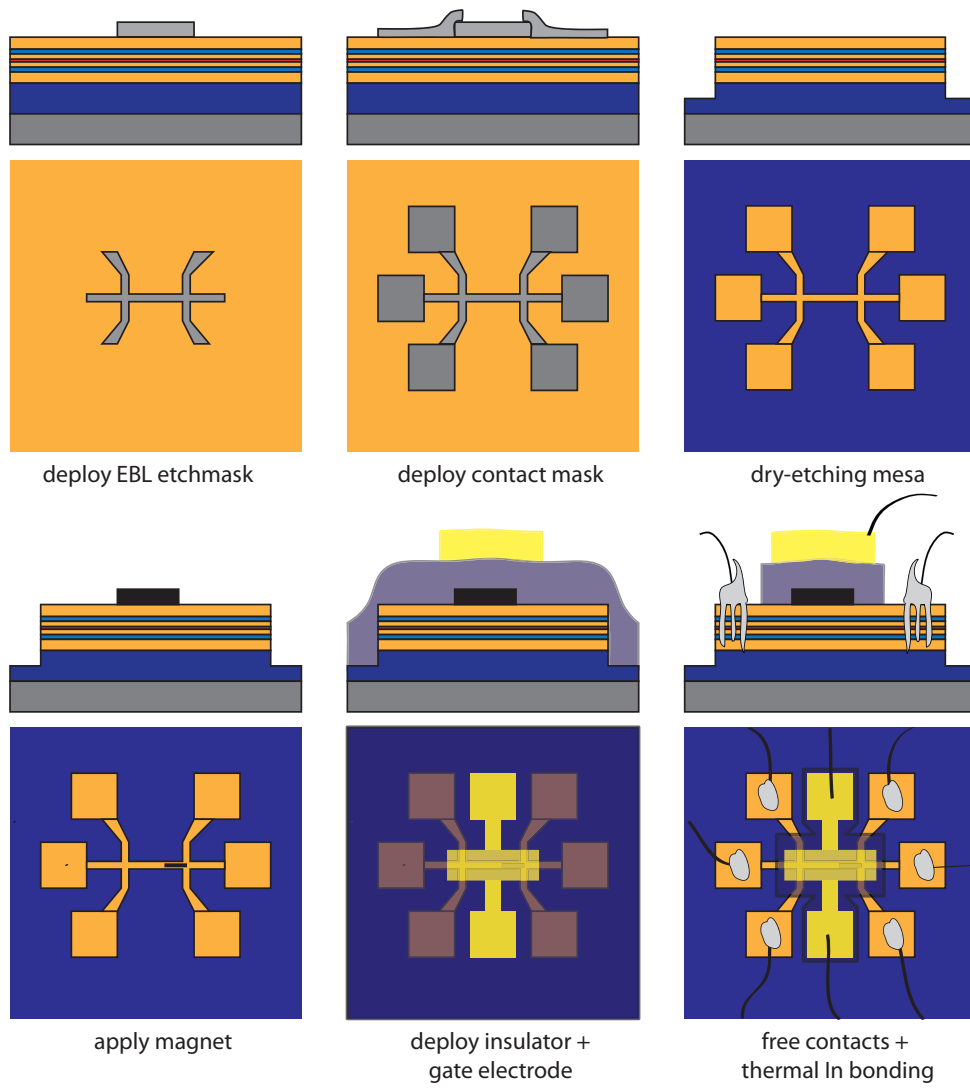


**Fig. 2.16:** Process flow for the fabrication of MHM sensors on HgTe 2DEG.

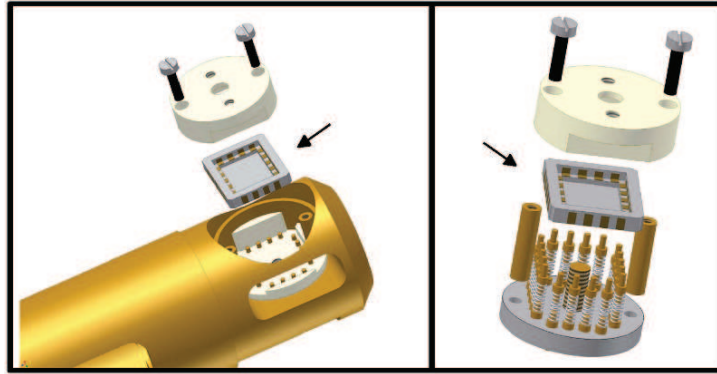


**Fig. 2.17:** Sample holder for the characterization, the arrows point to the chip carrier where the sample is glued inside. Right: Contacts of the chip carrier are done by pins mounted on springs.

surement setup. It allows characterization measurements with variable magnetic fields, several applicable voltages and simultaneous detection of four voltages. It is based on a computer, equipped with a voltage card Adlink 6208V (offering 8 channels  $\pm 10$  V with a resolution of 16 bit), a GPIB-card from National Instruments for the communication with two nanovolt-/microohmmeters Agilent 34420A and the temperature controller ITC 503 from Oxford. The measurement control was performed by a self-written LabVIEW program which allows for automated measurement with swept, stepped parameters and temperature control.

For low temperature measurements a  $^4\text{He}$  bath cryostat has been used. With its variable temperature insert from JANIS, temperatures from 1.5 K to 300 K could be obtained by pumping via a rotary pump or using the built-in heater. The Oxford ITC 503 was connected to the heater regulating the temperature via its PID controller. The cryostat was equipped with superconducting coils and an Oxford 120 power supply delivering magnetic fields up to 5 T. Moreover, self-made low-offset power supplies were used for hysteresis measurements with magnetic fields in the range of  $\pm 500$  mT. Two sample-sticks were available, one offering in-plane and the other out-of-plane geometry of the magnetic field. The setup is depicted in fig. 2.18.

The electrical setup consists of an 18 contact switchbox where voltages could be applied and detected. The output voltage of the voltage card was limited by 1000:1, 100:1 and 10:1 voltage dividers in order to decrease the offset of the Adlink 6208V and limit the

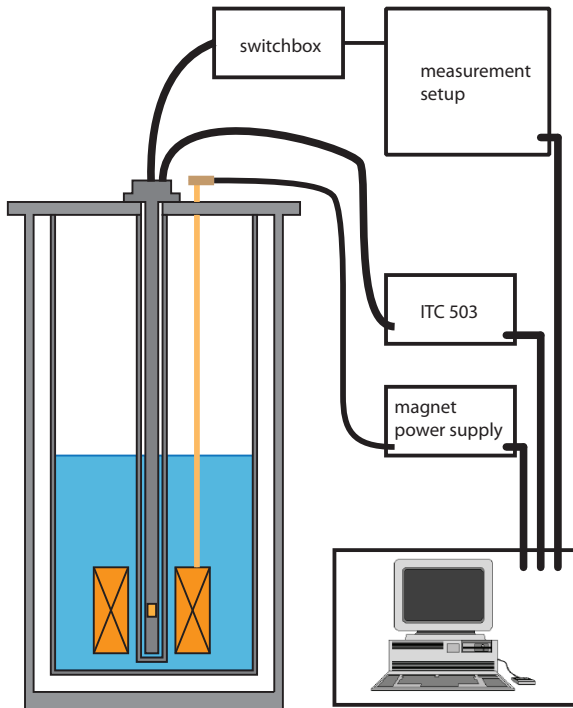


**Fig. 2.18:** Scheme of the low-temperature measurement setup. The cryostat has an outer and inner vacuum chamber for variable temperature measurements. The sample stick is immersed inside the cryostat in absence of  $^4\text{He}$  to prevent other gases to solidify.  $^4\text{He}$  is injected by a connection to the bath controllable via needle valve. The heater sits below the sample stick which is equipped with a temperature sensor. The sensor is read by the ITC 503 which controls the heater as well. The electrical contacts are accessible via a switchbox which is connected to the measurement setup. The computer controls the magnetic field of the superconducting coils, the applied voltages and collects the measurement data.

applied voltage. The voltage was applied to a reference resistor and the sample in series. The magnitude of the reference resistor was always chosen to be equal to or lower than the sample resistance. The voltage measurements in this DC-setup were performed with low-noise, low-offset, operation-amplifier-based instrumentation amplifiers which referenced the incoming voltage difference to ground. The probes were measured by two Agilent 34420A nanovoltmeters which enable the simultaneous measurement of four voltages (two channels each). The intrinsic noise of the setup was found to be in the order of some 100 nV.

For room-temperature measurements, a similar sample holder and comparable measurement setup was used. Here the magnetic field was applied by an electromagnet with an iron yoke. Due to the hysteresis of the magnet, the commercially available Hall sensor Infineon TLE4990 was used for the determination of the magnetic field.

### 2.2.7 Measurements and Discussion

In the following section the measurements obtained using MHM shall be discussed. Starting from the macro-Hall bars the first ideas of the measurement principle and the analysis

of the obtained data will be enlightened. The aim of higher flux sensitivity asks for miniaturized Hall bars and nanoscale magnets. Here the peculiar switching due to single domain states will be shown. In the end the flux and magnetic moment resolution is estimated.

### 2.2.7.1 Analysis of the Measurement Data

As mentioned before, the Hall voltage is a mirror of the applied magnetic field perpendicular to the plane of the Hall device. The magnetic field can be determined with knowledge of the carrier density in the device. Therefore the first step was to determine the carrier density of the 2DEGs by standard Hall measurements in a homogeneous field perpendicular to the sample plane. Subsequently, the orientation of the magnetic field is switched in-plane in order to manipulate the magnetization of the magnet. Even though the effect of the magnetic field should be zero for the bare Hall cross (vanishing Lorentz force)  $R_{xy}$  still exhibits a linear magnetic field dependence. This can be accounted to not 100% parallelism of magnetic field and current. It can be explained by the gluing in the chip carrier since the misalignment can be estimated by the measurement to be smaller than  $1^\circ$ . Thus the linear part is subtracted for magnetic fields where the saturation magnetization of the magnet is reached.

The measurement curve should now be symmetric to the abscissa. However, due to non negligible voltage offsets and slightly off voltage leads an offset occurs. This has been corrected in the following as well. Using the known carrier concentration the obtained signal can now be recalculated into the effective magnetic stray field  $B_{z,eff} = -neR_{xy}$ . The noise of the measurement  $N$  is obtained by the standard deviation of a time-dependent measurement; or, alternatively, by the standard deviation for constant  $R_{xy}$  in the saturation of the hysteresis. The minimum detectable field then equals  $B_{min} = -neN$ .

### 2.2.7.2 Macro-Hall Bars

The first magnetometry measurements were obtained for three macroscopic Hall bars with magnets of cobalt iron ( $L = 300 \mu\text{m}$ , thickness =  $50 \text{ nm}$ , widths:  $20$  and  $50 \mu\text{m}$ ) in order

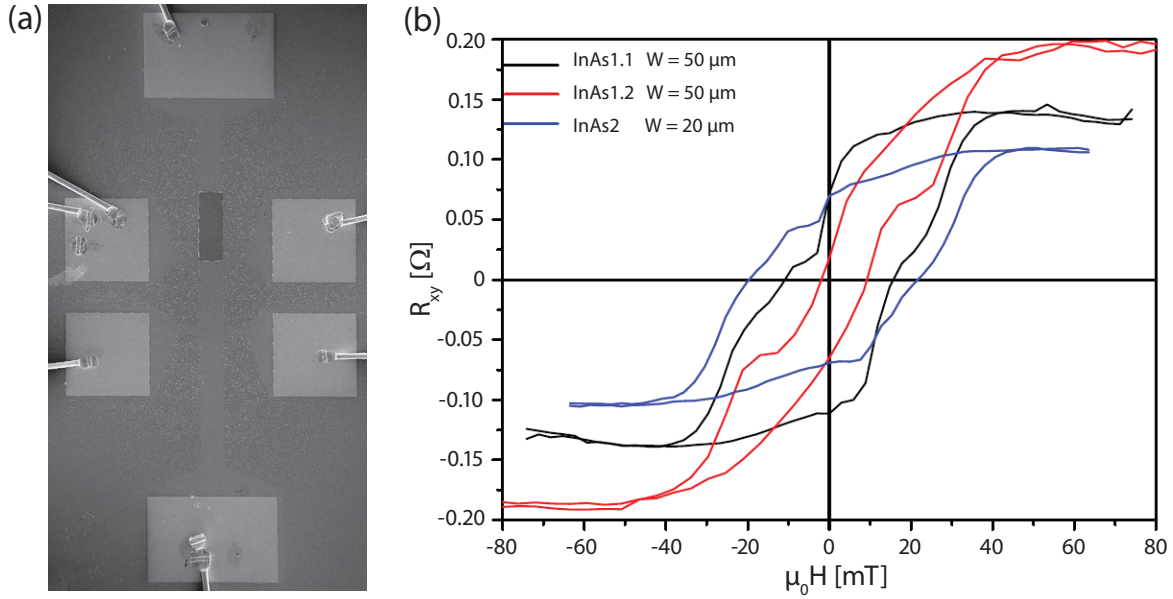


**Fig. 2.19:** (a) Micrograph of a  $100 \mu\text{m}$  wide macro-Hall bar with CoFe magnet on top, (b) measurements on magnets with different widths.

to get an idea of the key points of Hall magnetometry.

The hysteresis measurements with up and down sweeps of the three magnets at  $T = 4.2 \text{ K}$  are depicted in figure 2.19. At first sight, the samples exhibit multi domain behavior with domain movements and pinning/depinning processes, visible by smooth variations and abrupt jumps of the Hall resistance, respectively. Furthermore, all samples show constant magnetization at  $H > 40 \text{ mT}$ , where the saturation magnetization of the CoFe magnet is reached. In addition, the features in the up and down sweeps show the expected symmetric behavior. It must be noted that the (black) and (red) curve, though from nominally identical samples, show very different saturation magnetization and coercive fields. The deviations are much larger than lithographic errors could explain due to shape anisotropy (coercive field) or width (saturation magnetization). Sidewalls, leading to complicated end domain structures, can also be excluded due to the reliable bilayer process and visual confirmation by microscope. The reason was then found to be the sputtering target that led to an increasing contamination with Cu because of inhomogeneous degradation in the sputtering process.



Summarizing, Hall magnetometry measurements were undoubtedly obtained for macro-Hall bars showing the typical magnetization behavior of multi domain magnets. Even though the measurements did not allow for a quantitative analysis, they served to prove the principle before heading to micro-Hall bars which will be discussed in the next section.

### 2.2.7.3 Micro-Hall Bars

The sensitivity of the Hall sensors is inversely proportional to the Hall cross area. It is obvious that the investigation of nanoscale magnets asks for sensor sizes in the same dimensions. The movement of electrons obeys then a different regime, the quasi-ballistic/ballistic one. This section shows the results obtained with InAs-2DEG micro-Hall-Bars and deals with the properties of small magnets.

The fabricated micro-Hall bars were downscaled by a factor of 100, compared to the macro-Hall bars, and exhibited widths of a few micrometers. The mean free path of the electrons in the 2DEG (2.38) with a carrier concentration  $n \approx 1 \cdot 10^{12} \text{cm}^{-2}$  and mobility  $\mu \approx 1.5 \cdot 10^5 \text{cm}^2/\text{Vs}$  equals about  $2 \mu\text{m}$  and is comparable to the Hall cross size. In this regime, the rounding of the corners does not only play an important role for the signal strength at room-temperature (see fig. 2.12) but also leads to falsifying results because of backscattering due to ballistic transport in weak magnetic fields ("electron billiard"). These ballistic effects are known to be responsible for the so-called "last-plateau" in the Hall resistance.

This behavior was observed for the first series that had been wet etched and exhibited significant roundings at the voltage leads. The Hall resistance is plotted as the red line in fig. 2.20. The observed non-linearity is an unwanted side-effect and can give rise to wrong signal analysis. Thus the fabrication process was altered to dry etching where the roundings could be suppressed efficiently (see fig. 2.20a). The corresponding Hall resistance is the black line and recovered the full linearity at low magnetic fields. Furthermore, the mobility of the sample based on the same substrate increased and argues that the dry etching leads to more specular edges of the current channel. Moreover, the offset was found to be dramatically reduced, due to better Hall cross shape definition.

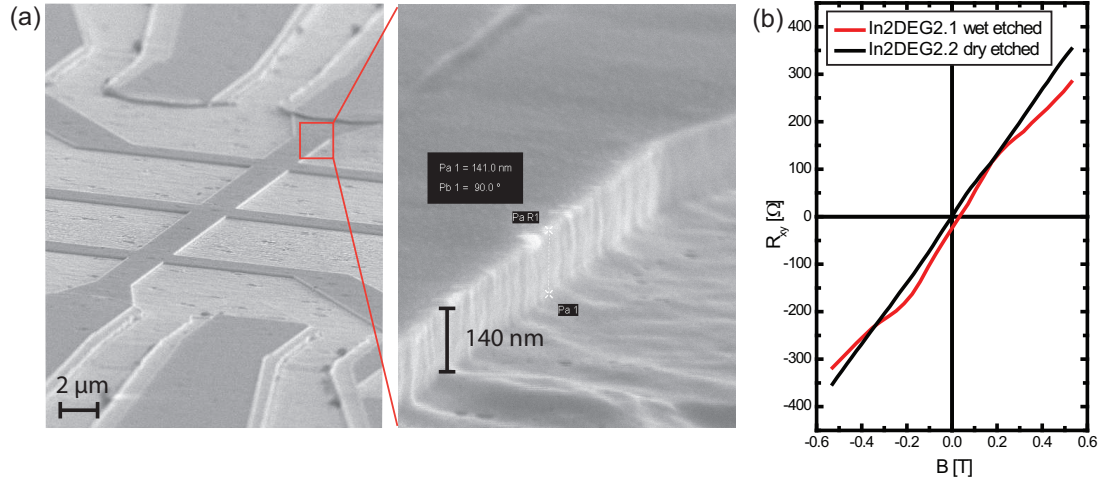


**Fig. 2.20:** (a) SEM picture of the edges resulting from dry etching (b) Hall measurements for wet etched and dry etched Hall bars with the same nominal geometry.

The following Hall bars were therefore all fabricated by dry etching.

Proceeding to magnetometry, several micro-Hall bars with applied nanomagnets were investigated. For comparable results, the samples were processed as parallel as possible to prevent any unwanted differences (e.g. thickness variations of the magnets).

In fig. 2.21 the measurements of nominally identical 2 μm wide micro-Hall bars, fabricated on the same sample, undergoing the same sputter deposition of 50 nm CoFeB, are depicted. When first investigating the widest magnet (blue curve), the reversal of magnetization is affected by propagation and annihilation of domain walls - similar to the macro-Hall bars presented before. The continuous shape speaks for domain wall movement and rotation of the magnetic moments inside the specific domains. In comparison, the curves for magnets with widths of 0.5 (red) and 1 (black) μm show a rectangular switching behavior - the sign of single domain particles. The abrupt jumps are the sign for coherent rotation of all spins. The magnet thus exhibits single domain behavior which becomes favorable for small dimensions, as discussed in section 2.1.4.

The effect of shape anisotropy leads to an increase of the coercive field because the creation of a domain wall with its concomitant exchange field is less favorable for smaller

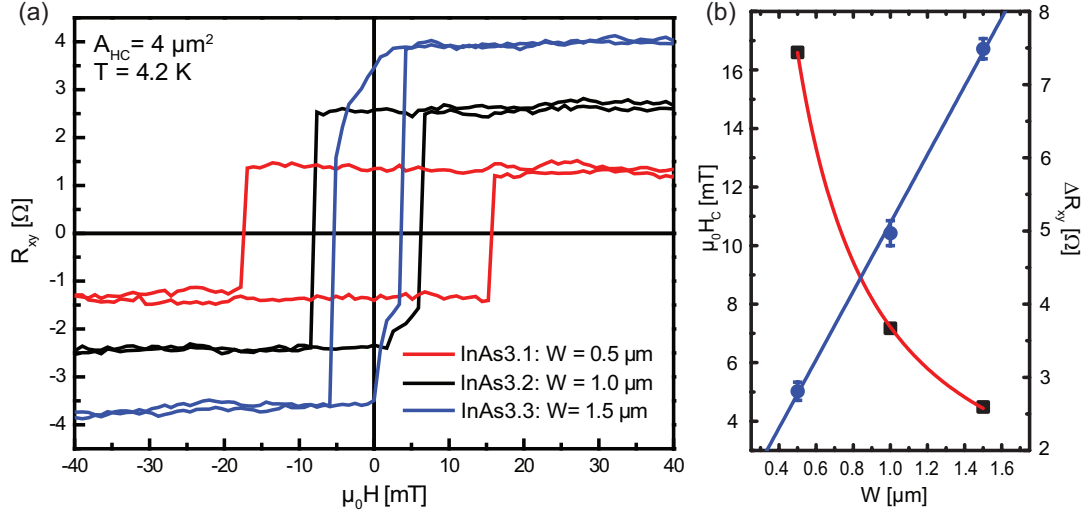


**Fig. 2.21:** (a) Hysteresis curves of identical micro-Hall bars on InAs 2DEG, dimension of Hall cross equals  $(2 \cdot 2) \mu\text{m}^2$  for all measurements; CoFeB-magnets were 0.5 (red), 1.0 (black) and 1.5 ( $\mu\text{m}$  wide, 50 nm thick and 9  $\mu\text{m}$  long. (b) extracted coercive fields in dependence of the width (black squares), the red line depicts the progression predicted for the upper bond in fig. 2.3. progression of signal strength (blue circles).

widths (see section 2.1.3.2). The coercive field of the three magnets can be fitted by the progression of the upper bond predicted by Brown for an infinite ferromagnetic slab [Bro64] as indicated by the red line in 2.21b. In addition, the signal height for the black (blue) curve doubles (triples) the signal of the smallest magnet in agreement with the theory. This is because the strength of the stray field is proportional to the cross-section  $w \cdot t$  of the magnet.

The influence of the sensor area is depicted in fig. 2.22. The identically processed samples differ only by the Hall cross area  $A_{HC}$ . The hysteresis curve shows nearly the same coercive fields - the small difference is due to fabrication tolerances. Obviously, the signal of the identical stray fields differs significantly because of the averaging over the Hall cross area. As plotted in fig. 2.22b the signal strength can be fitted linearly on the inverse Hall cross size. This is the expected result from equation (2.59) in case of constant response function  $\tilde{F}_H$ .

Subsequently, the experiments were carried out at room temperature. Measurements of samples InAs3.1 and InAs3.2 are depicted in fig 2.23. For comparison, the curves for

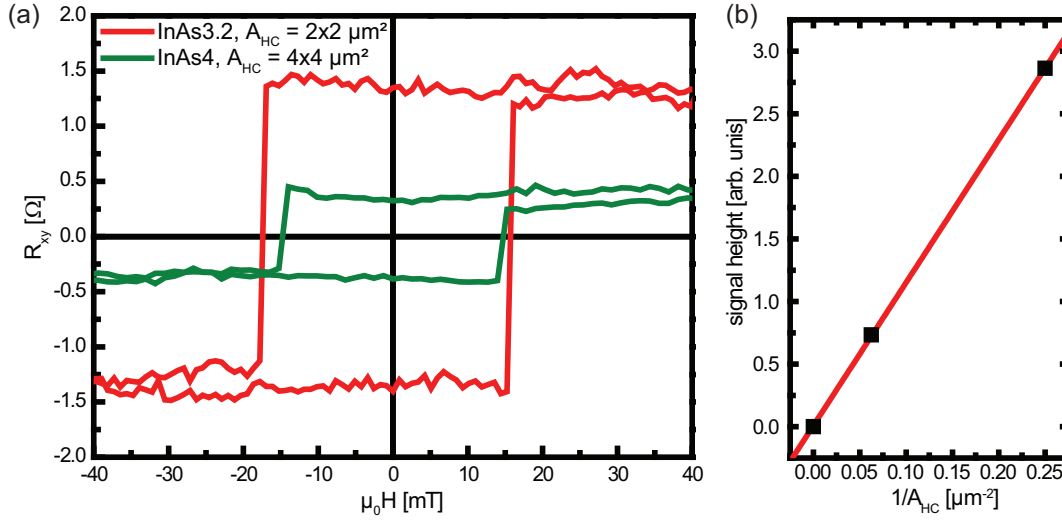


**Fig. 2.22:** (a) Hysteresis curves for the nominally identical magnet (CoFeB, width  $0.5 \mu m$ , length  $9 \mu m$ , thickness  $50 nm$ ) on a Hall cross with area of  $16 \mu m^2$  (InAs4, green) and  $4 \mu m^2$  (InAs3.2, red); (b) signal height depending on  $A_{HC}$  with linear fit. The point for infinite  $A_{HC}$  has been inserted for clarity.

low temperatures are plotted as well.

First, the coercive fields decrease due to thermal energy supporting the nucleation of a domain wall. The difference in the signal strengths between the two temperatures is remarkably strong. The measurements differ by a factor of about 20 - more than the change from diffusive to ballistic covers. Indeed, the stray field signal of the CoFeB magnet used is supposed to decrease slightly with higher temperatures but cannot explain the extent. The most plausible explanation is therefore an increased carrier concentration at high temperatures. In order to prove this hypothesis standard Hall measurements at room temperature were carried out and showed a dramatic increase of the carrier concentration from  $1.0 \cdot 10^{12} cm^{-2}$  to about  $2.1 \cdot 10^{13} cm^{-2}$  - a factor of 21. The reason was found to lie in parallel conductance of the substrate because measurements between contacts isolated from each other exhibited a resistance of only  $1.6 k\Omega$  at room temperature. It must be stated that with this design of the 2DEG substrate, a quantitative analysis of stray fields at room temperature is not possible. That is due to the different mobility in the substrate as well as the undefined current path inside the sample. An improvement could be made by optimizing the insulation of the 2DEG by incorporating insulating layers during the

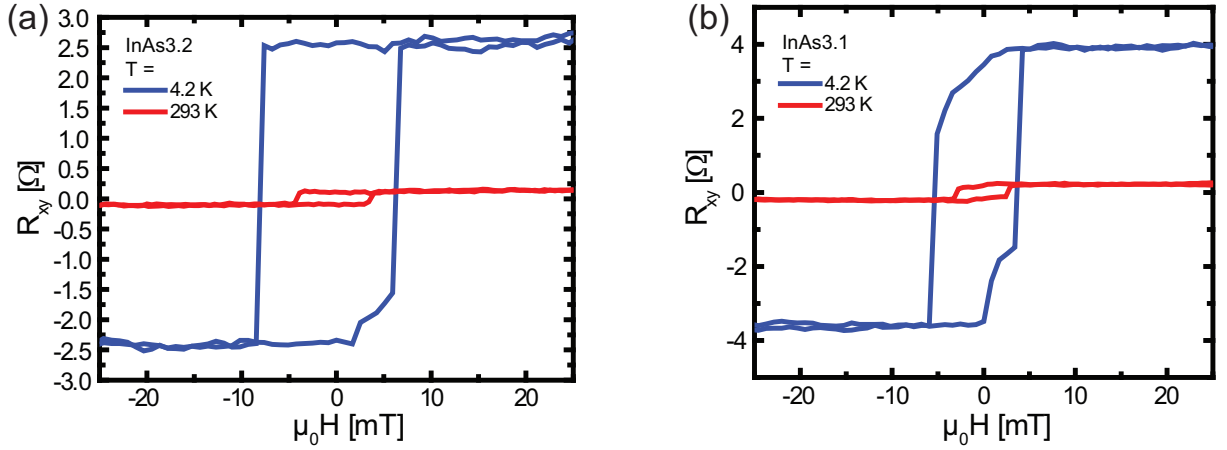


**Fig. 2.23:** Measurements at room temperature and 4.2 K of (a) a 1.0 and (b) 1.5  $\mu\text{m}$  wide magnet on a Hallcross with  $A_{HC} = 4\mu\text{m}^2$ .

growth process and deeper etching in the fabrication process.

For two exemplary samples the noise and resolution limits are investigated in closer detail in table 2.1. The noise  $N$  has been determined by the standard deviation in the region where the saturation magnetization was reached. The signal height is measured as the median of the two steps for up and down sweeps. By knowing the noise of the measurement and the carrier concentration (here  $n = 1.0 \cdot 10^{12} \text{cm}^{-2}$ ), the smallest detectable average field  $B_{min} = n_e e N$  as well as the minimum flux  $\Phi_{min}$  (2.69) were obtained. The minimum magnetic moment resolution was derived following equation (2.70). This analysis has been omitted for room temperature. The 16  $\mu\text{m}^2$  exhibited the lower noise

sample	$A_{HC}$ [ $\mu\text{m}^2$ ]	T [K]	signal S [ $\Omega$ ]	noise N [ $\Omega$ ]	SNR	$B_{min}$ [ $\mu\text{T}$ ]	$\Phi_{min}$ [ $\frac{h}{2e}$ ]	$m_{min}$ [ $\mu_B$ ]
InAs3.2	4	4.2	5.02	0.05	100.4	80	0.15	$6.1 \cdot 10^5$
		293	0.231	0.013	17.8			
InAs4	16	4.2	0.758	0.018	42.1	29	0.22	$1.8 \cdot 10^6$
		293	0.051	0.007	7.3			

**Tab. 2.1:** Signal height, noise and signal to noise ratio at room temperature and 4.2 K for samples InAs3.2 and InAs4. For  $T = 4.2 \text{ K}$  the minimal detectable field as well as the lowest flux and magnetic moment is calculated

compared to the smaller Hall bar. Thus the minimal detectable average field was also lower at a value of  $29 \mu T$  which compares well to similar experiments [Hoc03]. However, for the detection of nanomagnets the field flux and magnetic moment resolution are the more important figures of merit. And here the positions are reversed in favor of the smaller Hall bar which exhibits a field flux sensitivity of  $0.15 \Phi_0$  compared to  $0.22 \Phi_0$  where the flux quantum  $\Phi_0 = \frac{h}{2e}$ . Sample InAs3.2 offers the better magnetic moment resolution of  $6.1 \cdot 10^5 \mu_B$  compared to  $1.8 \cdot 10^6 \mu_B$  for the larger sample InAs4.

In conclusion, the dependency of the coercive field on the width of a rectangular slab suits theoretical prediction as well as the inverse proportionality of  $A_{HC}$  on the Hall signal (as long as the magnet's end is fully situated inside this area). Moreover, the linear dependency of the width on the signal strength has been proven. The achieved sensitivities are close to the best magnetic moment detection ( $10^4 \mu_B$ ) reported so far [TKGL<sup>+</sup>00], where the hysteresis of a single cubic iron nanoparticle (edge length = 30 nm) has been detected.

Subsequently, the sensors were miniaturized to even smaller dimensions. Unfortunately, the defect density of the available substrates was not low enough and further samples exhibited non-ohmic resistance because defects were situated in the current channel of the sample.

Since the best known 2DEG GaAs/(Al,Ga)As has already been extensively used for micro-Hall magnetometry before, the extraordinary HgTe 2DEG was chosen as new candidate. In the next chapter the suitability of the HgTe 2DEG for MHM will be investigated.

#### 2.2.7.4 Measurements on HgTe

With the experience obtained in the previous measurements sub- $\mu m$  Hall-Bars based on HgTe-2DEG were fabricated. The increased requirements on accuracy in the fabrication process for these devices could be fulfilled without problems. An example for the most critical step - the proper alignment of the magnet in the middle of the Hall cross - is shown in fig. 2.24a. The crossing of the white lines indicates the middle of the Hall cross and the accuracy of the alignment can be estimated to be in the order of a few 10 nm.

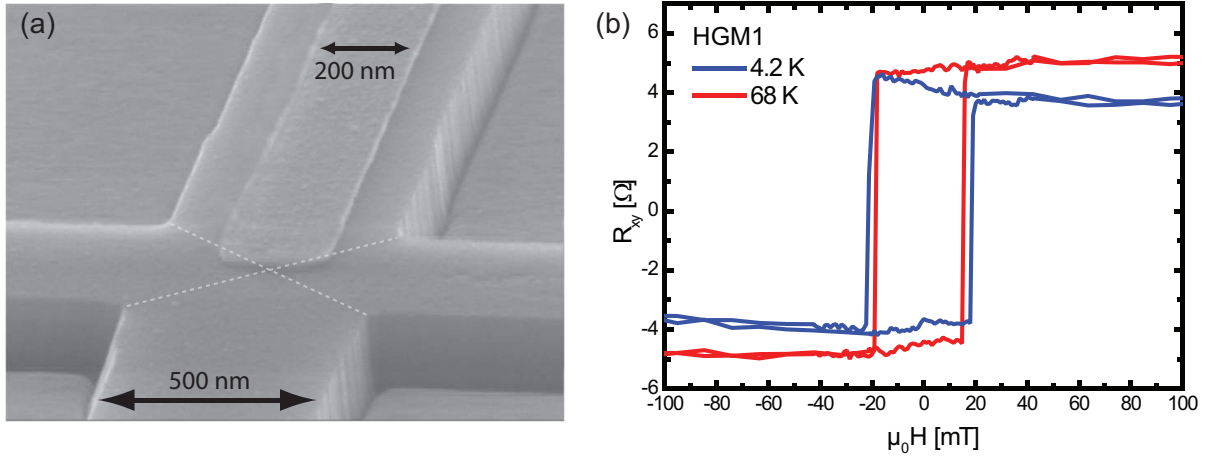


**Fig. 2.24:** (a) Micro-Hall sensor fabricated on HgTe 2DEG with Permalloy magnet on top, (b) hysteresis measurements of sample HGM1 with a current of 1  $\mu\text{A}$  for 4.2 K and 68 K, (c) signal height.

Moreover, it is visible that the edges of the mesa are smooth and the corners sharp due to highly anisotropic dry etching, thus suppressing unwanted ballistic effects.

Now the measurements on sample HGM1 shall be discussed. HGM1 is a micro-Hall sensor with a sensor area of  $300 \cdot 300 \text{ nm}^2$ . The applied Py magnet has a cross-section of  $100 \text{ nm} \cdot 30 \text{ nm}$  and a length of  $5 \mu\text{m}$ .

The magnetic field sweep measurements on this device are shown in fig. 2.24b and exhibit on the first sight a very clear signal.

It is remarkable, however, that the signal strength for 68 K is higher than for 4.2 K. Intuitively, this could be explained by a higher carrier concentration/lower mobility at lower temperatures or a lower saturation magnetization at lower fields. Both hypotheses are uncommon for both modulation-doped 2DEGs and ferromagnets. Furthermore the curve for 4.2 K could not be adjusted by a linear fit to correct the misalignment of the parallel field. Therefore the signal strengths and noise of a temperature range between 4.2 K and 200 K have been analyzed. As depicted in fig. 2.25a the signal strength first increases with higher temperatures and stays constant from 68 K on. The noise (indicated by error bars) reaches its minimum for this temperature. This is expressed in fig. 2.25b where the maximum of the SNR has a value of 108 for  $T = 68 \text{ K}$ .

The explanation for this behavior is uncommonly high universal conductance fluctua-

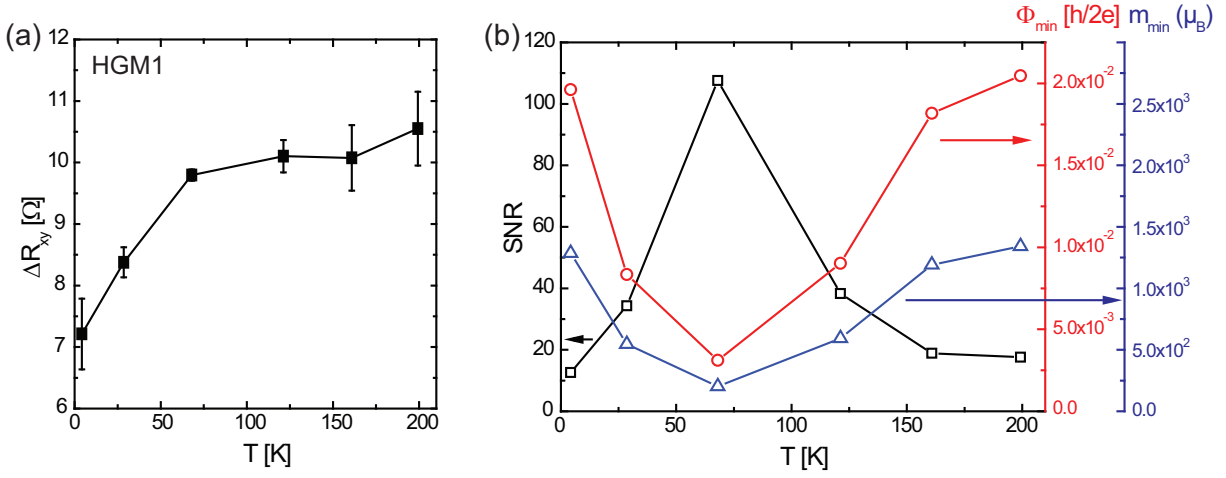


**Fig. 2.25:** Plots of (a) the signal height  $\Delta R_{xy}$  with error bars corresponding to the standard deviation and (b) the SN-ratio (black squares),  $\Phi_{min}$  (red circles) and  $m_{min}$  (blue triangles) depending on the temperature.

tions (UCF). These are fluctuations in the resistivity which depend strongly on the phase coherence length and are typically negligible for temperatures higher than 4.2 K and the used currents of about  $1 \mu A$ . However, measurements presented later in this thesis confirm the presence of UCF in HgTe up to 45 K. Phenomenologically, the electrons behave as waves and the transmission depends on the impurity configuration that can be altered e.g. by a magnetic field. That means that the stray field of the magnet sets two different configurations and the retrieved signal is a sum of the stray field and UCF signal. This falsifies  $R_{xy}$  and can lead to either higher or lower signal strengths. Here the achieved impurity configurations lead to a lower signal. Moreover the UCF increase the noise in the measurement.

At about 60 K the UCF vanish and the noise is the lowest. For higher temperatures the noise starts to rise again due to thermal noise.  $B_{min}$  for this temperature was found to be about 70 μT. This is the same value as for the  $(2 \cdot 2) \mu m^2$  InAs-based sensors. It is therefore not surprising that the HgTe Hall bar with only  $1/44 A_{HC}$  of the InAs-2DEG offers better resolution for localized fields. In fig 2.25b the field flux resolution for different temperatures is depicted by red circles.

The highest flux sensitivity for this HgTe-based device equals  $\Phi_{min} = \frac{\Phi_0}{322}$  and the



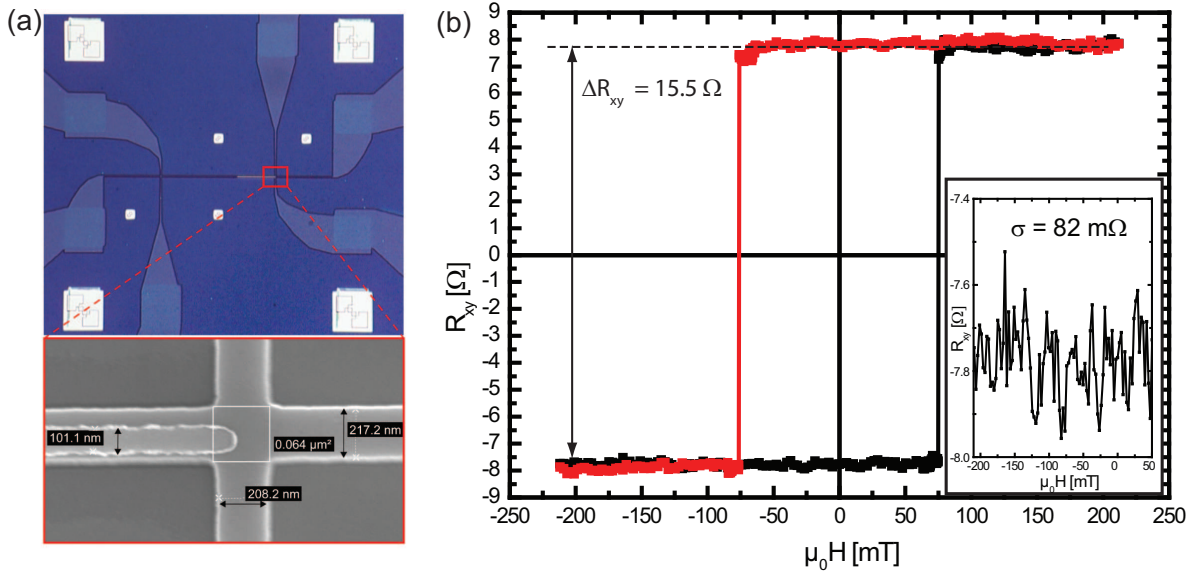


**Fig. 2.26:** (a) Micrographs of the smallest sensor HGM2 with  $A_{HC} = 0.045 \mu m^2$ ; (b) hysteresis measurement at a high current of  $8.4 \mu A$ .

highest magnetic moment resolution is  $2 \cdot 10^2 \mu_B$  (blue triangles in fig. 2.25). This ultra sensitive sensor's resolution is therefore better than state-of-the-art GaAs/AlGaAs 2DEGs sensors [GDL<sup>+</sup>97, LXvM<sup>+</sup>02], whose sensitivity has been calculated to be  $10^3 \mu_B$  or higher. The magnetic stray field of the Py magnet is found to be very constant over the temperature range from 60 K to 200 K as expected from this high  $T_C$  material. Furthermore the coercive field decreases slightly with temperature. This is because the thermal energy supports the nucleation process of a domain wall. Moreover it can be concluded that there is no parallel conductivity and the carrier concentration stays stable in the investigated temperature range.

The last sample described in this section was aiming for the highest possible sensitivity for nanoparticles. These are of particular interest since systematic nanowire growth in ordered arrays is within reach and a candidate for future storage devices. The sample HGM2 exhibits  $A_{HC}$  of  $(217 \cdot 208) nm^2 \approx 0.045 \mu m^2$ . Additionally, the top spacer layer of the 2DEG was omitted during growth, enabling closer contact to the 2DEG (distance = 25 nm). The applied magnet has a cross section of  $(100 \cdot 20) nm^2$ , easily comparable to typical synthesized nanowire dimensions (see fig. 2.26a).

The UCFs have been suppressed by using high currents in order to heat up the electron channel and smear out the quantum interference effects. The optimum current was found by increasing the applied voltage step by step and monitoring the Hall signal. First, the noise decreased significantly with higher voltages up to the point at about  $10 \mu A$  where the noise started increasing again, probably due to thermal heating. The following measurement was carried out at an applied voltage of 1.1 V which resulted in a current of  $8.4 \mu A$  (the sample resistance was about  $130 k\Omega$ ).

The corresponding Hall magnetometry measurement shows a brilliant signal with a height of  $15.5 \Omega$  while the noise is very low at  $82 m\Omega$  (see fig 2.26b). The SNR therefore equals 189. With the measured carrier concentration of  $7.2 \cdot 10^{11} cm^{-2}$   $B_{min}$  equals  $95 \mu T$ , and the corresponding flux sensitivity in units of magnetic flux quanta equals  $\frac{\Phi_0}{485}$ . The magnetic moment resolution (after (2.28)) has also been optimized down to  $92 \mu_B$  - a value unmatched so far for micro-Hall magnetometry. Yet this is still too far away from the detection of single spins as proposed in [JL05]. However, theoretically, a further decrease of  $A_{HC}$  by a factor of 92 could enable single spin detection. The corresponding edge length equals 22 nm - a dimension not far from reality.

With these results we can estimate the suitability to measure nanomagnets. For a nanomagnet with the same cross-section (edge length  $\approx 45 nm$ ), the particle could still be detected down to a saturation magnetization of  $1/189 M_{S,Py} = 800 kA/mT$ . In order to classify this value a representative for weak ferromagnets shall be considered. The diluted magnetic semiconductor GaMnAs exhibits at 4.2 K a saturation magnetization  $M_{S,GaMnAs} \approx 38 kA/m$  [GDJ<sup>+</sup>07]. The response of a similar shaped nanowire made of GaMnAs would therefore be 9 times larger than our sensitivity limit and easily observable. From another perspective, this sensor is capable of detecting the magnetization switching of a Py-slab that has a square cross-section with an edge length of 3.3 nm.

It is noteworthy that this was the sample fabricated with an additional gate to control the carrier density. The experiments with varied gate voltage did not show a significant increase in the SNR either for higher or lower carrier concentrations. Apparently, the higher Hall constant is directly canceled out by the reduced current as predicted by

(2.66).

Concluding this chapter, we were able to fabricate micro-Hall magnetometers with ultra-high sensitivity and the capability to investigate nanoscale magnets. The next chapter will deal with the second candidate for sensors on the micro-scale, the Micro-SQUID.

## 2.3 Micro-SQUID Sensors

In 1911, Kammerling Onnes discovered the effect of superconductivity (SC) [Onn11]. He observed a vanishing electrical resistance of mercury when the temperature dropped below a critical temperature  $T_C$  of 4.19 K. The theory behind superconductivity remained unclear until London made his empirical equations that could explain the effect under certain assumptions. The deep understanding of superconductivity was then obtained by Bardeen, Cooper and Schrieffer and their famous BCS-theory. SC is a remarkable effect and has drawn a lot of attention in science (up to now five Nobel Prizes dealt with superconductivity). Unfortunately - the ultimate goal - superconductivity at room temperature remained unachievable so far, even though the limit of the nitrogen boiling point was surpassed by a critical temperature of 93 K in 1987 [WAT<sup>+</sup>87]. Therefore the obvious use for a superconductor - the dissipation free transport of electric current at room temperature - is still out of sight. Nevertheless the principle of superconductivity is used in many specialized applications, e.g. in superconducting magnets (high magnetic fields) or for transport due to levitation (e.g. Supratrans [SdHV<sup>+</sup>05]). In addition, a remarkable application is the use as a magnetometer in superconducting quantum interference devices (SQUIDs). These sensors facilitate ultra-high resolution measurements of magnetic fields and are, since their first realization in 1964 [JLSM64], nowadays widely available as commercial devices. While their magnetic field resolution of homogeneous fields is unreached (down to  $5 \cdot 10^{-18}T$  [RM02]) - the measurement of strongly localized fields is not its specialty. In 1989 Benoit had the idea of miniaturizing the superconducting loop in order to be able to measure magnetic fields of upcoming nanostructures [CEKP<sup>+</sup>91]. He used electron beam lithography to structure a SQUID with a diameter of only 1  $\mu\text{m}$  - this device was then called micro-SQUID. In the following years, Wernsdorfer did extensive studies on micro-SQUIDs with impressive results [WHM<sup>+</sup>95, WHB<sup>+</sup>95, Wer09].

This chapter of the thesis deals with the fabrication and measurement of niobium-based micro-SQUIDs. The theory of superconductivity and standard SQUIDs will not be discussed since it would lead out of the scope of this work.

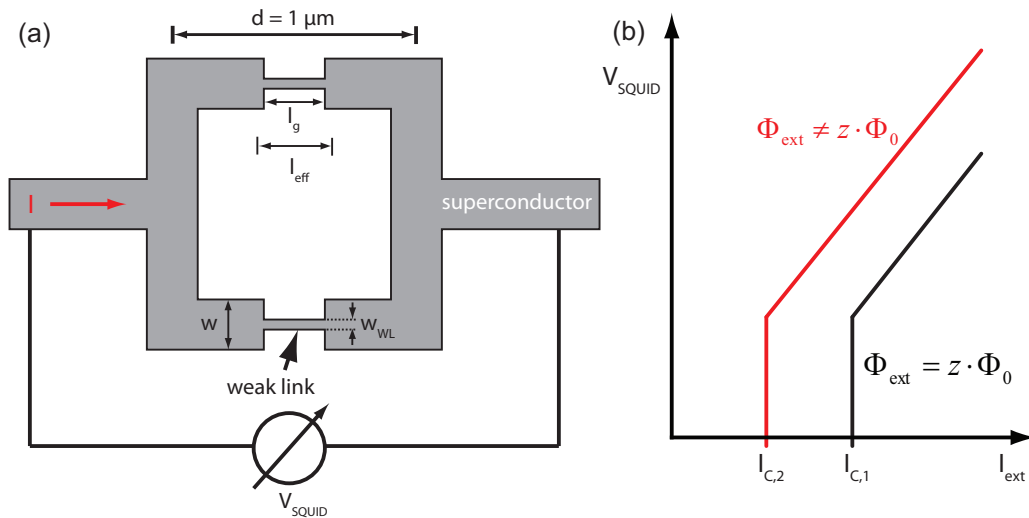


**Fig. 2.27:** (a) Sketch of a symmetrical micro-SQUID with two weak links (b) Voltage drop over the micro-SQUID depending on external current.

### 2.3.1 Basics of Micro-SQUID Operation

In this section the standard design and geometry of a typical micro-SQUID will be introduced. Furthermore, the mode of operation will be described. In the end the quantization condition for SQUID operation will be derived.

#### 2.3.1.1 Micro-SQUID Design

A closed superconducting path is necessary for the SQUID operation. The geometry itself does not play an important role. Square-like sensor areas are commonly used due to fabrication issues. The design of such an exemplary micro-SQUID is depicted in fig. 2.27a. The axis length  $d$  is here  $1 \mu\text{m}$ , and is defined by the centers of outer and inner leg. Moreover, the ring has two contacts that allow for application of external voltages. Furthermore the width  $w$  of the superconductor equals  $200 \text{ nm}$  and is constricted in two parts of the micro-SQUID - the so-called weak links - to a width  $w_{WL}$  of a few ten nanometers. Therefore, for an applied external voltage, the corresponding current  $I$  leads to a constant current density outside and an increased current density inside the weak links. The length of the constriction which the current experiences equals the effective length  $l_{eff}$ . It differs slightly from the geometrically defined length  $l_g$ .

With increasing currents, the superconductivity will first break down in the weak link and the following heat-up will cause an avalanche due to Joule's warmth. Subsequently, the whole device will become normal conducting. Therefore the figure of merit of a micro-SQUID is the measurement of the critical current  $I_c$  which depends on the flux penetrating the sensor area (see  $I_{c,1}, I_{c,2}$  in fig. 2.27b for two different fluxes). The observed critical current is a periodic function of the penetrating magnetic field. The reason for this behavior is based on the quantization criterion which is the subject of the next section.

### 2.3.1.2 Quantization Criterion

As the BCS-theory describes, the transport in a superconductor is based on the attractive force between two electrons mediated by the vibrating crystal lattice. Therefore the current is carried by pairs of electrons - the so-called Cooper pairs. They embrace a macroscopic state over the whole superconductor and can be described by a quantum mechanical wave function [Kit05]:

$$\Psi = \sqrt{n}e^{i\Phi} \quad \text{and} \quad |\Psi|^2 = n \quad (2.71)$$

$\Psi(\mathbf{r})$  is the probability amplitude and  $\Phi$  the phase. We assume the local density of the Cooper pairs  $n$  is constant over the micro-SQUID; a reasonable assumption since Cooper pairs carry the charge  $q = -2e$ , and the electric fields arising from inhomogeneous distribution would be instantly equalized. Under this assumption, the current density carried by the Cooper pairs in presence of a magnetic field can be derived. Using the impulse operator, the velocity of the Cooper pair in presence of a magnetic field is given by

$$\mathbf{v} = \frac{1}{m} (-i\hbar\nabla - q\mathbf{A}) \quad (2.72)$$

with the vector potential  $\mathbf{A}$ . Applied to the wavefunction, it follows for the particle flux:

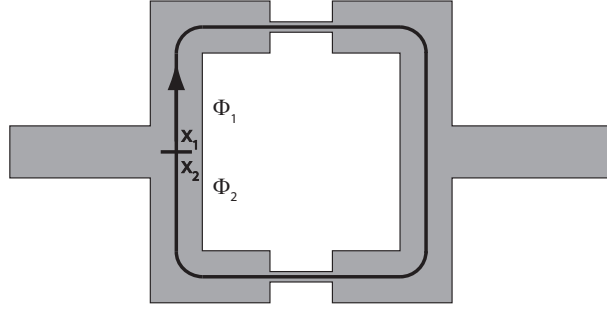


**Fig. 2.28:** Integration path around the superconducting loop.

$$\Psi^* \mathbf{v} \Psi = \frac{n}{m} (\hbar \nabla \Phi - q \mathbf{A}) \quad (2.73)$$

with  $\mathbf{j} = q \Psi^* \mathbf{v} \Psi$  and  $q = -2e$ , the current density carried by Cooper pairs equals

$$\mathbf{j}_s = \frac{-2ne\hbar}{m_e} \nabla \Phi - \frac{4ne^2}{m_e} \mathbf{A} \quad (2.74)$$

Rearranging (2.74) leads to the expression:

$$\nabla \Phi = -\frac{m_e}{2ne\hbar} \mathbf{j}_s - \frac{2e}{\hbar} \mathbf{A} \quad (2.75)$$

Now the special geometry of a closed superconducting loop is taken into account. Integrating equation (2.75) over the closed loop, beginning at  $x_1$  and ending in  $x_2 = x_1$  as depicted in fig. 2.28, results in:

$$\Phi_2(x_1) - \Phi_1(x_1) = -\frac{m_e}{2ne\hbar} \oint \mathbf{j}_s - \frac{2e}{\hbar} \oint \mathbf{A} \quad (2.76)$$

With assumption of constant Cooper pair density,  $\Psi^* \Psi$  is defined for the whole superconductor (including  $x_1$ ). However, the wave function  $\Psi$  keeps one degree of freedom: the phase  $\Phi$ , which is merely determined by the factor:

$$\Psi = \sqrt{n} e^{i(z \times 2\pi + \Phi)} \quad (2.77)$$

where  $z$  is an integer number. The phase of the wave function is therefore determined to differences of  $z \times 2\pi$ . For two different phases  $\Phi_1(x_1)$  and  $\Phi_2(x_1)$  the relation  $\Phi_2(x_1) - \Phi_1(x_1) = z \times 2\pi$  holds. Substituting Maxwell's equation  $rot\mathbf{A} = \mathbf{B}$  in (2.76) and using Stokes' theorem, which relates the line integral of a vector over a closed loop to the integral over the comprised surface of the curl of the vector, one obtains:

$$z \times 2\pi = \frac{m_e}{2ne\hbar} \oint \mathbf{j}_s + \frac{2e}{\hbar} \int_{A_{SQUID}} \mathbf{B}dA \quad (2.78)$$

$$= \frac{m_e}{2ne\hbar} \oint \mathbf{j}_s + \frac{2e}{\hbar} \Phi_{loop} \quad (2.79)$$

where  $\Phi_{loop}$  is the magnetic flux through the integrated area as depicted in fig 2.28. Introducing the flux quantum  $\Phi_0 = \frac{\hbar}{2e}$  leads to the equation:

$$z \times \Phi_0 = \frac{m_e}{4ne^2} \oint \mathbf{j}_s + \Phi_{loop} \quad (2.80)$$

Equation (2.80) can be understood empirically: for a given external field  $\mathbf{B}$  it follows that the current density  $\mathbf{j}_s$  must change by full integer numbers of the flux quantum in order to maintain the macroscopic wave function. Another commonly used interpretation is that the flux through a superconducting loop must fulfill the quantization in  $\Phi_0$ . That is why this relation is also called *quantization criterion* (QC). This quantum is not as minuscule as one might think. For the described SQUID dimensions of  $1\mu m \times 1\mu m$  one quantum equals a magnetic field flux of about  $2mT$  - a reasonable magnetic field, more than 40 times stronger than the magnetic field of the earth. Therefore external fluxes  $\Phi_{ext}$ , created by applied external fields, can take any values  $z \times \Phi_0 < \Phi_{ext} < (z + 1)\Phi_0$ . This stands in direct conflict with the quantization criterion. The only solution for this dilemma is when the loop counteracts with a circular current  $I_{circle}$ . This current leads, corresponding to Ampère's stationary circuital law  $\mu_0\mathbf{j}_{circle} = rot\mathbf{B}$ , to a magnetic field that diminishes or strengthens the external flux in order to meet the QC.

The term  $\frac{m_e}{4ne^2} \oint \mathbf{j}_s$  describes all superconducting currents arising in the loop. These are



- screening currents  $j_{screen}$  that come into existence because a superconductor is a perfect diamagnet and the magnetic field must be pressed outside the superconductor. Due to the symmetry of these currents it follows that:  $\oint_{loop} j_{screen} = 0$
- external currents  $j_{external}$  applied via the contacts. These currents are divided symmetrically over the loop and therefore  $\oint_{loop} j_{external} = 0$  as well (see fig. 2.29).
- circular currents  $j_{circle}$ . These are currents flowing clockwise or counterclockwise in the loop and therefore:  $\oint_{loop} j_{circle} \neq 0$ . This is obviously the current that ensures quantized fluxes through the superconducting loop since it is the only not vanishing contribution.

The flux through the loop consists of the externally applied and internal flux:

$$\Phi_{loop} = \Phi_{ext} + \Phi_{circle} = \Phi_{ext} + L_g \cdot I_{circle} \quad (2.81)$$

$L_g$  is a geometrical factor and depends on the shape of the loop. Therefore (2.80) equals:

$$z \cdot \Phi_0 = \frac{m_e}{4ne^2} \oint \mathbf{j}_{circle} + \Phi_{loop} \quad (2.82)$$

$$= \frac{m_e}{4ne^2} \left( \frac{4d - 2l_{eff}}{\sigma_{loop}} + \frac{2l_{eff}}{\sigma_{WL}} \right) \cdot I_{circle} + (\Phi_{ext} + L_g \cdot I_{circle}) \quad (2.83)$$

$$= \left( L_g + \frac{m_e}{4ne^2} \left( \frac{4d - 2l_{eff}}{\sigma_{loop}} + \frac{2l_{eff}}{\sigma_{WL}} \right) \right) \cdot I_{circle} + \Phi_{ext} \quad (2.84)$$

Here a homogeneous distribution of the current in the cross-section of the loop  $\sigma_{loop}$  and the weak links  $\sigma_{WL}$  is assumed. Equation (2.84) implies that the flux comprised by a current in a loop consists of two contributions: the geometric factor shown by  $L_g$  and the kinetic factor of the Cooper pairs.

Equation (2.84) can then be written as:

$$z \cdot \Phi_0 = \Phi_{ext} + (L_g + L_{kin}) \cdot I_{circle} \quad (2.85)$$

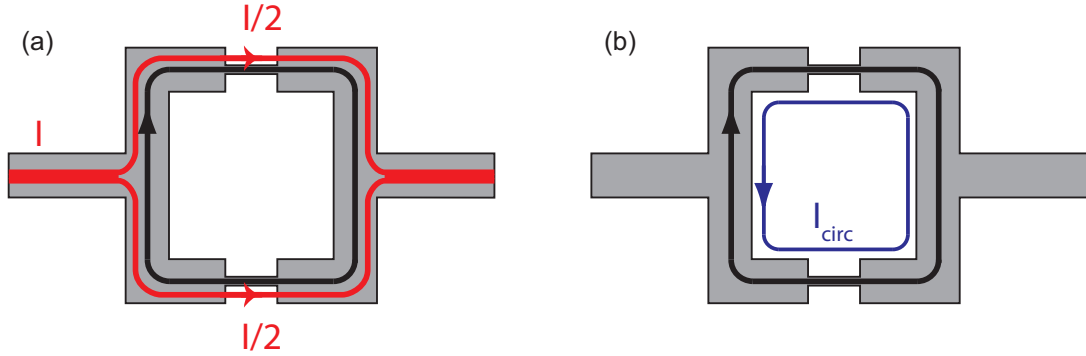


**Fig. 2.29:** (a) Current dispersion in the micro-SQUID (b) Circular current running counterclockwise to the integration path.

The circle current needs to be as small as possible due to energy considerations and will take values in the range  $(L_g + L_{kin})I_{circle} \in [-\frac{\Phi_0}{2}; \frac{\Phi_0}{2}]$ . This range enables the device always to suffice the quantization criterion. However, it must be noted that in some experiments higher circular currents were observed leading to an ambiguity of the critical current.

As depicted in figure 2.29a the external current  $I_{ext}$  is divided symmetrically to the branches of the micro-SQUID. In addition, a circular current is present in order to maintain the QC. Therefore the total current through one weak link is always twice the circular current of the other one. The current through the stressed weak link is given by:

$$I_{wl, stress} = \frac{I_{ext}}{2} + I_{circle} \quad (2.86)$$

The behavior for varied  $I_{ext}$  will now be considered (compare fig. 2.27b). First the case without circular current (or  $\Phi = z \times \Phi_0$ ) is examined. With increasing  $I_{ext}$  the voltage drop  $V_{SQUID}$  over the device stays zero until  $I_{c,1}$  is reached, as the black curve implies. In presence of a circular current one weak link is stressed and therefore leads to an earlier breakdown by means of  $I_{ext}$  as shown by the red curve ( $I_{c,2}$ ). The critical current of the stressed weak link can be written as:

$$I_{c,wl} = \frac{I_{c,ext}}{2} + I_{circle} \quad (2.87)$$

$$I_{c,ext} = 2(I_{c,wl} - I_{circle}) \quad (2.88)$$

$I_{c,wl}$ , the critical current for the weak links, is nearly constant for small magnetic fields, whereas  $I_{circle}$  strongly depends on external fluxes. The behavior of  $I_{c,ext}$  over the magnetic flux  $\Phi$  in units of  $\Phi_0$  is sketched in figure 2.30 and will now be discussed in detail. First, for zero external flux, the critical current reaches its highest value and equals  $2I_{c,wl}$ . This value is obtained for fluxes  $z \cdot \Phi_0$ . On the other hand, the minimum of  $I_{c,ext}$  is obtained for maximum  $I_{circle}$  and therefore for a flux of  $(z + 0.5) \cdot \Phi_0$ . At these positions,  $I_{circle}$  changes its sign in order to minimize the energy of the system. Accordingly, the critical current increases again.

Due to equations (2.85) and (2.88)  $\Delta I_{c,ext} = 2 \cdot I_{circle,max} = \frac{\Phi_0}{(L_g + L_{kin})}$ . The curve between has a linear shape with a slope of  $\pm 2(L_g + L_{kin})$ . The repeated change of rotational direction of the circular current in an external flux causes periodic behavior of the critical current of this device. Monitoring the critical current via the measured voltage drop thus allows for external fluxes to be detected.

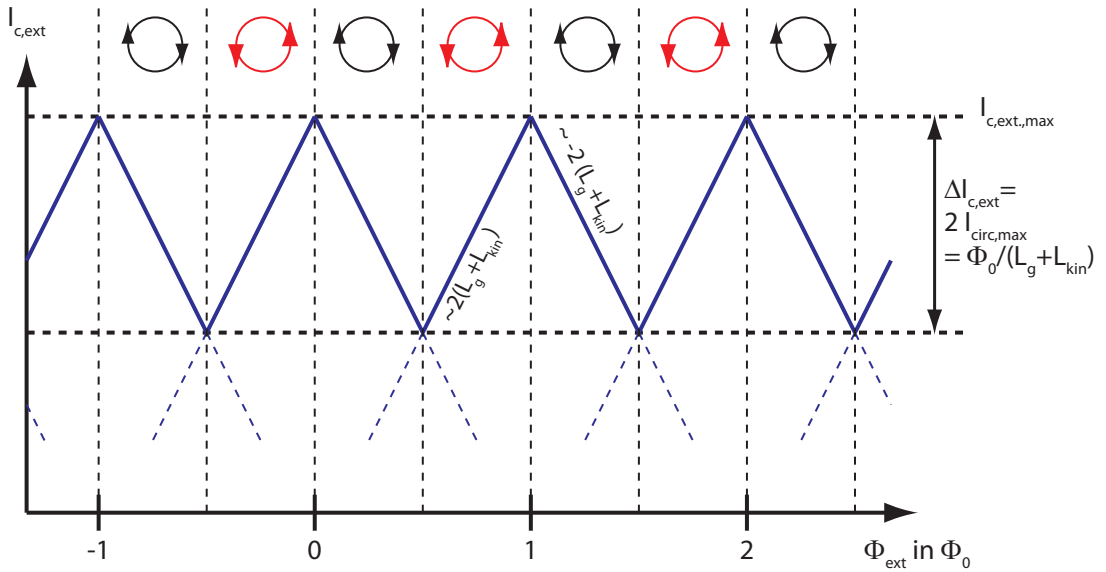


**Fig. 2.30:** Critical current of a micro-SQUID depending on the externally applied current.

Yet it is important to understand that this characteristic curve does not allow for absolute measurements of the magnetic field. The reason is the plurivalence of the y-axis.

Thinking of the sensitivity of the magnetic sensor, the figure of merit is the modulation depth (MD) as calculated by the amplitude of the curve normalized with the maximum critical current:

$$MD = \frac{\Delta I_{c,ext}}{I_{c,ext,max}} \quad (2.89)$$

using the expressions of  $\Delta I_{c,ext}$ , alongside the relation  $I_c = \mathbf{j}_c A$ , where  $\mathbf{j}_c$  only depends on the superconducting material. The evaluation of MD leads to:

$$MD = \frac{\Phi_0}{2I_{wl,c}(L_g + L_{kin})} = \frac{\Phi_0}{2(L_g + L_{kin})j_{c,wl}\sigma_{wl}} \quad (2.90)$$

The geometric inductance for a quadratic loop is given by  $L_g = 1.25 \mu_0 d$  [CB06], while the kinetic inductance is given by equations 2.84 and 2.85. The modulation depth then results in:

$$MD = \frac{\Phi_0}{\left(1.25 \mu_0 d + \frac{m_e}{4n e^2} \left(\frac{4d - 2l_{eff}}{\sigma_{loop}} + \frac{2l_{eff}}{\sigma_{wl}}\right)\right) 2j_{c,wl}\sigma_{wl}} \quad (2.91)$$

$$= \frac{\Phi_0}{j_c \left(2.5 \mu_0 d \sigma_{wl} + \frac{m_e}{2n e^2} \left(\frac{\sigma_{wl}}{\sigma_{loop}} (4d - 2l_{eff}) + 2l_{eff}\right)\right)} \quad (2.92)$$

Now the main factors for the modulation depth of the micro-SQUID are obvious. The cooper pair density is constant for a given superconductor at constant temperature. In order to increase MD, which should intuitively lead to a better sensitivity, the following factors can be tuned:

- decrease the side length  $d$  of the micro-SQUID
- decrease the effective length  $l_{eff}$  of the weak links
- decrease  $\sigma_{wl}$  and/or decrease the ratio  $\frac{\sigma_{wl}}{\sigma_{loop}}$

However, increasing the modulation depth does not necessarily increase the resolution of the micro-SQUID. The reduction of the side length  $d$ , for example, also leads to a higher oscillation period, thus a lower slope. For constant noise conditions the benefit of deeper MD can then be canceled in terms of magnetic field resolution. For localized fields, further miniaturization is favorable.

Moreover, the effective length of the weak link  $l_{eff}$  is not identical to the geometric length and cannot be decreased indefinitely [Lik79]. Phenomenologically this can be understood as if the current path is constricted even outside the weak links. This is because  $\mathbf{j}$  cannot change abruptly at the transition.

The decrease of  $\frac{\sigma_{wl}}{\sigma_{loop}}$  is technologically challenging because the superconductivity must persist in the weak link. Nevertheless, controlled oxidation of the superconductor in the weak link has been successfully used in order to increase the modulation depth that way [BFT<sup>+</sup>01].

Due to stable fabrication process and therefore higher yield, the most commonly used micro-SQUID for sensing applications nowadays exhibits a typical area of  $1 \mu m^2$  and a constant width of the superconducting layer.

### 2.3.2 Fabrication of Micro-SQUIDs

This section deals with the fabrication of micro-SQUIDs based on niobium. The process parameters for the fabrication of a superconducting ring are described in table A.5.

The substrate used were Si wafers with 200 nm thermal  $SiO_2$  on top. After standard cleaning of the substrate, the superconductor is deployed onto the wafer.

First, a direct fabrication technique was employed using positive EBL, ebeam evaporation of Nb and lift-off. But the production of a stable high quality film was not straightforward. It is important to know that Nb is a getter material and easily incorporates impurities. Therefore a fast evaporation process is favorable. On the other hand, the evaporation heated up the vacuum chamber because of niobium's high melting point of 2750 K. This caused an evaporation of previously condensed material at the walls of the vacuum chamber, decreasing the quality of the deposited Nb. In order to prevent the

latter, a multi step evaporation process with cool down phases was therefore used.

But there is another impact on the purity of the superconducting film: the resist used for direct patterning was found to be another serious source for impurities. The low chamber pressure, supported by high heat radiation, leads to an outgassing of the resist - especially of those surfaces that have not been exposed to atmosphere during baking. Unfortunately, these are the trenches that provide the lift-off structure. Subsequently this hypothesis was confirmed by measurements, which exhibited a strong width dependence of superconducting strips. In a series samples the smallest superconducting strip was achieved for a width of 100 nm, whereas the critical current increased for wider strips. This behavior is best explained best by local impurities originating from the sample and not by general impurities (e.g. of the source). Thus the resist presumably is the reason for poor superconducting properties in thin structures. Summarizing, the best superconducting width of 100 nm is far too wide for the dimension of weak links. Therefore direct patterning methods are unsuited for Nb-based micro-SQUID fabrication.

The source material in the crucible improved in its quality over time (higher  $T_C$ ). An explanation is the preferred evaporation of impurities with lower sublimation temperature in the Nb-source. Hence, after refilling the crucible, the quality of the superconducting layer was decreased significantly. To circumvent this issue, an alternative deposition process with constant source quality was introduced.

The altered method of fabricating the micro-SQUID consisted of DC-sputtering a complete superconducting layer with subsequent etching. The development process on these films was performed by production of various superconducting layers, and exposing them to different temperatures in order to investigate stability and aging of the superconductor. The superconducting transition temperature was then determined in a commercially available SQUID-System from Quantum Design (for particular measurements, see [Bat08]).

The results were as follows:

- The faster the film was sputtered, the more stable the superconductivity was. The obvious reason is the getter behavior of niobium.
- The superconducting films lose quality due to their age and when they were exposed

to high temperatures (e.g. 200°C, when baking a resist). Applying a protective layer of Al prevented the thermal degradation while Ru could not.

Due to the fact that aluminum forms an insulating oxide and is etched by the standard optical developer, an additional protective layer needed to be used. Ru is an adequate choice because it is resistant to the developer, and its natural oxide is conductive thus alleviating good contacts.

The metal trilayer Nb/Al/Ru therefore became the basis for the fabrication of micro-SQUIDs. The further fabrication steps will now be discussed and are depicted in fig. 2.31a. After spincoating the PMMA bilayer the micro-SQUID structure is defined by EBL. The weak links were written by single pixel lines to ensure a high current density and a locally controlled breakdown of superconductivity. After development in isopropanol and stopping in deionized water, the Ti etch mask was evaporated and produced in the subsequent lift-off process. In order to remove all remnants of PMMA, the sample was cleaned in hot MIBK and rinsed in IPA. In the next step, the outer contacts were made by standard optical lithography. Subsequently evaporated metal trilayer titanium/gold/titanium is structured by lift-off and serves as an adhesive layer, contact layer and etch mask, respectively. The definition of the micro-SQUID is then done by physical Ar-sputtering. The successful definition of the mesa is checked by measuring the resistance of the remaining layer aiming for high resistance. The final step is to glue the sample with GI-Varnish into a chip carrier and bond the contacts. In a later experiment, a permalloy nanomagnet was deployed to the micro-SQUID. The magnet was applied by EBL with exact alignment, to lie on the leg of the micro-SQUID with one end pointing to the center of the loop. The deposition was carried out via sputtering and subsequent lift-off.

### 2.3.3 Measurement Setup

In contrast to standard SQUIDs, where the device is usually held in a constant resistance mode, another measurement method must be used in order to investigate micro-SQUIDs. This is because Joule heat leads to a breakdown of superconductivity in the complete microscopic ring and therefore a state of constant voltage drop cannot be obtained.

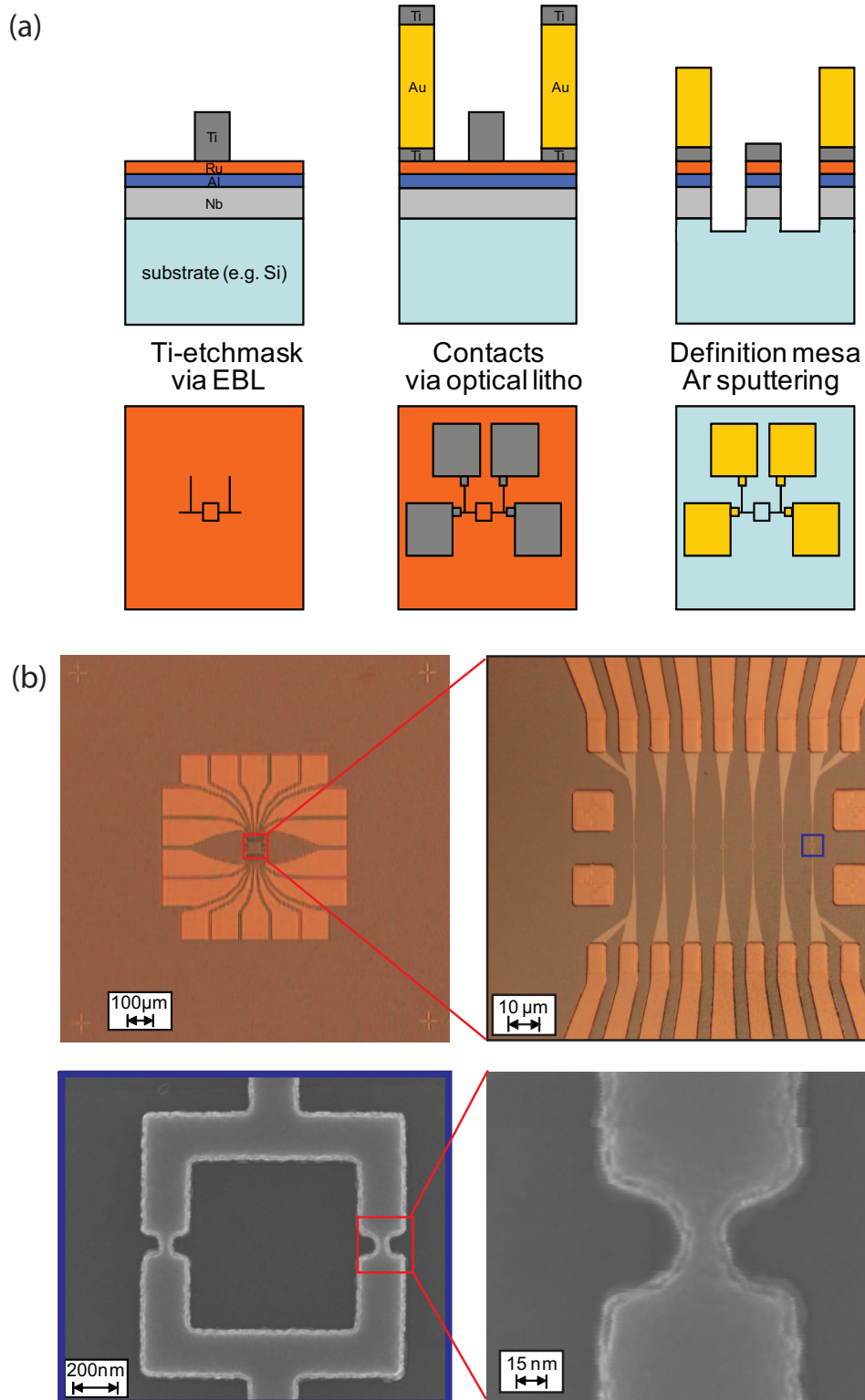


**Fig. 2.31:** (a) Process for fabrication of micro-SQUIDs (b) Micrographs after applied contacts and dry-etching in different magnifications, the red and blue boxes correspond to the zoomed-in micrographs.



The measured unit of a micro-SQUID is in fact the critical current. As mentioned before, the critical current  $I_{c,ext}$  is a function of the magnetic field due to the existence of the circular current.  $I_{c,ext}$  is sampled by taking voltage ( $V_{SQUID}$ ) vs. current ( $I_{ext}$ ) curves. An electronic circuit was developed in order to offer a good time resolution. The circuit consists of two PCBs (printed circuit board). PCB1 is supplying periodic voltage ramps, whereas PCB2 is used to read-out the micro-SQUID. The principle of the measurement setup is sketched in fig 2.32.

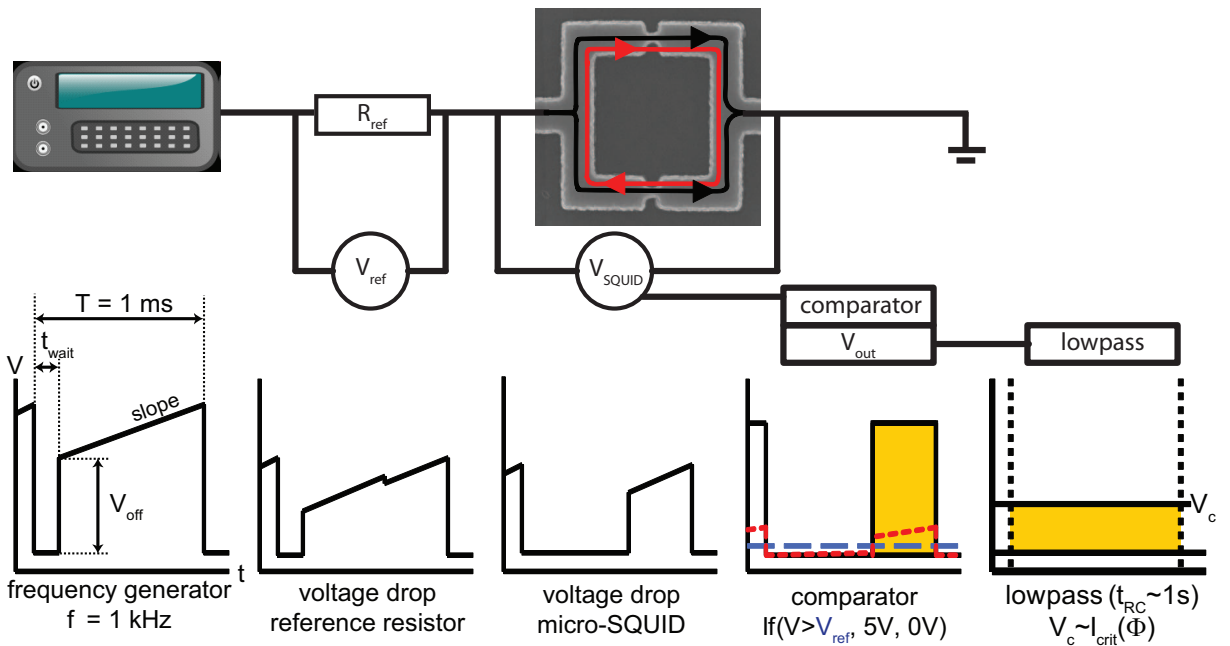


**Fig. 2.32:** Scheme of the used measurement setup; the sample itself is immersed in a bath cryostat in liquid Helium at 4.2 K. The measurement consists of a function generator providing definable voltage ramps with a frequency  $f$  which is applied to a reference resistor and the micro-SQUID in series. The corresponding voltages to the positions in the setup are sketched underneath. The yellow boxes indicate the same area translating a periodic signal into a DC voltage.

PCB1 is a function generator which offers periodic voltage ramps (sawtooth-like). In order to adjust these to the specific breakdown conditions of each micro-SQUID, the frequency  $f$ , the offset  $V_{off}$ , the slope and a waiting time  $t_{wait}$  (before the ramp starts) can be adjusted by trimmers. The frequency used during all the measurements was 1 kHz. The voltage between the ramps is set to 0 V in order to bring the micro-SQUID back to its superconducting state. After PCB1 there is a reference resistor of  $1\text{ k}\Omega$  in order

to limit the output current. The micro-SQUID is in series in the circuit and thereafter the lead is put to ground. Before starting sensitive measurements, the voltages over the reference resistor and the micro-SQUID were monitored by a 2-channel oscilloscope in order to optimize the ramps to the characteristics of each micro-SQUID.

After doing so, PCB2 is employed in the circuit parallel to the micro-SQUID while removing the oscilloscope. In PCB 2, an instrumentation amp measures the voltage drop over the micro-SQUID. Subsequently, a comparator compares  $V_{\text{SQUID}}$  (red) to an adjustable reference voltage  $V_{\text{ref}}$  (blue). It outputs 5 V if  $V_{\text{SQUID}} > V_{\text{ref}}$  and 0 V otherwise. The oscilloscope is used to adjust the reference voltage to a level well above the noise and below the voltage drop to normal conductance (preferably in the middle). A following low-pass filter with a time constant of 1 sec averages over the signal, supplying a DC-voltage that corresponds to the time of superconductivity, and therefore the critical current. Subsequently this  $V_c$  is measured by an Agilent 34420A nanovoltmeter. The read out is carried out by a computer which also controls the magnetic field by a self-written LabVIEW-program. The sample is immersed in a bath cryostat in liquid helium equipped with two superconducting coils (see setup in section 2.2.6).

### 2.3.4 Resolution of a Micro-SQUID

Using the previously described fabrication process, micro-SQUIDs were obtained with desired geometry of legs and weak links as shown in fig. 2.31b. When applying a perpendicular magnetic field, the critical current is predicted to be a periodic function (fig. 2.30). In this case the electron microscope provides a measured leg length of  $d = 1.002 \mu\text{m}$  equal to an area of the micro-SQUID  $\approx 1.004 \mu\text{m}^2$ . The expected periodicity is therefore  $\Delta B = \Phi_0/A_{\text{SQUID}} = 2.08 \text{ mT}$ .

The actual measurement of this device is shown in fig. 2.33. The experimental curve strikingly matches theory. With  $d = \sqrt{A_{\text{SQUID}}} = \sqrt{\Phi_0/T_{\text{SQUID}}}$  the periodicity predicts a leg length  $d$  of  $(0.994 \pm 0.023) \mu\text{m}^2$ . The difference between geometry and measurement lies well in the error bars and can be explained by a slightly tilted sample and imperfect magnetic field calibration. It must be noted that the error of the period in this measure-

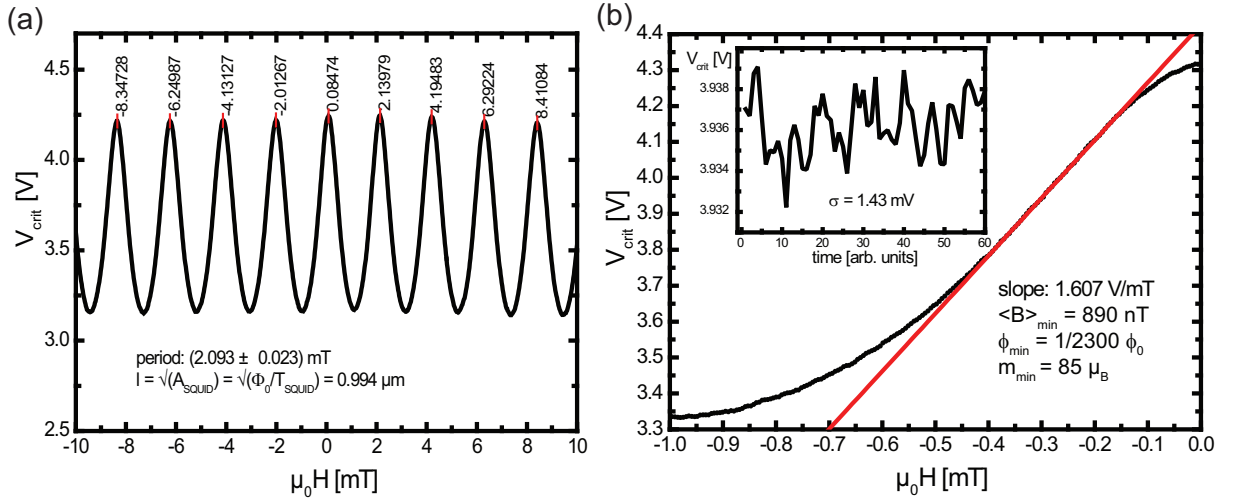


**Fig. 2.33:** (a) Micro-SQUID measurement with a periodicity of  $\approx 2.09$  mT (b) Fine magnetic field sweep for determination of maximum slope, inset: time dependent measurement at maximum slope.

ment is higher than shown later. This is due to "coarse" magnetic field steps of  $20 \mu\text{T}$  taken here.

The operating B-field range of the micro-SQUID is limited due to the breakdown of superconductivity when reaching the critical field  $B_C$  of the superconductor (the average  $B_C$  is in the order of several 10 mT). One can estimate the resolution of the micro-SQUID by the slope of the signal and the noise of the measurement. The noise is obtained by the standard deviation of  $V_c$  in a time dependent measurement close to the highest slope (see inset fig. 2.33) The noise found in this measurement is about 1.43 mV while the slope at the steepest part is determined to be 1.607 V/mT.

The ability to resolve magnetic field changes therefore calculates to  $8.9 \cdot 10^{-7}$  T. With (2.69) and (2.70) the minimum detectable flux change equals  $\Phi_0/2300$  while the magnetic moment resolution is  $85 \mu_B$ .

In conclusion, the resolution of this device is excellent and well-suited to detect the magnetic properties of nanoscale particles. In the next section the exemplary measurement of a ferromagnetic particle will be described.

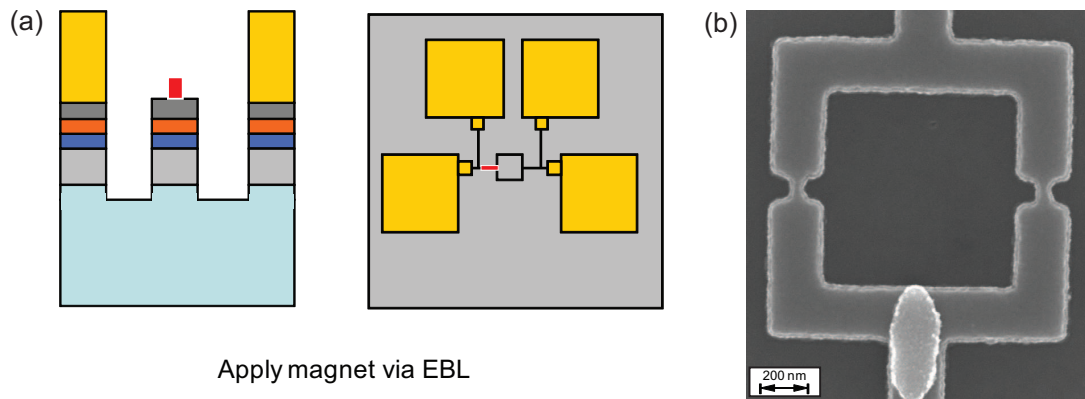


**Fig. 2.34:** (a) Additional process step (side and top view) for application of nanomagnet (b) Micrograph of micro-SQUID ( $1.0\ \mu\text{m}$  leg length) with deployed permalloy ellipsoid.

### 2.3.5 Investigation of a Nanomagnet

The feasibility of the achieved device to investigate the magnetic properties of nanoparticles shall now be enlightened.

A device was fabricated according to the developed process. Subsequently a Py ellipse was processed on top of the leg of the micro-SQUID pointing inside the loop. The major axis was 400 nm, the minor axis 200 nm and the thickness 30 nm. Since the lift-off is a challenge for sputtering, a low voltage electron beam lithography step of 2.5 keV was employed to obtain a strong undercut. The additional process step and a micrograph of the sample are shown in fig. 2.34.

Subsequently, the micro-SQUID was characterized in a perpendicular field and the sensitivity was found to be in the same order as the micro-SQUID discussed in the previous section. The sample was then inserted inside the in-plane sample stick. Thus the magnetic field was aligned parallel to the leg and the long axis of the nanomagnet.

Starting from negative magnetic fields, the up and down sweeps are shown in fig. 2.35a). Remarkably, the SQUID still shows an oscillatory behavior, even though the critical current should stay constant for in-plane magnetic fields ( $\Phi = 0$  perpendicular through the loop). Apparently, the misalignment between the sample plane and the magnetic field is not negligible, thus providing a small magnetic field perpendicular to the plane. The misalignment can be estimated by comparing the period of the oscillations

$T_{par} = 124 \text{ mT}$  vs  $T_{perp} = 2.09 \text{ mT}$  to an angle of  $0.98^\circ$ , which is a reasonable mismatch due to manual gluing. Following the further progression of the up sweep up to a magnetic field of about  $+0.3 \text{ mT}$  the curve deviates significantly from the periodic behavior. The critical current jumps to a different position and from there on an oscillatory curve with the same periodicity is recovered. When sweeping the magnetic field down again, the curve presents symmetrical behavior to the " $B = 0 \text{ T}$ "-axis confirming hysteretical behavior of the nanomagnet.

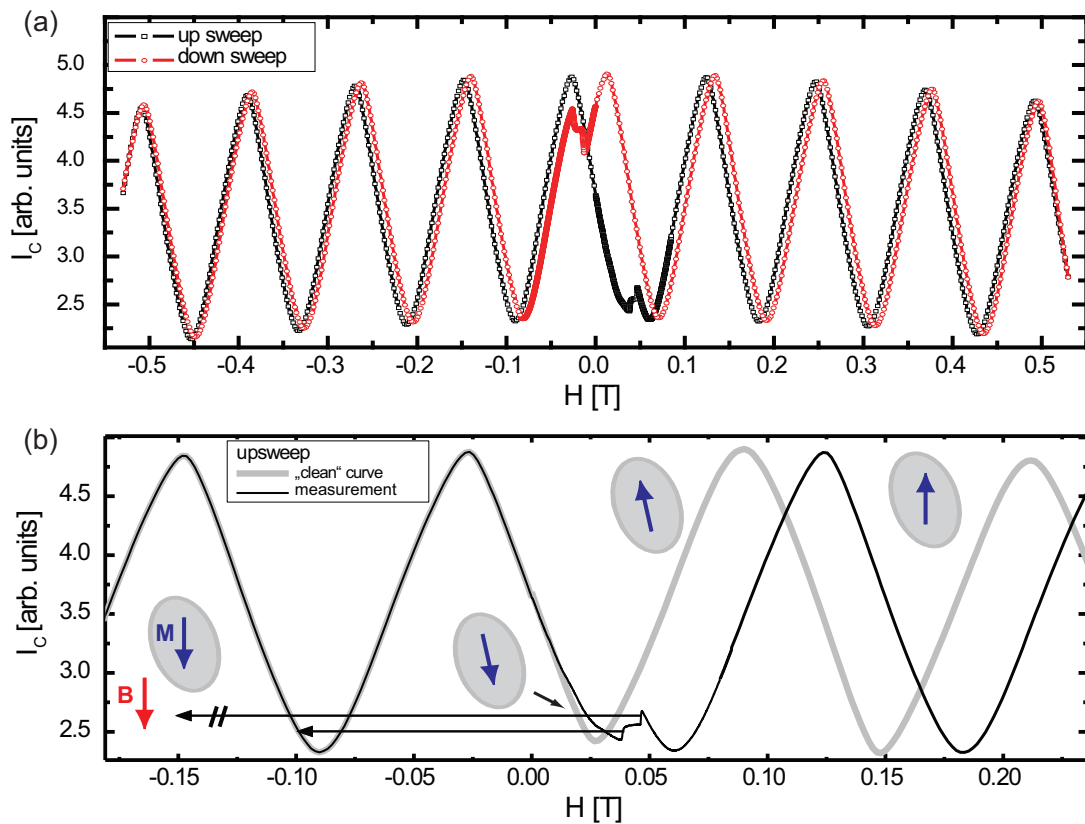


**Fig. 2.35:** (a) Hysteresis measurement in in-plane magnetic field, (b) Up sweep with artificial curve without magnet (light grey) by maintaining the periodicity of the signal; presumed magnetization orientations are sketched.

A closer look to the progression of the up sweep will now be taken (fig. 2.35b). For better understanding, the initial periodicity is artificially maintained in the "clean curve" indicated by the light grey curve. The measurement starts to deviate from the "standard" behavior at  $B \approx 0 \text{ T}$  indicating the misalignment between  $\mathbf{B}$  and the long

axis of the ellipse. For low fields, the magnetization tends to orient along the easy axis (long axis of ellipsoid). This takes place in a coherent rotation of all spins (single domain state). Subsequently, at about  $35 \text{ mT}$ , the switching of magnetization takes place. Then the magnetization seems to be pinned until the full switching is observed for  $B = 50 \text{ mT}$ . From this point, the field flux does not change any more due to the stray field of the nanomagnet. The critical current recovers the oscillation stemming from the external field.

It is noteworthy, that parallel fields up to 0.5 T did not interfere with the standard micro-SQUID mode of operation. In conclusion, the change in the stray field of an applied nanomagnet was observed confirming the suitability of this sensor for the magnetic characterization of nanoparticles.

## 2.4 Conclusion

The last two sections featured two very different magnetic sensors, based on the classical Hall effect and superconductivity. During this work, the fabrication and characterization of these sensors has been established at the chair of Experimentelle Physik III. The achieved sensitivity for both sensors is state-of-the-art for micro-SQUID sensors [Wer09] and better than state-of-the-art for MHM [GDL<sup>+</sup>97] compared to publications.

The need to compare the two magnetic sensors is obvious. Table 2.2 shows the results for the best sensors optimized for the detection of strongly localized fields.

Method	$B_{min}$ T	$\Phi_{min}$ $\Phi_0$	$m_{min}$ $\mu_B$
Micro-Hall-Magnetometry	$9.5 \cdot 10^{-5}$	$2.1 \cdot 10^{-3}$	92
Micro-SQUID	$8.9 \cdot 10^{-7}$	$4.4 \cdot 10^{-4}$	85

Tab. 2.2: The sensitivity of the two sensors for  $T = 4.2 \text{ K}$

There is no question, the micro-SQUID beats the micro-Hall magnetometry, both in terms of magnetic field and magnetic moment resolution. However, the sensitivity

differences are not that far apart. And MHM is superior in other ways. It boasts a wider usable temperature range, up to room temperature. Micro-SQUIDs are limited to the critical temperature of their superconductor. And even though high temperature superconductors are available, the characterization of technology-relevant properties of nanoparticles at room temperature is still currently out of reach. Another drawback is the limited magnetic field suitability due to breakdown of superconductivity. However, the obtained field range for parallel fields in this work ( $\geq \pm 0.5 T$ ) suffices most manipulation requirements. The out-of-plane magnetic fields, on the contrary, are limited to values of several  $10 mT$ . MHM is only disturbed by the occurrence of the quantum Hall effect. But even at high fields of some Tesla, there will still be a signal visible.

On the other hand, micro-SQUIDs do not underlie restrictions when it comes to substrates. The superconductor can be deposited on almost any material. Moreover, there is no need to take account of the conductivity of the material because there is no better conductor than a superconductor. Therefore micro-SQUIDs are well-suited for scanning sensors; they can even be built on top of a cantilever [HMK02].

Then again, the high-sensitive micro-Hall magnetometry depends on high mobility electrons. The sensors can also be built of standard metals but cannot come close to the sensitivity of the 2DEG-based (e.g.  $\Phi_{min} \approx 10^{-1} \Phi_0$  for  $(100 \cdot 100) nm^2$  Au sensor [CGDB<sup>+</sup>07]).

One last important difference is the propagation of the two sensor signals depending on the magnetic field. The linear dependence of MHM gives an explicit response and the measured signal is absolute. On the contrary, the periodicity of micro-SQUID curves inhibits absolute measurements. That is why the investigation of slowly varying fluxes is the specialty of micro-SQUIDs. Abrupt switching of single domain particles is harder to investigate but can be measured by the cold mode method [Wer09]. Here the magnetic field must lie parallel to the micro-SQUID plane.

For these measurements, the micro-SQUID setup needs to be improved. At first, the magnetic field should be manipulable in 3D in order to correct misalignment and for variable sample rotation. Furthermore, the electronics for the SQUID should instantly

set the applied voltage to zero when the breakdown of superconductivity occurs. This prevents the micro-SQUID from heating up and should lead to a better sensitivity in the measurements.

In the case of MHM the established measurement setup is close to the limit of the technique. An interesting application would be the measurement of single spins or spin accumulations. In the spin Hall effect, for example, spins are separated by a driven current due to the Rashba effect. The HgTe used 2DEG for MHM exhibits a giant Rashba splitting and the spin Hall effect has been observed in transport measurements [BRN<sup>+</sup>10]. The direct measurement of the moments of the spin could be obtained by a heterostructure offering two 2DEG layers and two driven currents.

This concludes the chapter of micromagnetic sensors. The next chapter will deal with transport properties on HgTe 2DEGs. Although used before for MHM, HgTe is more than a standard 2DEG and exhibits very uncommon transport properties.



# Chapter 3

## Dirac Fermions in HgTe Heterostructures

In the second part of this work we will investigate mesoscopic transport properties of HgTe quantum wells at low temperatures. During the last few years these have gained a lot of interest due to the discovery of the quantum spin Hall effect QSHE [KBMH08]. The very special band structure and the tunable energy gap give rise to particular effects.

The quantum well can be tuned in order to reach a zero energy gap and promises in ab initio calculations a very similar band structure to the famous graphene. In the first section of this chapter a brief overview of the band structure of HgTe/(Hg,Cd)Te will be given. The existence and experimental evidence of a zero-gap quantum well is the topic of the second section. In the last part the investigation of an observed conductance correction is dealt with. Experiments at low temperatures prove the latter is attributed to quantum interference effects and conclude this work.

### 3.1 Properties of (Hg,Cd)Te Quantum Wells

Both HgTe and CdTe bulk materials crystallize in the zinc-blende structure (like GaAs). This lattice resembles the diamond lattice, but with two different atoms per unit cell.

The band structures for the binary compounds CdTe, HgTe and the ternary material

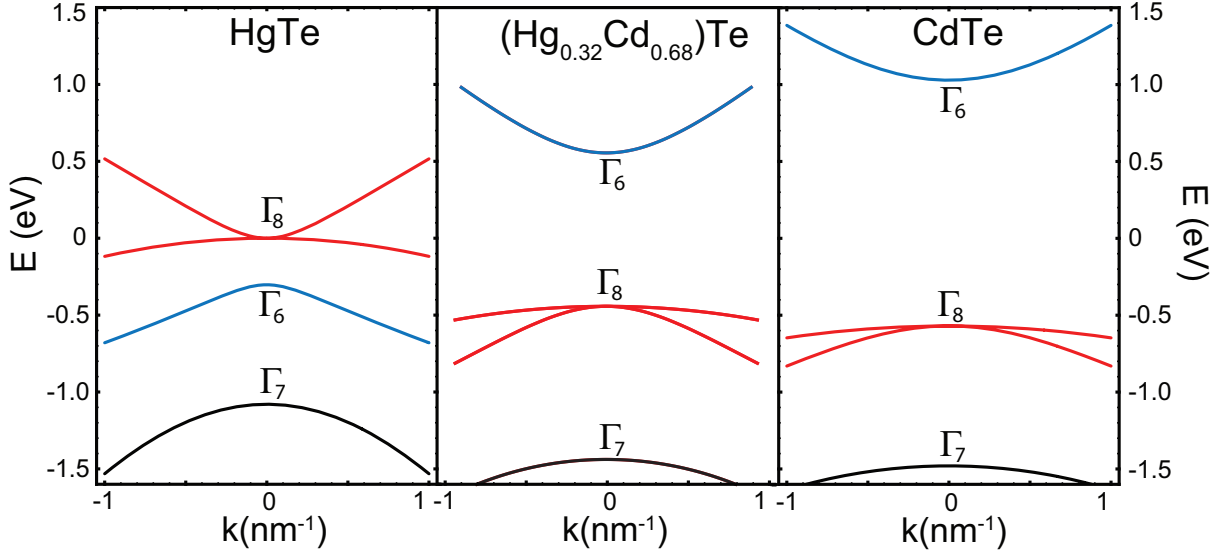


**Fig. 3.1:** Band structures of HgTe, CdTe and their ternary compound  $\text{Hg}_{0.32}\text{Cd}_{0.68}\text{Te}$  calculated by the Kane model [PJ00].

$\text{Hg}_{0.32}\text{Cd}_{0.68}\text{Te}$  are depicted in fig. 3.1. It has been derived by numerical calculations using the standard Kane model [PJ00]. All systems exhibit their band extrema at the  $\Gamma$ -point of the Brillouin zone.

CdTe exhibits a similar band structure to the well-known semiconductor GaAs with an s-type conduction band ( $\Gamma_6$ ,  $J = 1/2$ ) and p-type valence bands ( $\Gamma_7$ ,  $J = 1/2$ ;  $\Gamma_8$ ,  $J = 3/2$ ). The  $\Gamma_8$  band splits into the light ( $m_j = \pm 1/2$ ) and heavy hole ( $m_j = \pm 3/2$ ) part. The band gap defined by  $E_G = \Gamma_6(k=0) - \Gamma_8(k=0)$  equals about  $1.6 \text{ eV}$  for  $T = 0 \text{ K}$ .

The band structure on the left belongs to HgTe and shows a semi-metal progression. The  $\Gamma_8$  band lies above the  $\Gamma_6$  band and the energy gap defined by  $\Gamma_6 - \Gamma_8$  equals  $-300 \text{ meV}$  for  $T = 0 \text{ K}$ . The switching of both bands leads to the particular order of the s-type  $\Gamma_6$  band lying between the heavy/light hole band  $\Gamma_8$  and the split-off band  $\Gamma_7$ . This is called an *inverted* band structure. The light hole bulk subband of  $\Gamma_8$  now becomes the conduction band and the heavy hole subband is the first valence band. The real band gap in terms of transport is zero, due to the twofold degeneracy of the  $\Gamma_8$  band at  $\mathbf{k}=0$ .

The ternary system  $\text{Hg}_x\text{Cd}_{1-x}\text{Te}$  is obtained by combining the two bulk materials. Figure 3.1 middle shows that the band order remains as in CdTe. The energy gap can be tuned by the ratio  $x$  and equals about  $1 \text{ eV}$  for  $x = 0.32$ .

When bringing the materials together in a heterostructure, using  $\text{Hg}_{0.32}\text{Cd}_{0.68}\text{Te}$  as the barrier and  $\text{HgTe}$  as the well material, a quantum well is generated. The motion of the electrons is then restricted in one direction and a two-dimensional electron gas forms (see fig. 2.7 in section 2.2.1.1). The band structure of this quantum well was derived in [PJ00, NPJJ<sup>+</sup>05]. The degeneracy of the  $\Gamma_8$  band is lifted and the light hole band is shifted to lower energy far away from the Fermi energy ( $E < -0.1 \text{ meV}$ ) for typical quantum well widths ( $4 \text{ nm} < d_{QW} < 15 \text{ nm}$ ) - thus not taking part in electronic transport. Moreover, the quantum confinement leads to discrete energy niveaus. The  $\Gamma_6$  band decomposes into the electron-like  $E_i$  and the heavy hole-like  $\Gamma_8$  band into  $H_j$  levels. The progression of these levels depends on  $d_{QW}$  and is depicted in fig. 3.2a.

For a very wide well the first niveau is close to that of bulk  $\text{HgTe}$  material and stays inverted (see fig. 3.2b right). But with decreasing  $d_{QW}$  the energy levels of the  $\Gamma_6$  band ( $E_i$ ) shift significantly to higher energies and those of the  $\Gamma_8$  band ( $H_j$ ) to lower ones, and eventually cross at a critical quantum well width  $d_c \approx 6.3 \text{ nm}$ . With further decrease in  $d_{QW}$ , a "normal" order of the bands is obtained, thus electron-like states form the conduction band and hole-like states the valence band (see fig. 3.2b).

The inversion for  $d > d_c$  in this material system leads to the occurrence of the quantum spin Hall effect (QSHE) that demonstrated the first transport experiments on a 2D topological insulator [KWB<sup>+</sup>07, KBMH08]. Its outstanding property for Fermi energies lying in the band gap is the not vanishing conductance of  $2e^2/h$  due to edge channel transport in a zero magnetic field.

Before the experimental discovery the effect was predicted by Bernevig and Hughes [BHZ06]. The prediction was facilitated by the proposal of an analytically solvable model, the so-called *effective* Hamiltonian (or effective model). The band structure derived from that resembles the band structure calculated by the numerical Kane model for low energies. The effective Hamiltonian exhibits several parameters, namely  $\mathcal{A}, \mathcal{B}, \mathcal{C}, \mathcal{D}$  and  $\mathcal{M}$ , in order to be able to fit the derived band structure to the accurate Kane model. The effective model is - as opposed to standard 2DEGs - based on the Dirac Hamiltonian. Thus, when describing an electronic band structure, it mimics the band dispersion of

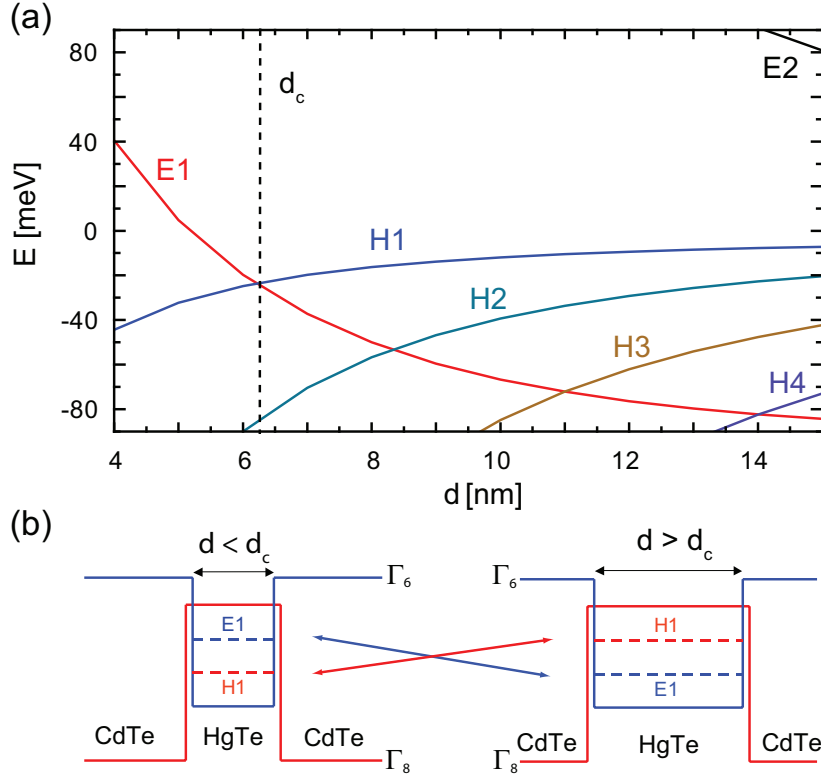


**Fig. 3.2:** (a) Progression of the  $E_i$  and  $H_j$  subbands depending on the thickness  $d$  of the HgTe quantum well (b) Sketches showing a normal QW and the transition to an inverted QW.

Dirac fermions in condensed matter.

The calculation of the energy spectrum for bulk HgTe is analytically solvable and given by

$$E_{\pm} = \mathcal{C} - \mathcal{D}k^2 \pm \sqrt{\mathcal{A}^2k^2 + (\mathcal{M} - \mathcal{B}k^2)^2} \quad (3.1)$$

Some of the introduced fitting parameters have an obvious physical meaning.  $\mathcal{C}$  sets an offset to the energy. For  $k = 0$  the energy gap is given by  $E_+ - E_- = 2\mathcal{M}$ , thus  $\mathcal{M}$  determines the band gap and is called the "Dirac mass". The term  $\mathcal{M}_{\hat{k}} = \mathcal{M} - \mathcal{B}k^2$  is called the *effective* Dirac mass and describes the  $k$ -dependent energy gap for finite  $k$ -values.

Using the envelope function approximation the effective model is also suitable for the description of semiconductor heterostructures. The comparison of the band structure

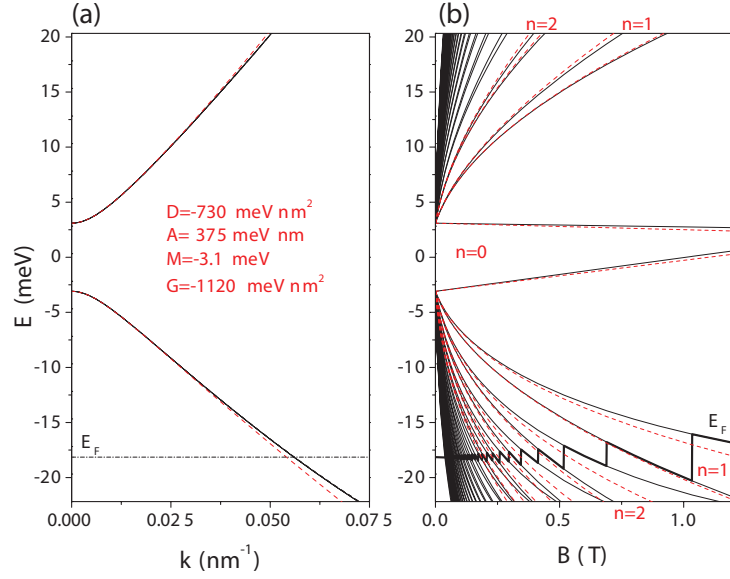


**Fig. 3.3:** Comparison of band structures for HgTe wells derived by the Kane model (black lines) and the effective model (red dashed) (a) Energy dispersion in k-space (b) Landau level progression in a magnetic field. Taken from [SNKT09].

derived by the effective model and the Kane model was carried out in [SNKT09]. The heterostructure of interest was a typical HgTe quantum well, with a well width of  $6.5 \text{ nm}$ , and a carrier concentration of  $5 \cdot 10^{10} \text{ cm}^{-2}$ . The result is depicted in fig. 3.3. The solid black lines correspond to the accurate Kane model and the dashed red lines to the effective model. The energy dispersions of both models coincide for low k-values.

The successful description by a Dirac Hamiltonian makes the HgTe quantum well a realization of massive Dirac fermions in condensed matter. Moreover, HgTe QWs exhibit the remarkable possibility to tune the Dirac mass  $\mathcal{M}$  by varying the quantum well width of the heterostructure in the growth process. The validity of the effective Hamiltonian in presence of a magnetic field has been proven. The splitting into Landau levels (Landau level fan chart) was calculated analytically and is consistent with the numerically obtained solution for low energies (fig. 3.3b, [SNKT09]).

The effective model is therefore suited to describe the band structure of a HgTe quantum well system in magnetic fields and can be further exploited to theoretically investigate optical parameters, quantum transport and more properties of this system.

Transport measurements which show effects based on the special Dirac-like band struc-

ture will be presented in the next chapters. First, a zero-gap HgTe QW with vanishing Dirac mass  $\mathcal{M}$  is investigated. Subsequently, the unusually prominent weak anti-localization effect observed in this material will be comprehensively examined in experiments in order to find out whether it is inherent to Dirac systems.

## 3.2 Single Valley Dirac Fermions in Zero-Gap HgTe Quantum Wells

In recent years the material graphene (a single sheet of graphite) has gained a lot of interest - both by experimentalists and theoreticians. The reason for that is on one hand the high mobility, and on the other the specific band structure. The two-dimensional system can be described by a Dirac Hamiltonian and was therefore the first realization of Dirac fermions in condensed matter. The lattice of graphene, with its hexagonal structure, has a unit cell with a basis of two atoms, leading to two inequivalent sublattices A and B. The low-energy spectrum mimics two massless Dirac cones (one for each valley), both being spin-degenerate. Therefore four Dirac cones in total exist in this material. Massless in this sense means that the Dirac mass  $\mathcal{M}$  (thus the band gap) in this system equals zero.

Many theoreticians have been inspired to investigate the peculiarities in transport and other properties arising from the linear band structure in graphene. Unfortunately, many predictions rely on the presence of only one spin-degenerate Dirac valley in the Brillouin zone or, at least, weak intervalley scattering. Thus graphene is not the suitable material to investigate these predictions because it exhibits two sublattices A and B which are connected by strong intervalley scattering.

The attempts in achieving a Dirac mass  $\mathcal{M} \neq 0$  in single-layer graphene have not yet been successful - opposing HgTe with a tunable Dirac mass  $\mathcal{M}$  as described in the previous section. For research a tunable mass is a very interesting playground, and a band gap is desirable for devices in order to control the electronic transport.

In this section, low-temperature experiments on a HgTe quantum well with a Dirac mass  $\mathcal{M} = 0$  or a quantum well width of  $d = d_c \cong 6.3 \text{ nm}$  will be presented.

### 3.2.1 Energy Dispersion for $\mathcal{M} = 0$

As previously mentioned, the energy dispersion of a HgTe heterostructure can be approximated for low  $k$  values by the effective model yielding the eigenvalues:

$$\begin{aligned}
E_{H_1} &= \mathcal{C} - \mathcal{D}k^2 + \sqrt{\mathcal{A}^2k^2 + (\mathcal{M} - \mathcal{B}k^2)^2} \\
E_{E_1} &= \mathcal{C} - \mathcal{D}k^2 - \sqrt{\mathcal{A}^2k^2 + (\mathcal{M} - \mathcal{B}k^2)^2}
\end{aligned} \tag{3.2}$$

The Dirac mass  $\mathcal{M}$  can be tuned from negative to positive values. For a HgTe quantum well with  $d = d_C$  the Dirac mass  $\mathcal{M} = 0$ . Moreover, for low  $k$  values (close to the  $\Gamma$  point) the quadratic term  $\mathcal{D}k^2$  can be neglected and the term with  $\mathcal{A}$  dominates. The energy dispersion can then be approximated by a linear progression:

$$E_{\pm}(k) \propto \pm \mathcal{A}k \tag{3.3}$$

To confirm the energy dispersion for this special case, the standard Kane model was used as well. The result is shown in fig. 3.4a. The linear progression holds true up to  $k$  values of about  $0.1 \text{ nm}^{-1}$  for the crystal direction  $[0,1]$  and  $[1,1]$ . The band structure was

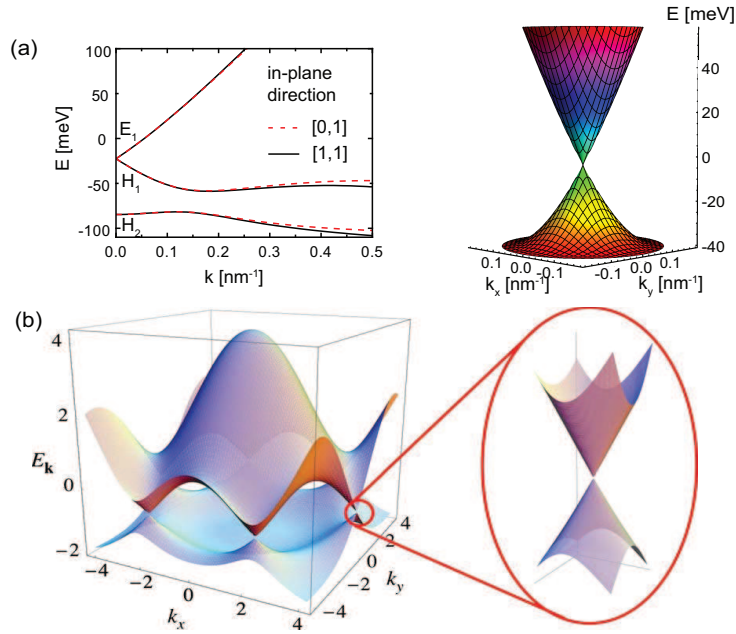


**Fig. 3.4:** Manifestations of Dirac cones in condensed matter (a) HgTe quantum well: one Dirac cone (b) Graphene: two Dirac cones for A and B obtained by a tight binding approach for the whole Brillouin zone (taken from [CNGP<sup>+</sup>09]).



derived earlier for many directions in the Brillouin zone [PJ00]. It was found to be very symmetric with the [1,1] direction deviating the most from the [1,0] direction. Thus one can state that the resulting energy dispersion for  $\mathcal{M} = 0$  resembles a Dirac cone at the  $\Gamma$ -point (see fig. 3.4a right).

In comparison to graphene (fig. 3.4b), the HgTe quantum well with  $d = d_c$  exhibits only one valley, and thus no valley degeneracy whereas the spin degeneracy exists in both systems without external fields. In that sense one can say the quantum well HgTe ( $\mathcal{M} = 0$ ) is "half-graphene". However, it must be stated that non-linearities in  $k$ , such as the quadratic terms in (3.2), come earlier into play than in graphene.

### 3.2.2 Fabrication and Measurement Setup

In these studies several modulation-doped HgTe/(Hg<sub>0.32</sub>, Cd<sub>0.68</sub>)Te quantum well structures with quantum well widths ranging from 5.0 to 7.5 nm (yielding positive as well as negative Dirac masses  $\mathcal{M}$ ) have been investigated. Furthermore, several quantum wells were grown aiming for the critical well width  $d_c = 6.3$  nm.

The wafers were processed into Hall bar devices with dimensions (length  $L \times$  width  $W$ ) of  $(600 \times 200)$  and  $(20.0 \times 13.3)$   $\mu\text{m}^2$  using optical lithography processes adjusted to the low heat tolerance of the material (process details are given in table A.3). The following Ar sputtering step with Ti as the etch mask transfers the Hall bar geometry to the heterostructure. For gating purposes a 100 nm thick  $\text{Si}_3\text{N}_4/\text{SiO}_2$  multilayer gate insulator and a 5/50 nm Ti/Au gate electrode are deposited. The Ohmic contacts were performed by thermal indium bonding. The grown quantum wells were n-conducting at zero gate voltage and exhibited carrier concentrations of about  $n_{2D} \cong 5 \times 10^{11} \text{ cm}^{-2}$  and mobilities of several  $10^5 \text{ cm}^2\text{V}^{-1}\text{s}^{-1}$ . Typically, a bias voltage of up to 10 mV was applied between the current contacts 1 and 6 (see fig 3.6a). This resulted in a current  $I$  in the order of about 1  $\mu\text{A}$  which was determined by the voltage drop across a reference resistor in series with the sample. The longitudinal ( $V_x$ , contacts 3 and 5) and transverse ( $V_H$ , contacts 2 and 3) voltages were detected simultaneously in a 6-point measurement setup, yielding the longitudinal ( $\rho_{xx} = V_x/I \times W/L$ ) and transverse ( $\rho_{xy} = V_H/I$ ) resistivities.

The electron density (and thus the Fermi energy) can be varied by applying a gate voltage  $V_G$  between the top electrode and the 2DEG. As reported previously [KBMH08], the carrier density can be varied from n- to p-type conduction for more negative gate voltages. The gate voltage has been restricted to  $|V_G| < 3V$  in order to prevent hysteretical effects [HBS<sup>+</sup>06]. The transport measurements were carried out in a setup with a variable temperature cryostat at  $4.2K$  as described previously (see fig. 2.18), unless stated otherwise.

Since no growth calibration is sufficiently precise to consistently grow a quantum well with the critical thickness, and the direct measurement of the buried well is intricate, we developed a simple nondestructive method to assess the well thickness.

### 3.2.3 Identification of the Energy Gap Using the Quantum Hall Effect

For better understanding of the method, the Landau level fan chart (fig. 3.5a) for a sample with a normal quantum well ( $d = 5.7nm < d_c$ ) will be discussed. This chart was obtained by adjusting the Kane model to experimentally obtained magnetic field sweeps for various gate voltages. The nominal values of the growth process (thickness, doping) serve as a valuable starting point.

Since the sample is a normal structure, the  $E_1$  subband lies above the  $H_1$  subband. Therefore there is no crossing of the lowest Landau levels, which is typical for inverted quantum wells. Moreover, the spin degeneracy is already lifted for very low fields due to the high g-factor present in HgTe QW as described in [BLT<sup>+</sup>11]. The typical characterization includes a magnetic field sweep (as depicted in fig. 3.5b). Here the longitudinal and transverse resistivities are measured and can be used to evaluate carrier concentration and mobility of the material. It corresponds to a horizontal measurement in the Landau level fan chart as shown by the red line in fig. 3.5a). The maxima of the longitudinal resistance (orange curve) correspond to the hitting of the LLs with the filling factors  $\nu$  (compare section 2.2.3) and can be assigned by the measurement of the Hall resistance. Here for example the last full plateau is at  $h/6e^2 \approx 4.3k\Omega$  so the following peak in  $\rho_{xx}$  corresponds

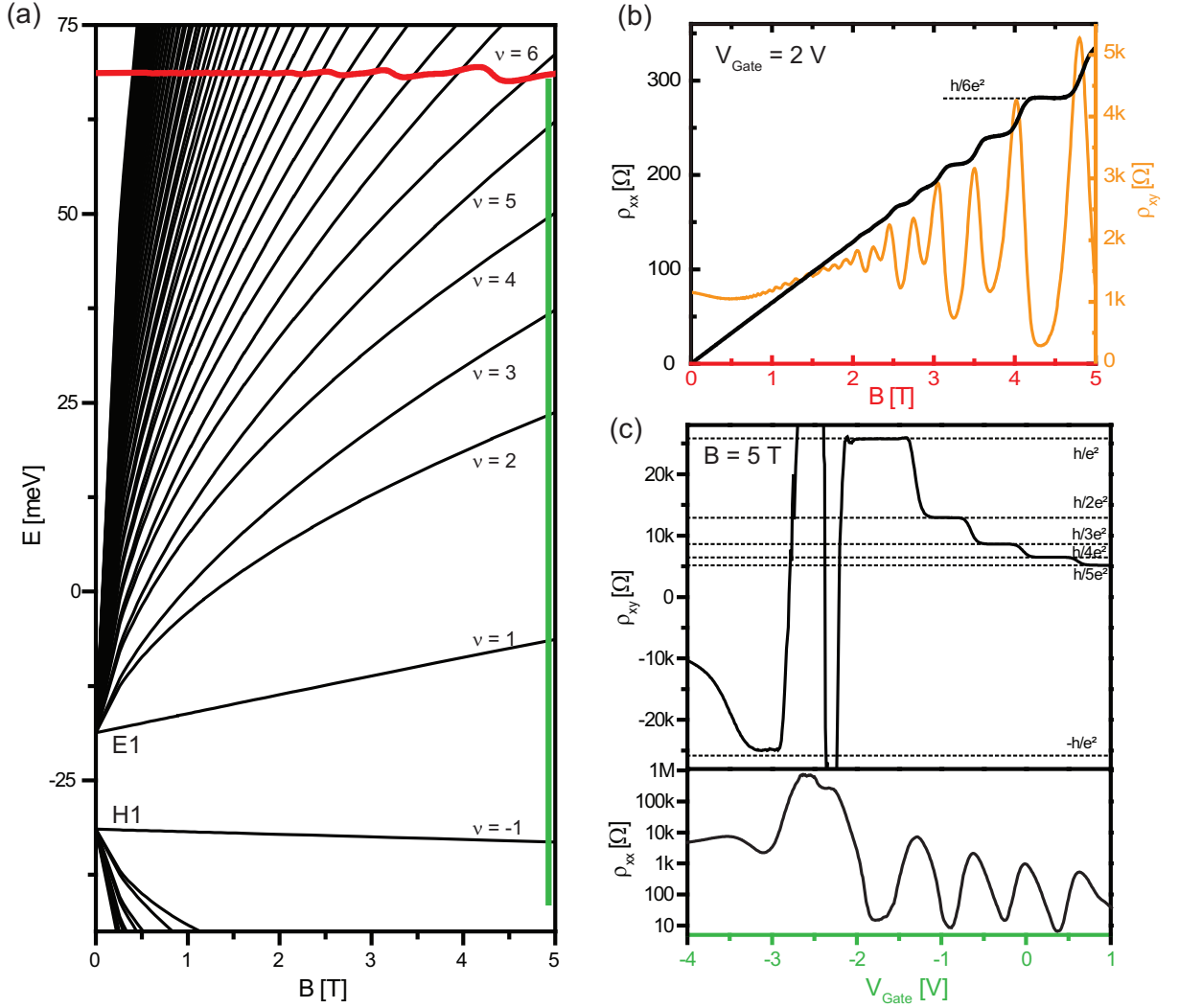


**Fig. 3.5:** Illustration of a magnetic field sweep and a gate voltage sweep by means of a calculated LL fan chart (a) Landau level fan chart based on the Kane model for a normal quantum well with a well thickness  $d = 5.7 \text{ nm}$ ; the Landau levels are spin-resolved; the red line indicates the measurement for a B-field variation from  $0 \text{ T}$  to  $5 \text{ T}$  for a constant gate voltage of  $V_{\text{Gate}} = +2 \text{ V}$  whereas the green line indicates a measurement sweeping the gate voltage at a constant magnetic field of  $5 \text{ T}$  (b) Measurement of  $\rho_{xy}$  and  $\rho_{xx}$  for  $V_G = 2 \text{ V}$  corresponding to the red line of (a) - hitting of the LLs manifests in maxima of the SdH oscillations which can be assigned to the filling factors by simultaneous  $\rho_{xy}$  data (c) Gate voltage sweep corresponding to the green line in (a) at a constant magnetic field of  $5 \text{ T}$  - the  $\rho_{xy}$  data shows hitting of Landau levels starting from  $h/5e^2$  up to  $h/e^2$ . Subsequently, the energy gap is reached and the sample becomes insulating for about  $-2.9 \text{ V} < V_G < -2.1 \text{ V}$  and reaches the p-conducting side with  $-h/e^2$ . The  $\rho_{xx}$  data is drawn in logarithmic scale and exhibits its maxima when Landau levels are hit. In the gap the sample turns insulating with a resistivity in order of  $1 \text{ M}\Omega$ .

to the filling factor  $\nu = 6$ . Performing a gate sweep with a fixed magnetic field (fig. 3.5c) is equivalent to a vertical measurement in the Landau level chart and corresponds to the green line in fig. 3.5a. Here the starting point is the end of fig. 3.5b and the first plateau is at  $h/5e^2$  followed by the SdH peak with the filling factor  $\nu = 5$ . It must be noted that the gate voltages are slightly shifted due to the occurrence of interfacial states as described in [HBS<sup>+</sup>06]. The charging and discharging of these states leads to hysteretical behavior and acts as an extra capacitor, strengthening/weakening the externally applied gate voltage. With lower gate voltages lower LLs are crossed, hitting  $\nu = 1$  for a gate voltage of  $-2.1 V$ . The sample enters the energy gap and thus the insulating region. Since this quantum well belongs to the normal regime the sample is truly insulating and the QSHE is absent. For even lower  $V_G$  the p-conducting regime is reached hitting  $\nu = -1$  followed by the quantum Hall plateau at  $-h/e^2$ .

The latter gate sweeps were found to be a simple nondestructive method to assess the energy gap (proportional to  $\mathcal{M}$  or  $d_{QW}$ ). The position of the Landau levels with the filling factors  $\nu = \pm 1$  can be mapped by performing several gate sweeps at various magnetic fields. In detail, the crossing point of the lowest LLs for the  $E_1$  and  $H_1$  subband is a precise measurement of the well thickness. Calculating the Landau levels of the effective Hamiltonian in a magnetic field [BLT<sup>+</sup>11], it has been found that two "zero modes" ( $n = 0$ ) with opposite spin orientation exist. This is one of the important differences between Landau levels described by a Dirac Hamiltonian and those for more traditional 2DEGs (compare section 2.2.3). The energy dispersion of the zero modes in a magnetic field is given by:

$$E_0^\uparrow = \mathcal{C} + \mathcal{M} - \frac{eB_\perp}{\hbar}(\mathcal{D} + \mathcal{B}) \quad (3.4)$$

$$E_0^\downarrow = \mathcal{C} - \mathcal{M} + \frac{eB_\perp}{\hbar}(-\mathcal{D} + \mathcal{B}) \quad (3.5)$$

$E_0^\uparrow$  stands for the  $n = 0$  LL for the spin-up particles ( $\nu = 1$ ) and  $E_0^\downarrow$  for the spin-down particles ( $\nu = -1$ ).  $B_\perp$  is the perpendicular magnetic field. The spin splitting can be derived by subtraction and equals:

$$E_0^\uparrow - E_0^\downarrow = 2\mathcal{M} - 2\mathcal{B}\frac{eB_\perp}{\hbar} \quad (3.6)$$

The spin splitting increases linearly with the applied magnetic field. Using (3.6) and setting  $E_0^\uparrow = E_0^\downarrow$ , a critical magnetic field  $B_c = \hbar\mathcal{M}/(e\mathcal{B})$  can be found where the two zero-mode levels become degenerate. Since  $\mathcal{B} < 0$  for all observed HgTe QWs, this critical or "crossing" field  $B_c$  occurs for inverted samples ( $\mathcal{M} < 0$  thus  $\mathcal{M}/\mathcal{B} > 0$ ) for positive magnetic fields. For normal samples, however, the crossing extrapolates to (non-physical) negative magnetic fields. In the case of a well with quantum well thickness of  $d = d_c$  ( $\mathcal{M} = 0$ ), the crossing takes place for  $B_c = 0 T$  - at zero magnetic field. Keeping this in mind, the knowledge about the crossing point of the two lowest LLs gives information about the type of quantum well ( $\mathcal{M} > 0$  normal,  $\mathcal{M} < 0$  inverted) and directly indicates the existence of a Dirac point ( $\mathcal{M} = 0$ ) in the quantum well.

In fig. 3.6a the Hall conductivity  $\sigma_{xy} = \rho_{xy}/(\rho_{xy}^2 + \rho_{xx}^2)$  for the sample with  $\mathcal{M} = 0$  at magnetic fields of 5, 4, 3, 2 and 1 Tesla is plotted. It must be noted that, in principle, the quantized value in the quantum Hall effect is  $\sigma_{xy}$  and not  $\rho_{xy}$ . For the typical quantum Hall effect  $\rho_{xx}$  vanishes. From this follows that  $\rho_{xy} = \sigma_{xy}^{-1}$ . Here, on the contrary,  $\rho_{xx}$  does not vanish when entering the insulating region and must be taken into account. In the following, the gate voltage has been offset for comparison reasons, such that  $V_G - V_{Dirac} = 0 V$  and corresponds to the Dirac point. The point varies between different cool downs, but is typically in the order of  $-1.2 V$ .

As one can see, the quantum Hall plateaus are well developed even for the lowest field of  $1 T$ . Therefore, the  $\nu = \pm 1$  Landau levels can be easily identified by the boundaries of the zero plateau  $\sigma_{xy} = 0$  for each magnetic field. The shifting of the curves by  $e^2/h$  per Tesla does not only serve for clarity but the axis can be translated into a magnetic field axis with a spacing of  $1 T$  between the scans. With this " $B_\perp$ "-axis being drawn on fig. 3.6a right-hand, a linear extrapolation is performed in the graph (indicated by the red and black dashed lines). In this case the extrapolation leads to  $B_c \approx 0 T$  - the sample exhibits a Dirac mass close to zero.

This zero-gap sample was found after systematical measurements on several samples.

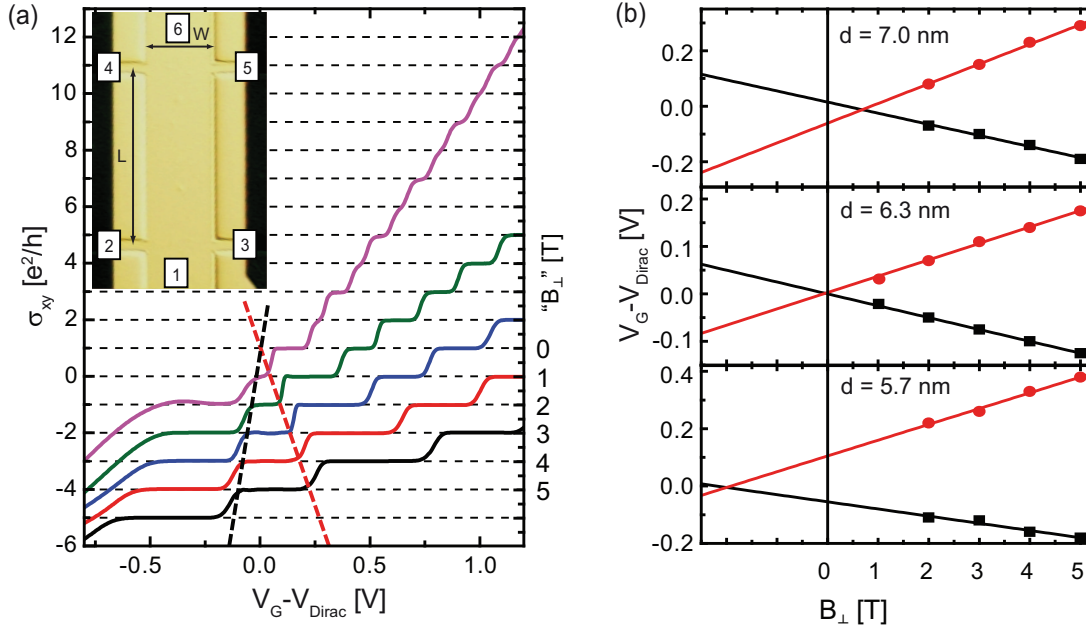


**Fig. 3.6:** (a) Quantum Hall measurement data on the sample with  $d = d_c$ . Curves taken by swept gate voltage (Fermi energy) for constant fields of (from top to bottom) 1 (purple), 2 (green), 3 (blue), 4 (red) and 5 (black) Tesla. The curves are offset, the  $\sigma_{xy}$  scale belongs to the 1 T curve. The traces for higher fields are shifted down by  $e^2/h$  and thus a  $B_{\perp}$ -axis for the zero plateau can be drawn on the right axis in order to determine  $B_c$ . (Inset) Exemplary micrograph of Hall bar with length  $L$ , width  $W$  and an Au top gate (b) Evaluation of  $B_c$  for three quantum wells grown close to  $d_c$ , the middle shows a crossing for  $0T$ , thus  $\mathcal{M} \approx 0$ .

The feasibility of this method to give a quick inference to the Dirac mass of the quantum well is shown in fig. 3.6b. Here the magnetic field-dependent position of the LLs with  $\nu = \pm 1$  for three different samples is depicted. The upper panel exhibits a crossing for positive magnetic fields - this sample is inverted. In a detailed fitting of the SdH-oscillations to the Kane model the well thickness was determined to be  $d = 7.0 \text{ nm}$  - confirming the validity of the method. The graph in the middle is the extrapolation data of fig. 3.6a, rotated by  $90^\circ$  counterclockwise, bearing the known intersection at  $B_c = 0T$  thus indicating  $\mathcal{M} = 0$ . The third panel shows an intersection for a magnetic field  $B_c < 0T$  and therefore belongs to a sample with normal band structure. This in fact holds true, since this sample belongs to the band structure already known from fig. 3.5 and bears a well width of  $d < d_c = 5.7 \text{ nm}$ .

This method is therefore suitable to perform a quick screening of samples.

### 3.2.4 Characterization of the Zero-Gap Sample

In this section the sample with the crossing field  $B_c = 0 T$  will be further investigated. First, the peculiarities of the quantum Hall measurements due to the Dirac Hamiltonian are described for this HgTe well. The Hall conductivities of the sample for a magnetic field of 1 T and 5 T are shown in fig. 3.7, alongside the longitudinal resistivity exhibiting Shubnikov-de Haas oscillations.

Obviously, the quantization in  $\sigma_{xy}$  is distinctive for both magnetic fields. Taking a closer look at the 1 T curve (fig. 3.7a), the plateaus are wider and more pronounced for odd multiples of  $e^2/h$  ( $\nu = 1, 3, 5, \dots$ ). Furthermore, the even integer plateaus already start to come into existence due to spin-splitting. This order differs from the one in typical 2DEGs. In e.g. GaAs - for low magnetic fields - the lowest Landau level is not spin-resolved yet and would only exhibit a plateau at  $e^2/2h$  in this type of measurement. In contrast the Landau level  $\nu = +1$  in this sample is very wide even at low magnetic fields. This is a direct consequence of the Dirac physics involved in this system [CNGP<sup>+</sup>09]. Moreover, the well developed plateaus occur at one half of the conductivity values of graphene [NGM<sup>+</sup>05, GN07] and can be clearly assigned to the absence of the valley degeneracy in the HgTe quantum well, whereas the spin degeneracy is present in both systems.

Another remarkable difference between these two Dirac systems is the always observable plateau for  $\sigma_{xy} = 0$  in the Hall curves of HgTe. Concomitantly, the longitudinal resistivity shows fairly high values, indicating a gapped system as a result of spin-splitting, even at fields as low as 1 T. In the 5 T curve (fig. 3.7b) all plateaus are fully spin resolved at integer values in  $e^2/h$ , with a nearly constant plateau width and simultaneous SdH-oscillations when the Fermi energy hits an LL.

For clear proof that this sample is in fact described by a Dirac Hamiltonian with  $\mathcal{M} = 0$  for low energies, the evolution of Landau levels was investigated in a perpendicular magnetic field and varied Fermi energies. In order to achieve a detailed mapping of  $\sigma_{xy}$  in the energy and magnetic field space, numerous gate voltage sweeps were taken - each at a

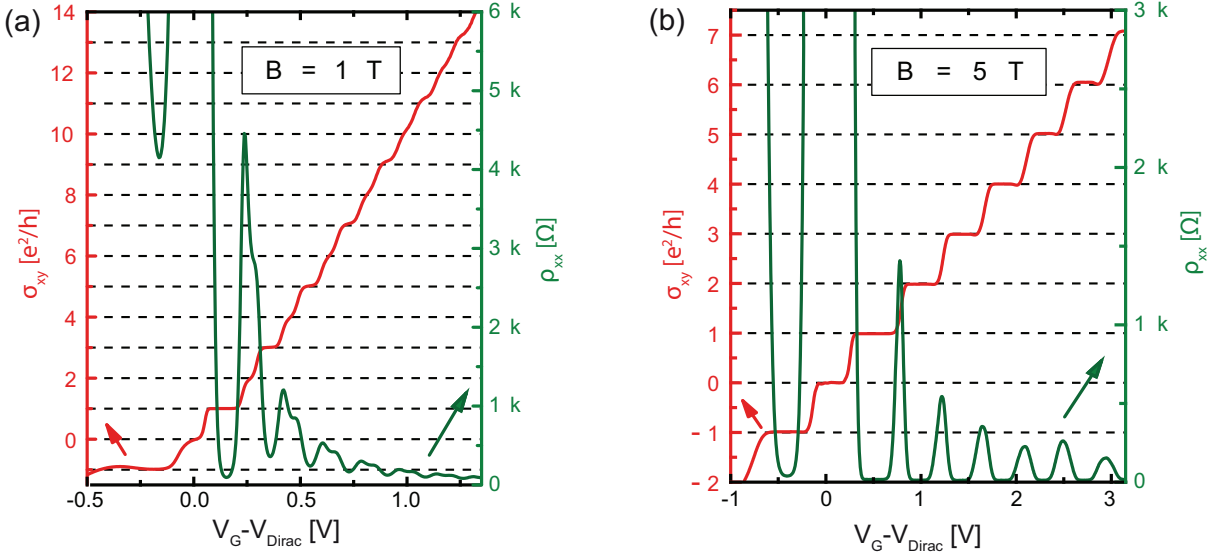


**Fig. 3.7:** Hall conductivity and longitudinal resistivity measurements for the zero-gap sample at magnetic fields of (a) 1 T and (b) 5 T, respectively.

constant (stepped) magnetic field. The position of the Landau levels can then be obtained by calculating and plotting the derivative  $\partial\sigma_{xy}/\partial V_G$  in a color-coded contour plot as a function of both magnetic field  $B$  and gate voltage  $V_G$ . This is correct since  $\sigma_{xy}$  exhibits its extremal slope when hitting an LL and thus the brightest colors in fig. 3.8 indicate the Landau levels. An exemplary measurement for one curve of  $\sigma_{xy}$  and the corresponding deviation is shown in fig. 3.8a.

Based on the band structure calculations, the gate voltage scale now needs to be translated into an energy scale. For this purpose the gate is taken as a plane capacitor plate. Then the energy  $E(n_e)$ , depending on the electron concentration, is calculated using the Kane model under the assumption  $\mathcal{M} = 0$ . This calculation was used to derive the density of states (DOS) as a function of a magnetic field, and was cross-checked with the experimental data of the Shubnikov-de Haas oscillations. The result is depicted in fig. 3.10a. The node positions in the SdH signal coincide accurately with the nodes in the DOS calculations. The overlap between experiment and theory is a proof for the validity of the underlying Kane model.

The y-axis of the contour plot (fig. 3.8b) is translated with the achieved function  $E(V_G)$ . The result is shown in fig. 3.9. The dashed white lines in fig. 3.9a represent an



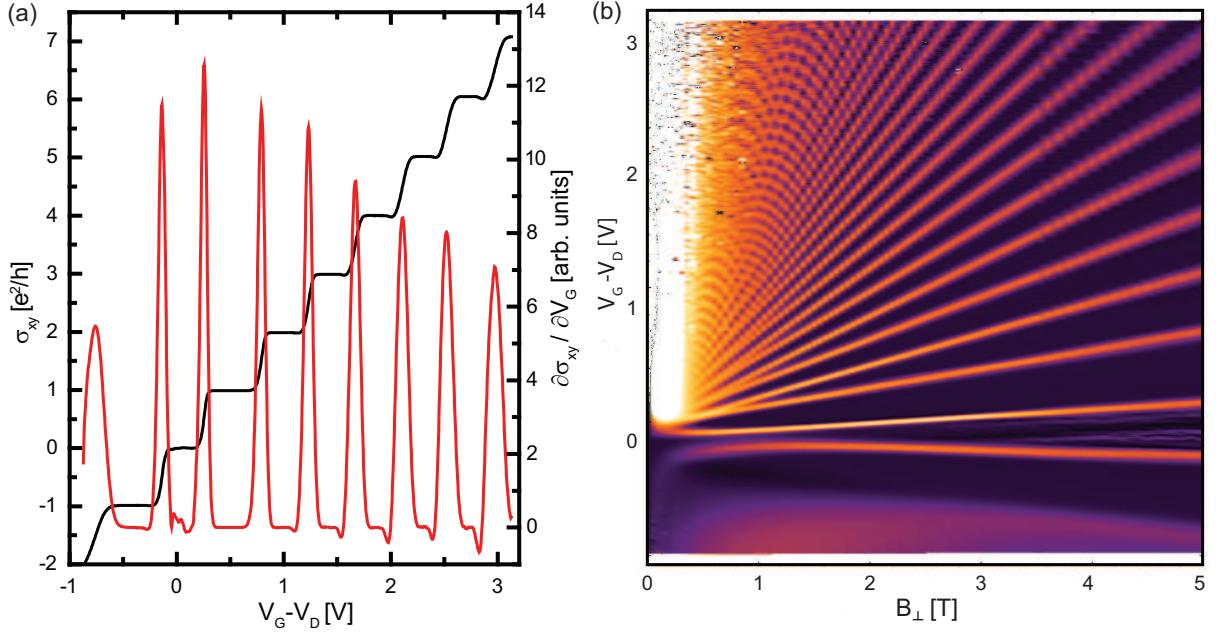


**Fig. 3.8:** (a) Measurement at constant  $B = 5 T$ : (black) Hall conductivity and (red) first derivative (b) Contour plot of  $\partial\sigma_{xy}/\partial V_G$  in the magnetic field and gate voltage space.

overlay and show the calculated Landau level dispersion based on the Kane model. The very good agreement of this calculation with the experimental peaks in  $\partial\sigma_{xy}/\partial V_G$  is more evidence that the  $V_G$  to E conversion is self-consistent.

But the question is how the experimental Landau levels mimic the progression expected from the Dirac Hamiltonian. Solving the effective Hamiltonian in the presence of a magnetic field and with  $\mathcal{M}, \mathcal{C} = 0$  (shifting the Dirac point to zero energy), the equation for the Landau levels of  $n$ th order was calculated [BLT<sup>+</sup>11] and equals for the conduction band in low magnetic fields:

$$E_C^{\uparrow,\downarrow} \approx -\frac{e}{\hbar} B_\perp (2Dn + \mathcal{B}) \mathcal{A} \sqrt{2n \left( \frac{e}{\hbar} B_\perp \right)} \quad (3.7)$$

In standard semiconductors with parabolic band dispersion the Landau levels progression is linear in B (see section 2.2.3). Here, on the contrary, the Landau levels exhibit a square-root magnetic field dependence, as it is typical in Dirac fermion systems, such as graphene. The difference to graphene, however, is the additional linear term which is a consequence of the large effective g-factor in the HgTe quantum well system.

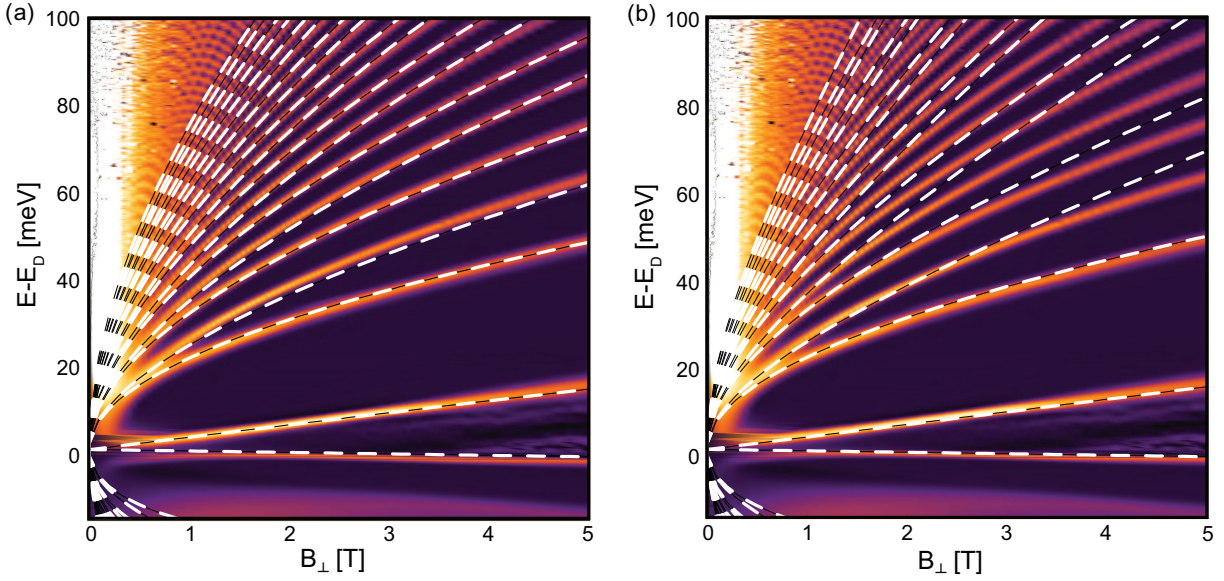


**Fig. 3.9:** Contour plot of  $\partial\sigma_{xy}/\partial E$  with calculated LL dispersion (b/w dashed) for the (a) Kane model (b) Effective model.

The effective model was extended by taking Zeeman contributions into account. The dashed white lines in fig. 3.9b correspond to the best fit of this extended model. The result is that this Dirac model adequately describes the experimental data for low Landau indexes  $n$  and low energies. However, it breaks down for energies  $E - E_D > 45\text{meV}$  when the energy dispersions of the effective model and the Kane model start to deviate significantly.

Another possibility to show the linearity in  $k$  for low energies and the increasing parabolic term for higher energies is to investigate the evolution of two different gap types for low and high gate voltages as will be shown shortly. A typical way to investigate the nature of the energy dispersion in a magnetic field is the dependence of Landau levels on magnetic fields.

It is useful to compare the Landau level dispersion of a Dirac system [Hal88, ZTSK05] and a typical parabolic system (e.g. GaAs/AlGaAs):

$$E_{Dirac}(N) = \sqrt{2e\hbar v_F^2 N B_\perp} \quad (3.8)$$

$$E_{parabolic}(N) = \frac{\hbar e B_\perp}{m^*} \left( N - \frac{1}{2} \right) \quad (3.9)$$

As shown in (3.3), the energy dispersion is linear for low energies. However, for higher energies the parabolic term becomes more and more dominant. Taking a closer look at the equations above, an analysis for the two limiting regimes can be deduced. Since the energy in our system is held constant, a plot of the Landau level versus the inverse magnetic field is instructive. Summarizing all constant terms within the variables C and C' one obtains:

$$N_{Dirac} = C \cdot B_\perp^{-1} \quad (3.10)$$

$$N_{parabolic} = (C' \cdot B_\perp^{-1}) + \frac{1}{2} \quad (3.11)$$

Therefore the extrapolation of the factor N to  $B^{-1} = 0$  gives insight whether the system follows Dirac physics (intercept at N=0) or standard-2DEG physics (intercept at  $N = 1/2$ ). As described in [BLT<sup>+</sup>11] the factor N must be determined from the larger gaps (so-called orbital gaps) which correspond to deep minima in the Shubnikov-de Haas measurements. The shallow minima are due to spin splitting in this material.

In fig. 3.10 the Shubnikov-de Haas measurements and the calculation of the density of states for three different gate voltages ( $V_G = 0, 1, 2 V$ ) are plotted. The density of states was broadened by a convolution with a Gaussian of width  $\Gamma_0 \sqrt{B[T]}$  due to nonzero temperature and crystal impurities with best fit for  $\Gamma_0 = 1.2 \text{ meV}$ . As proven in the graph, the theory reproduces accurately the experimentally obtained curves. The maxima in the measurements appear when the Fermi energy hits the Landau level, whereas a minima occurs for Fermi energy between two LLs. Here there are two different sets of minima in the density of states and the experimental data observable - shallow and deep.

The analysis in fig. 3.10b has been carried out by identifying the middle of the orbital gaps by the deep minima in the longitudinal resistance (circles) and by the middle of the

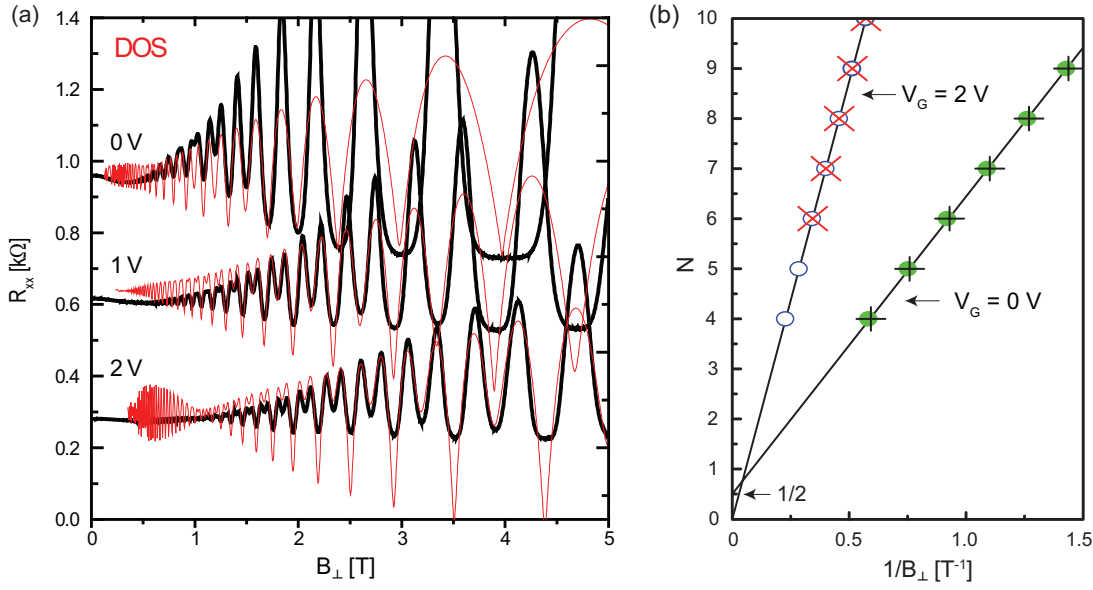


**Fig. 3.10:** (a) Shubnikov-de Haas measurements (thick black lines) for three different gate voltages  $V_G = 2V, 1V, 0V$ . The measurements are offset for clarity by  $700, 500$  and  $200\ \Omega$  for  $V_G = 0, 1$  and  $2V$ , respectively. The thin red lines show the calculated Fermi level density of states of the HgTe quantum well with  $\mathcal{M} = 0$

(b) Graph of the factor  $N$  for  $V_G = 0$  (open blue circles and red  $\times$ -es) and  $V_G = 2V$  (closed green circles and black  $+$ -es) depending on the inverse magnetic field.  $N$  was extracted in two ways: the circles have been obtained by the deep minima in the Shubnikov-de Haas oscillations whereas the crosses were determined from centers of the wide plateaux in  $\sigma_{xy}$ .

corresponding quantum Hall plateau (crosses). For a gate voltage of  $0V$ , which is quite close to the Dirac point  $V_D \approx -1.2V$  of this system, the transport should obey Dirac physics whereas for  $V_G = +2V$  in the second measurement the parabolic term dominates. The linear fit of the data for  $V_G = 0V$  extrapolates to  $N = 1/2$  and for  $V_G = 2V$  to  $N = 0$ . In conclusion, the intercept for  $V_G = 0V$  gives evidence for the Dirac physics in this system. This method has been used before to differentiate between single layer and bilayer graphene [NGM<sup>+</sup>05].

Concluding this section, it was proven that the investigated HgTe quantum well can in fact be described as a zero-gap Dirac system or, in other words, the electrons act as massless Dirac fermions.

### 3.2.5 Measurements Without Magnetic Field

In this section measurements at zero magnetic field are described, thus the spin splitting of the sample is supposed to be zero. In fig. 3.11a the resistivity  $\rho_{xx}$  is plotted against the gate voltage for voltages close to the Dirac point of the sample. As known from graphene samples [BSJ<sup>+</sup>08], the measurement exhibits a Dirac peak around  $(V_G - V_D) = 0 V$ . But, in contrast to graphene, the peak is not symmetric. This is due to the asymmetric density of states in HgTe. The hole band exhibits a high density of states compared to a low density of states for the electron band - opposing to the symmetry between the bands in graphene (see fig. 3.4). Strikingly, the sample does not show insulating behavior, just as expected from a zero-gap HgTe well at zero magnetic field. Note that we can rule out the quantum spin Hall effect which occurs for inverted HgTe quantum wells. This is because the dimensions of the sample are larger by far than the mean free path which leads to a breakdown of this topological phase [RBB<sup>+</sup>09].

To draw further comparison to the well-known Dirac system, graphene, the Dirac peak width is used to measure the quality of the sample. The more homogeneous the sample is, the more precise the Dirac point is achieved over the whole sample. That is why a very narrow peak indicates high-quality samples. In our case the half width of the peak  $\Delta V_G$  in fig. 3.11a corresponds to a charge inhomogeneity of about  $\Delta n \approx 3.0 \times 10^{10} \text{ cm}^{-2}$ . This value is comparable to the charge inhomogeneity due to puddle formation found in suspended graphene [BSJ<sup>+</sup>08].

As already mentioned, the resistivity does not become infinite at any point but instead shows a maximum value for  $\rho_{xx} \approx 71.7 \text{ k}\Omega$  ( $\sigma_{xx} \approx 0.36 e^2/h$ ) at a temperature of 4.2 K. The temperature dependence of the longitudinal conductivity is shown in fig. 3.11b (black circles). Its progression initially resembles a quadratic temperature dependence of up to about 12 K before turning into a linear dependence. The nonzero conductivity at  $V = V_{Dirac}$  (vanishing carrier density) is a manifestation of the singularity inherent to the Dirac cone at the  $\Gamma$ -point in HgTe quantum wells. Thus the occurrence of a minimal conductivity at zero magnetic field gives additional proof of the existence of Dirac fermions in this material.

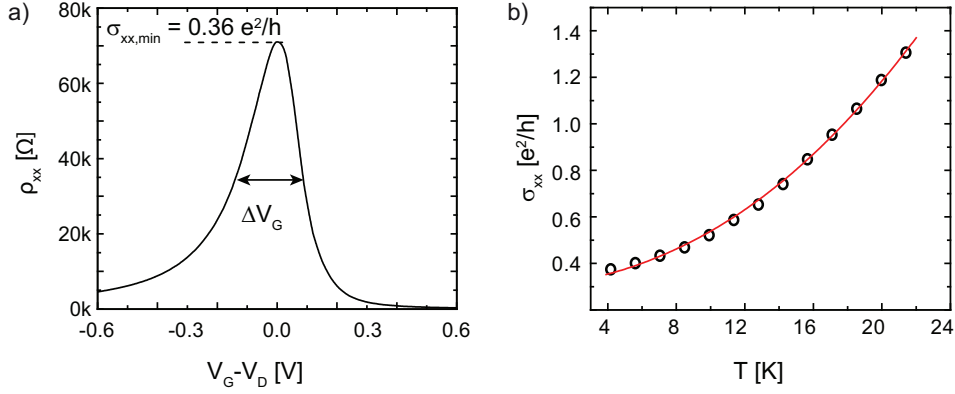


**Fig. 3.11:** Measurements of the longitudinal transport for zero magnetic field (a) Resistivity for gate voltage sweep (b) Temperature-dependent conductivity.

In collaboration with the Department Mesoscopic Physics, University of Würzburg, the minimum conductivity and the temperature dependence of this system has been calculated based on the Kubo formalism and using the effective model with  $\mathcal{M} = 0$  [BLT<sup>+</sup>11]. The consideration of well width fluctuations and potential disorder was necessary in order to describe the real sample accurately. The temperature dependence was found to be:

$$\sigma_{xx} \approx \frac{2e^2}{\pi h} \frac{1}{1 + \langle M^2 \rangle / \Gamma^2} + O\left(\frac{e^2 k_B^2 T^2}{h \Gamma^2}\right), \quad k_B T \ll \Gamma \quad (3.12)$$

$$\sigma_{xx} \propto \frac{e^2 k_B T}{h \Gamma}, \quad k_B T \geq \Gamma \quad (3.13)$$

where  $\Gamma$  describes the spectral broadening due to spin-independent potential disorder. The factor 2 in (3.12) is due to spin degeneracy and  $\langle M^2 \rangle \propto \langle (d_{QW} - d_c)^2 \rangle$  is the variance of the Dirac mass due to fluctuations in the quantum well width  $d_{QW}$ , causing deviations from the critical well width  $d_c$ . X-ray-reflectivity measurements were carried out on other grown HgTe quantum well samples fabricated in the same molecular beam epitaxy chamber and give an estimation of  $\sqrt{\langle \mathcal{M} \rangle} \approx 1 \text{ meV}$  [Sta10]. This value is in the same order as  $\Gamma_0$ , which corresponds to the width of the Gaussian used before, broadening the density of states to match the Shubnikov-de Haas oscillations. Therefore  $\sqrt{\langle \mathcal{M}^2 \rangle} \approx \Gamma$  and the zero temperature equals  $\sigma_{xx}(T \rightarrow 0) \approx \frac{e^2}{\pi h} \approx 0.318 e^2/h$ . This result agrees well with the data under the given approximations. Moreover, in equation (3.12) the

quadratic temperature dependence for  $k_B T \ll \Gamma$  has been calculated in accordance with the measurement, while for  $k_B T \geq \Gamma$  the dependence turns out to become linear (3.13).

Since these calculations are based on the Dirac model in the system and reflect the actual measurements, this agreement is additional evidence for the Dirac fermion physics inherent to HgTe quantum wells.

In summary, the existence of massless Dirac fermions in HgTe has been proven by several approaches. The HgTe quantum well is the first high electron mobility 2DEG which exhibits a linear band structure, providing one single valley. Therefore, Dirac transport theories derived during the rise of graphene and depending on single valley transport can now be investigated.

One example is the carrier concentration dependent mobility in this Dirac system. Typically, the mobility increases in regular 2DEGs due to increased screening of impurity potentials. In several HgTe quantum wells, however, a distinct peak in the mobility has been observed. These experiments on QWs with various  $\mathcal{M}$  could be described by a transport theory based on the effective model [TTP<sup>+</sup>11] and matches the experimental results.

It was noticed during low temperature measurements that a conspicuously stable, negative magnetoconductance occurs for narrow channels. The detailed experimental investigation of this effect is described in the last section.

### 3.3 Weak Anti-Localization Effect in HgTe Nanostructures

In chapter 2.2.2 the motion of electrons in a disordered system was described classically by the Drude model. It is based on non interacting electrons which are accelerated in an electric field  $\mathbf{E}$  and undergo collisions after an average time  $\tau$ . This leads to the Drude conductivity:

$$\sigma_0 = ne^2 \frac{\tau}{m_e} \quad (3.14)$$

Obviously, in this basic approach, the conductivity does not depend on the magnetic field. Moreover it was shown that the formation of Landau levels lead to Shubnikov de-Haas oscillations for high magnetic fields. For low magnetic fields, however, the conductivity remains unaffected.

But, as pointed out in the previous section, HgTe exhibits significant deviations from the regular parabolic energy dispersion on which the Drude model is based. Therefore investigations of the electronic transport in quasi 1D nanowires have been carried out and a very stable weak anti-localization peak has been found. The detailed results on various samples will be shown in the following sections.

#### 3.3.1 One-Dimensional Conductance

Starting with a sample fabricated for micro-Hall magnetometry, the longitudinal resistance of sample HWAL1.1 was measured. The corresponding sample design used to study transport in 1D channels is shown in fig. 3.12a. During the cool down of the sample in the cryostat a constant voltage of  $10\text{ mV}$  was applied via contacts 2 and 6 giving rise to a current  $I$ . The longitudinal voltage drop  $V_x$  was measured in a four-point configuration via contacts 3 and 4 in order to rule out contact resistances. Simultaneously, the driven current was measured by a reference resistor. Thus the longitudinal conductance is given by  $G = I/V_x$ .



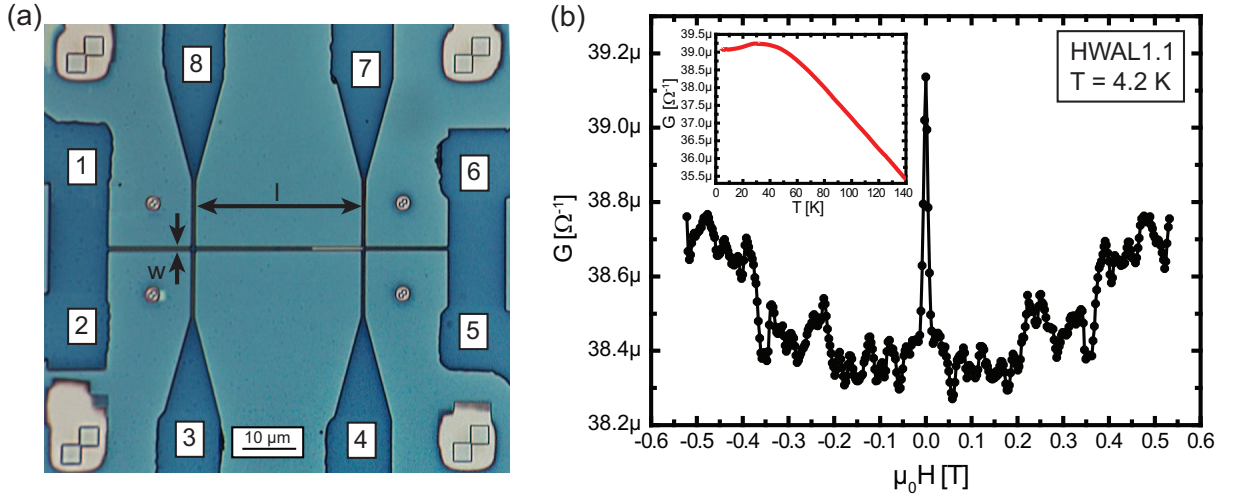


**Fig. 3.12:** Investigation of longitudinal conductance of quasi one-dimensional transport on HWAL1.1 (a) Micrograph of investigated sample with nominal dimensions  $(0.30 \cdot 30) \mu\text{m}^2$  (width  $w$  and length  $l$ , respectively) (b) Magnetoconductance at 4.2 K; inset: cool-down curve.

The cool down curve depicted in the inset of fig. 3.12b exhibits an increasing conductance for lower temperatures which can be attributed to decreasing electron-phonon interactions. Due to the modulation doping in the HgTe heterostructure, scattering at impurities is supposed to be negligible. Remarkably, the curve is non-monotonous for temperatures below 40 K. It is known that arising conductance corrections are due to an increased phase coherence length in high electron mobility systems at such low temperatures [BvH91]. This gives rise to interference effects which are strongly affected by magnetic fields. The conductance of HWAL1.1 depending on low magnetic fields is shown in fig. 3.12b. The dominant feature in the measurement is a pronounced peak around zero field. For nonzero fields, the conductance follows a parabolic behavior and features oscillations.

### 3.3.2 Parabolic Background

The classical magnetoresistance originating from Lorentz force is neglected by the Drude model. This approximation is correct as long as the elastic scattering time  $\tau$  is small. However, this does not remain valid for low temperatures and high mobility systems. According to Kohler's rule the arising magnetoresistance exhibits a parabolic dependency

on a magnetic field [Zim79]:

$$\frac{\Delta\rho}{\rho_0} \propto (\tau_e B)^2 \quad (3.15)$$

Phenomenologically, it is understood that the Lorentz force deviates the trajectories of electrons to circular paths thus effectively decreasing the mean free path of the carriers. The resistance increases with higher magnetic fields - it is a negative magnetoconductance effect. However, in the measurement we find a positive magnetoconductance which cannot be attributed to Lorentz magnetoresistance.

Furthermore, the Coulomb interaction between two conductance electrons gives rise to another conductance correction and is called electron-electron interaction. An intuitive interpretation has been given by Bergmann [Ber87]. He understood the interaction between the electrons as a diffraction of one electron in the electrostatic potential of the other. The deviation in the motion of the electron gives rise to a correction in the conductivity. It follows a temperature dependence as:

$$\delta\sigma_{ee} \propto \ln(T) \quad (3.16)$$

Intuitively, the decrease of this correction is due to electron-phonon scattering at higher temperatures which overcomes the electron-electron interaction. In magnetic fields, the electron-electron interaction was experimentally found (in agreement with theory) to show a temperature dependent positive parabolic magnetoconductance [PTH83, CTP86]:

$$\delta\sigma_{xx} \propto \delta\sigma_{ee}(T)B^2 \quad (3.17)$$

where the parabolic part is supplied by the classical result and the temperature dependency by the e-e conductivity correction. Due to that the nonzero field signal on HWAL1.1 was measured in temperature-dependent mode (see fig. 3.13a). Here, the peak was cut out for clarity. Opposing to (3.17) the curvature was constant throughout the investigated

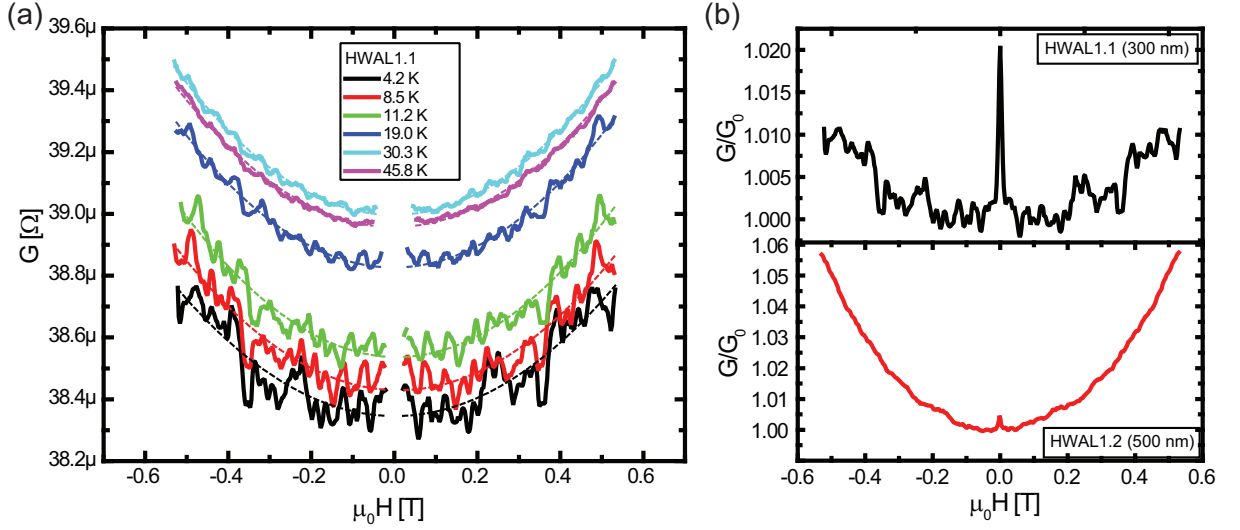


**Fig. 3.13:** (a) Longitudinal conductance of HWAL1.1 in varied magnetic field at several temperatures (peak was cut for clarity) (b) Normalized conductance of 300 and 500 nm wide channels at  $T = 4.2 K$ .

temperature range. In other words,  $\sigma_{ee}$  did not depend strongly on the temperature in this case.

Furthermore HWAL1.2 was fabricated - a second sample of the same substrate. The nominal dimension of this narrow channel had a width of 500 nm and a length of 30  $\mu m$  (compared to 300 nm and 30  $\mu m$  for HWAL1.1). Normalizing the conductance by the zero field conductance  $G/G_0$  ( $G_0$  taken from the offset of the parabolic fit), a comparison between the channels of two different widths is carried out in fig. 3.13b. Similar to the experimental results of Choi et al. on GaAs/(Al,Ga)As heterostructures [CTP86], the parabolic magnetoconductance is less pronounced for narrower channels than for wider ones (1.2 % versus 6 % at 0.5 T). In addition, the oscillations are considerably smaller.

The focus in the following, though, is set on the remarkable peak. The investigation of the temperature independent electron-electron interaction in this material is an interesting subject for further research.

Yet, in further plots, the parabolic background has often been subtracted in order to facilitate a quantitative analysis of the remaining features of the magnetoconductance. This is designated by the term  $\delta G$  and  $\delta\sigma_{xx}$  for conductance and conductivity, respectively.

### 3.3.3 Universal Conductance Fluctuations

The remarkably regular oscillations observed in fig. 3.12b appear for low fields and cannot be explained by earlier introduced ballistic effects or Shubnikov-de Haas oscillations. Instead, universal conductance fluctuations (UCF) - an effect based on the wave property of electrons - could be the origin of the observed oscillations.

When an electron wave propagates through a structure, it is scattered elastically at numerous impurities without losing its phase. Doing so, the electron as a wave experiences the entire sample width on its way along the channel.

An intuitive analogy of the electron wave in disordered conductors is the scattering of coherent monochromatic light inside disordered materials. Every scatterer is the source of a spherical wave (Huygens' principle) and the combination leads to a complicated superposition pattern. It is obvious that the change of only one scatterer will lead to a different superposition pattern. Thus this effect will change the probability of transmission and reflection of the monochromatic light. In the case of electrons, this effect changes the conductance.

For transport at low temperatures, the phase coherence length  $l_\phi$  can be much larger than the elastic scattering length  $l_e$ . When this conditions holds, fluctuations in conductance occur as soon as the Fermi vector  $k_F$  (thus the wavelength of the carriers) changes. This can be achieved by magnetic fields  $B$  and/or variations of the chemical potential  $\mu$ . The magnitude of these fluctuations were found to exhibit the universal constant  $e^2/h$  [Al85] - independent on the sample geometry - as long as the inelastic scattering length  $l_{in}$  is larger than any dimension of the sample. These fluctuations have been theoretically described by the Al'tshuler-Lee-Stone theory [Al85, LS85] using the diagrammatic technique. Lee [Lee86] later gave a heuristic argument using the Landauer-Büttiker ansatz. It is important to understand that the conductivity  $G(\mu, B)$  is not a time-dependent noise but a fluctuating function of its arguments for specific impurity configurations.

If measuring many samples with identical sample geometry and exactly the same physical properties, but different impurity configurations, every sample will exhibit a different conductivity due to UCF. However, when calculating the mean value over all

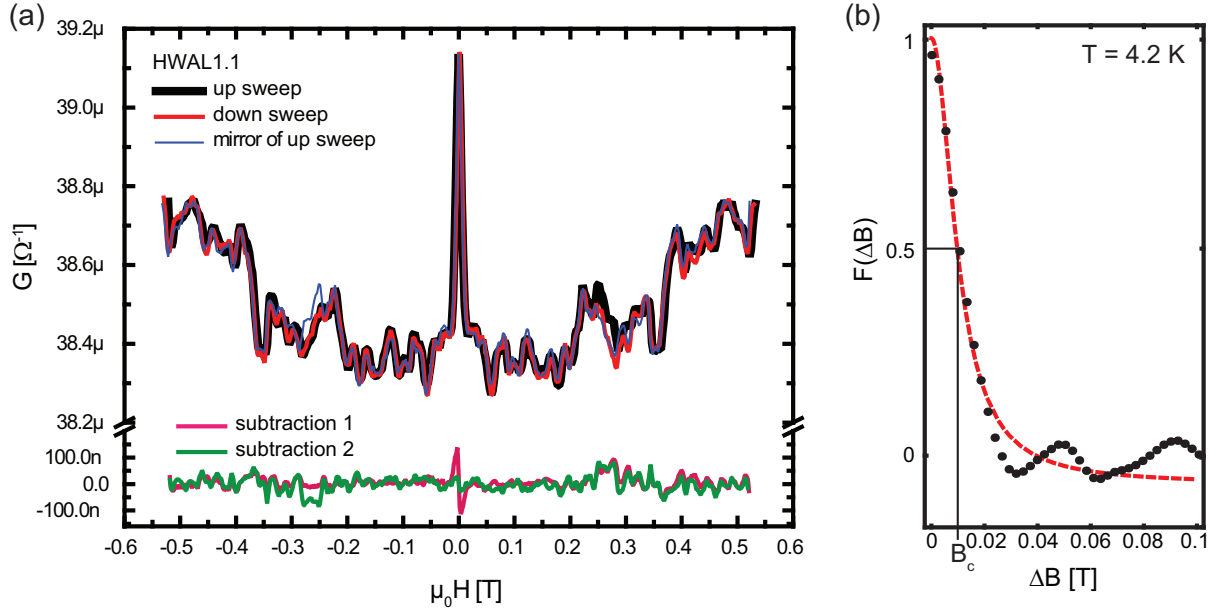


**Fig. 3.14:** (a) Longitudinal conductance of sample HWAL1.1; curves belong to an up sweep (black) and down sweep (red) of the magnetic field, the blue curve is a mirror of the up sweep in respect to  $B = 0 T$ . Subtraction of the curves are depicted below the break, (pink) up minus down sweep, (green) mirror of up sweep minus up sweep (b) Autocorrelation function for  $T = 4.2 K$  with correlation field  $B_c$ .

conductivities, the UCF will be averaged out because it is a statistical effect.

A more convenient way to investigate the UCF (compared to the fabrication of many identical samples) is to apply a magnetic field or a gate voltage, thus changing the superposition pattern on the same sample.

In case the width of the sample is much smaller than the phase coherence length  $l_\phi$  the result of Lee and Stone for the RMS of the UCF is given by

$$\delta G \equiv [Var(G)]^{\frac{1}{2}} = const \times \frac{e^2}{h} \left( \frac{l_\phi}{L} \right) \quad (3.18)$$

where  $e$  is the electron charge and  $L$  is the length of the system. UCF therefore originate from the phase coherence length of the electrons and should, in principle, be called a superposition rather than an interference effect.

In order to determine whether the measured oscillations are in fact UCF peculiar characteristics were tested.

Since UCF are not a time-dependent effect, measurements in perpendicular magnetic field must be reproducible due to stable impurity configurations. Moreover, UCF exhibit time reversal symmetry. Thus, changing the direction of current and/or inverting the sign of the applied magnetic field should not change signal due to UCF.

In fig. 3.14 the black and red curve correspond to two different measurements. The subtraction of the two measurements is drawn in the lower half by the pink curve. Apparently, the subtraction curve is almost zero in the limits of the error bars. The only significant difference existing around zero magnetic field is attributed to the hysteresis of the magnet because the measurements correspond to an up and down sweep of the magnetic field, respectively. For proving time reversal symmetry the black curve has also been mirrored at the zero field axis and results in the blue curve. Again, the subtraction (green curve) is nearly zero with a slight deviation for  $-0.3 T$ . This is presumably due to slight fluctuations in the measurement setup since the curve recovers the initial progression after that.

UCF have been found to be a tool to determine the phase coherence length [LSF87]. For 1D transport Beenakker and van Houten [BVH88] calculated the dependence of the correlation field  $B_c$  to the phase coherence length. The correlation field can be extracted by analysis of the autocorrelation function  $F(\Delta B) = \langle \delta G(B) \cdot \delta G(B + \Delta B) \rangle$  where  $\Delta B$  is the displacement parameter in the magnetic field. Evaluating  $F(\Delta B)$  for a range of displacements typically leads to a peak around  $\Delta B = 0$  for correlated systems. In case of white noise this peak is absent.

$B_c$  is determined by the half width at half height  $F(\Delta B_c) = 1/2 F(0)$ . Intuitively, this is the field needed to break the correlation between electron paths. The correlation function of sample HWAL1.1 at  $T = 4.2 K$  is displayed in fig. 3.14b alongside the evaluation of the correlation field  $B_c$ . From this data, using the formula derived by Beenakker [BVH88], the phase coherence length  $l_\phi$  is calculated to be  $> 1 \mu m$ . However, an enhancement of UCF in 2DEGs with Dirac-like band structure has been predicted by theory [RTB07]. That is why corrections to the used expression might be necessary to describe this system correctly.

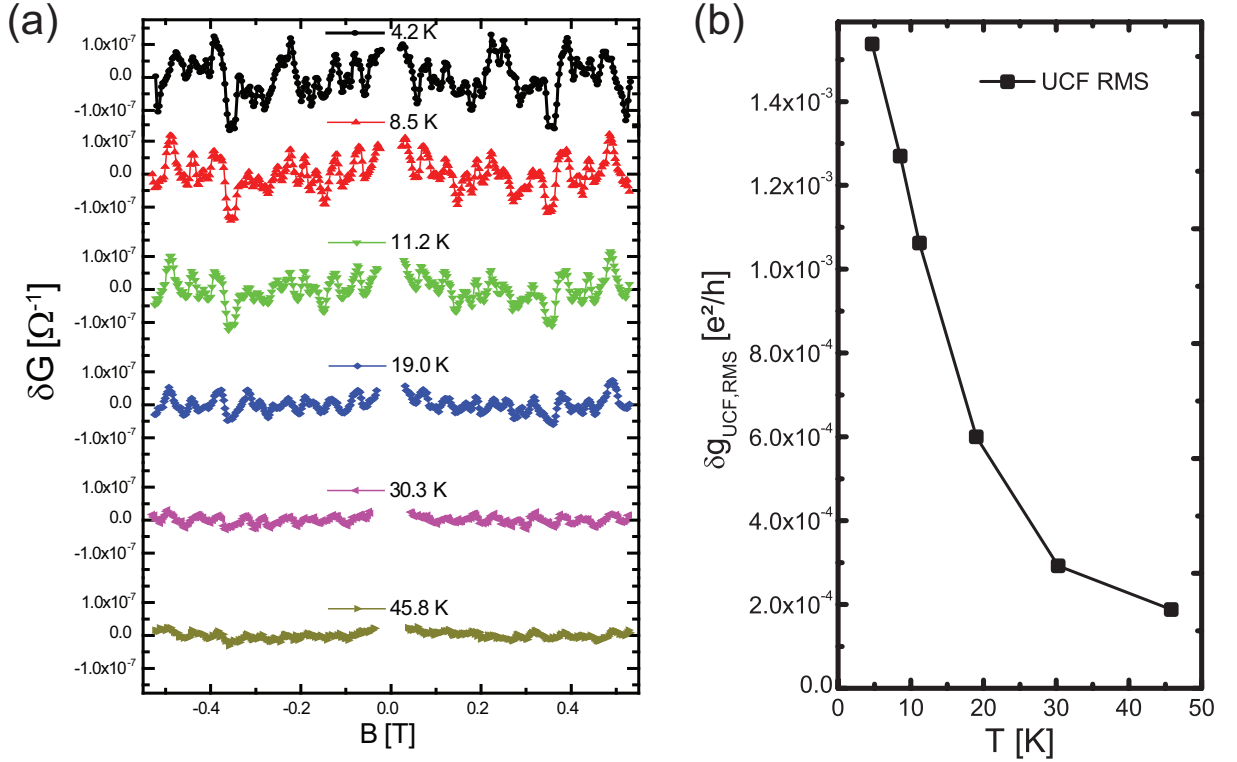


**Fig. 3.15:** Temperature dependent UCF on HWAL1.1 (a) Conductivity measurements for several temperatures; (b) Evaluated RMS of the conductivity depending on temperature.

In addition, UCF depend on the width of the 1D channel due to self-averaging effects. This is proven for the HgTe QW in fig. 3.13b, where the oscillations are pronounced for the 300 nm wide channel and barely visible for the 500 nm wide one (both fabricated from the same substrate). In conclusion, the observed oscillations show the characteristic properties of universal conductance fluctuations.

As mentioned before, keeping the phase information is crucial for UCF. Inelastic scattering due to e.g. electron-phonon scattering at increasing temperatures decreases the phase coherence length  $l_\Phi$ . The amplitude of UCF therefore follows the temperature dependence of the phase coherence length. In fig. 3.15a conductivity measurements for a temperature range from 4.2 K to 45 K are shown. Remarkably, features of the UCF remain visible for temperatures as high as 45 K. The temperature dependence of the root-mean-square of the UCF is depicted in fig. 3.15b.

The last feature of magnetoconductance in narrow HgTe channels is the peak around

zero magnetic field - omitted so far in the graphs. The breakdown of conductance corrections due small magnetic fields is usually due to lifting of the time reversal symmetry. The theory of localization predicts this behavior. The next section will give a phenomenological introduction into localization phenomena in order to summarize the basic dependencies to physical factors.

### 3.3.4 Localization

The so called localization of electrons in metals and semiconductors is based on the interference of time reversal pairs of coherent electron waves which are backscattered to their origin. The scattering occurs at crystal defects, at the boundary of the sample, or in the presence of impurities, and is quasi elastic. The interference happens to a single electron which undergoes several paths to the next scattering point. Therefore it is not a many particle effect.

The obvious requirement for weak localization is that the phase coherence time  $\tau_\phi$  must be larger than the elastic scattering time  $\tau_e$ . Typically, this condition is only fulfilled for very low temperatures.

Weak localization was first described in a diagrammatic perturbation theory by Anderson et al. and Gorkov et al. [ATAF80, GLK79]. More intuitively, the description by Bergmann [Ber84] interprets the localization phenomenon as coherent backscattering. Here, the interference of classical trajectories (or "Feynman paths") from one point to another are understood as the reason for localization. The sketch in fig. 3.16 shows exemplary paths of an electron traveling from point A to point B. Obviously, the electron can take various paths. In the figure, the circles are elastic scattering centers which are hit in average after the elastic scattering time  $\tau_e$ .

The electron moving from A to B experiences several scattering events. But because the scattering is elastic, the electron wave does not lose its phase information. Apparently, the wave picture of electrons only holds true for this motion, when the phase coherence length is longer than the distance from A to B. Due to the theory of Feynman paths every path  $j$  can be described by a complex amplitude  $A_j$ :



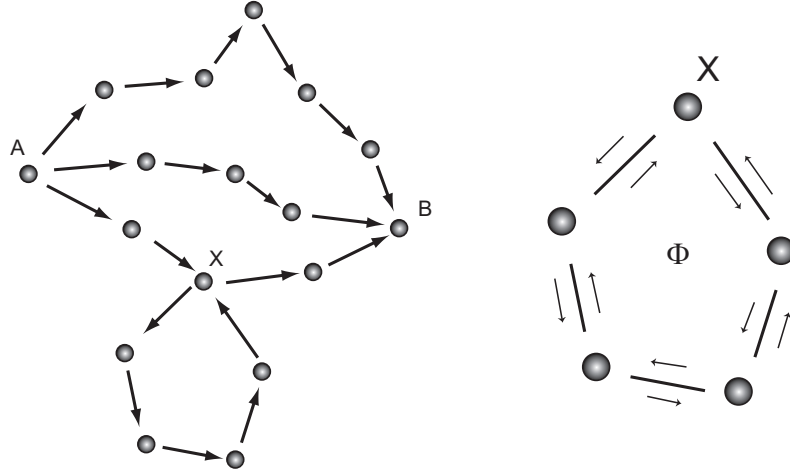


**Fig. 3.16:** Various electron paths from point A to point B with one path exhibiting a self crossing point X.

$$A_j = C_j e^{i\phi_j} \quad (3.19)$$

$\phi_j$  describes the phase shift the electron gains when moving from A to B. The overall probability  $P_{AB}$  for the electron moving from A to B is the sum of complex amplitudes  $A_j$  squared. The sum runs over all available trajectories from A to B.

$$P_{AB} = |A_j|^2 = \left| \sum_j C_j e^{i\phi_j} \right|^2 = \sum_j |C_j|^2 + \sum_{j \neq k} C_j C_k^* e^{i(\phi_j - \phi_k)} \quad (3.20)$$

The first term on the right-hand side of (3.20) corresponds to the classical trajectories and leads to the classical diffusion probability. The second term is responsible for quantum interference. The number of paths contributing to the sum is huge. Therefore, in most cases, the interference term equals to zero since all phases average out - they are uncorrelated. However, this statement only holds true for non-self crossing paths. This is merely a path where the start and end point is the same (as point X in fig. 3.16) - one could say, the electron is backscattered to its initial point. In that case the interference term does not average out and contributes to the overall amplitude  $P_{AB}$ . All self-crossing paths can be summed up in pairs for clockwise and counter-clockwise propagation along the self-crossing path. The expression for these trajectories in complex amplitudes is then

$A_{1,2} = C_{1,2}\exp(i\phi_{1,2})$ . When these pairs follow time-reversal invariance, the amplitudes  $C_1 = C_2 = C$  and the phases  $\phi_1 = \phi_2 = \phi$ . For the probability amplitude then follows:

$$P_{XX} = |A_1 + A_2|^2 = |C_1|^2 + |C_2|^2 + 2\text{Re}[C_1 e^{i\phi_1} C_2^* e^{-i\phi_2}] = 4|C|^2 \quad (3.21)$$

The probability for the electron to return to point X therefore is - compared to the classical results  $2|C|^2$  - twice as high. This constructive interference decreases the probability for an electron to propagate from point A to point B, leading to a decrease in conductivity. This is the main statement of weak localization.

Weak localization occurs in normal high mobility semiconductors (e.g. GaAs/AlGaAs 2DEG). In these systems with free spin, the phase gathered in clock- and counterclockwise propagation is the same. One says, the spin rotation symmetry is preserved. However, when the spin is locked to the moment  $\mathbf{k}$ , the two paths gain opposite phases on their ways and the spin rotation symmetry is broken.

Hikami and Larkin [HLN80] were the first to describe localization in this regime. The not-conservation of electron spin leads to an opposite effect in the localization theory - the weak anti-localization. This phenomenon has also been later discussed by Bergmann et al. [Ber82] for metallic samples. A fundamental consequence of quantum theory is that spin 1/2 particles must undergo a  $4\pi$  rotation in order to recover its initial state. In weak localization theory no phase difference is gathered by clockwise and anti-clockwise propagation of the waves, giving rise to a constructive interference. However, in case of weak anti-localization, the phase difference gathered on the two trajectories is  $2\pi$  leading to a destructive interference of the electron waves. Thus the backscattering to point X is decreased.

In consequence, the classical result of the probability amplitude  $P_{XX} = 2C$  is reduced by the interference term leading to a suppression of backscattering and thus to a higher conductivity (hence the name "anti"-localization).

The dominant mechanism for locking the spin to the motion is due to spin-orbit interaction (SOI). The two contributions to SOI are the Rashba and Dresselhaus terms. They come into existence due to inversion asymmetry, specifically structure inversion asymme-

try SIA (Rashba) and bulk inversion asymmetry BIA (Dresselhaus). In heterostructures the SIA can be very large. Here, an electrical field perpendicular to the plane naturally arises due to a gradient in the potential. The spin state of an electron moving perpendicular to this electric field is affected, acts as an external magnetic field, and leads to a spin splitting in momentum space. The Rashba splitting energy  $\Delta_R$  depends on the electric field which can be tuned by an external gate voltage. The BIA contribution to SOI is due to the asymmetry in the crystal structure, which exists in HgTe that crystallizes in the zinc-blende structure. Its energy splitting  $\Delta_D$  is constant for each crystal.

Hikami et al. [HLN80] derived a formula for WAL depending on these factors which allow for the correct calculation of such localization effects.

But only recently, Suzuura and Ando [SA02] predicted that a Dirac-like band structure exhibits its own mechanism of breaking spin rotation symmetry. This is due to the fact that spin and momentum vector are also locked - similar to the case of SOI. Though it turned out in experiments on graphene that this type is very difficult to observe. The reason was found to be the intervalley scattering between the two inequivalent Dirac valleys which exist in graphene.

In contrast, HgTe exhibits only one valley, making intervalley scattering impossible and thus allowing for the investigation of interference effects for Dirac fermions. Additionally, HgTe exhibits another factor that might influence localization effects, the Dirac mass  $\mathcal{M}$ . As mentioned before, the Dirac mass can be tuned by the thickness of the quantum well from negative, over zero, to positive.

Examining self-crossing paths in the presence of a magnetic field  $\mathbf{B}$  with its vector potential  $\mathbf{A}$  the two paths clock- and counterclockwise along the paths gain a phase difference  $\Delta\phi$ . The two amplitudes change into:

$$C_{1,2} \rightarrow C_{1,2} \exp\left[\left(\frac{ie}{\hbar} \oint \mathbf{A} d\mathbf{l}\right)\right] = C_{1,2} \left(\pm i \frac{2\pi\Phi}{\Phi_0}\right) \quad (3.22)$$

With  $\Phi$  being the magnetic flux through the area  $A$  of the selfcrossing path and  $\Phi_0 = \frac{h}{e}$  the magnetic flux quantum. The phase difference between the two time-reversed paths equals

$$\Delta\phi = 2\frac{2\pi\Phi}{\Phi_0} = \frac{2A}{l_m^2} \quad (3.23)$$

$$l_m = \sqrt{\frac{\hbar}{eB}} \quad (3.24)$$

where  $l_m$  is the so-called magnetic length. As (3.24) describes, the phase difference rises for increasing magnetic fields. Therefore the probability for constructive/destructive interference at point X decreases for increasing magnetic fields. For even higher fields, the correction due to localization becomes negligible and the conductivity approaches Drude conductivity.

Localization effects can be assessed experimentally by applying a magnetic field perpendicular to the sample thus breaking time reversal symmetry. The following subsections investigate the behavior of the conductivity correction, depending on

- temperature,
- Fermi energy,
- SOI strength and
- Dirac mass.

For this purpose, several samples were fabricated (shown in table 3.1).

name	top doping	nominal $d_{QW}[nm]$	bottom doping
HWAL1.1	X	8.0	X
HWAL1.2	X	8.0	X
HWAL2	X	6.5	X
HWAL3	X	8.0	
HWAL4		7.0	X
HWAL5	X	5.0	

**Tab. 3.1:** Samples used for WAL investigations; symmetrical and asymmetrical QWs with varying nominal  $d_{QW}$  (growth process parameter); real  $d_{QW}$  of HWAL2 presumably  $> d_c$ .

### 3.3.4.1 Experimental Analysis of WAL measurements

In experiments, usually, the resistance  $R$  and the change in resistance  $\delta R$  is attained. In theory, on the contrary, the conductivity change  $\delta\sigma$  is derived. The latter is independent on geometry and therefore is the favorable parameter for analysis. Starting from experiment, the conductance and resistance are typically normalized to a square unit cell resulting in  $\sigma_{xx}$  and  $\rho_{xx}$  (for low magnetic field applies  $\sigma_{xx} = \frac{1}{\rho_{xx}}$ , because  $\rho_{xy} \ll \rho_{xx}$ ). This allows for comparison of samples with different dimensions. It must be noted that this perspective is only correct for geometrical phase effects such as localization. For statistical effects (e.g. UCF), the determination of the conductivity leads to false results. This is obvious because UCF exhibit the universal value of  $e^2/h$  in case the dimensions are smaller than  $l_\Phi$ . Thus, for two samples with a length  $l_1, l_2 < l_\Phi$  the UCF exhibit the same conductance amplitude of  $e^2/h$  whereas the amplitude in conductivity would differ.

The transformation between the conductance and resistance change, though straightforward to calculate, is not intuitive on first sight and shall be carried out as follows:

$$G_{xx} = \frac{1}{R_{xx}} \quad (3.25)$$

$$\sigma_{xx} = \frac{1}{\rho_{xx}} = \frac{1}{R_{xx}} \frac{l}{w} \quad (3.26)$$

$$\delta\sigma_{xx} = \sigma_{xx}(B) - \sigma_{xx}(0) = \quad (3.27)$$

$$= \frac{1}{\rho_{xx}(B)} - \frac{1}{\rho_{xx}(0)} = \frac{\rho_{xx}(0) - \rho_{xx}(B)}{\rho_{xx}(0) \cdot \rho_{xx}(B)} \approx \frac{1}{\rho_{xx}(0)^2} \cdot \delta\rho_{xx} \quad (3.28)$$

here,  $w$  and  $l$  are the width and length of the channel. It has been assumed that the resistance change in magnetic field is small compared to the resistance for zero magnetic field  $\rho_{xx}(0)$ . Apparently,  $\delta\sigma_{xx} \neq 1/\delta\rho_{xx}$ . For measurements at an ensemble of  $N$  parallel strips the conductivity equals

$$\sigma_{xx} = \frac{1}{R_{xx}} \cdot \frac{l}{w} \cdot \frac{1}{N} \quad (3.29)$$

### 3.3.4.2 Localization and Temperature

In this section the WAL peak is investigated in respect to the temperature dependence. Since the localization relies on the same critical length scale as UCF ( $l_\Phi$ ), the conductivity correction could persist in similar high temperatures, whereas the analysis of localization effects usually asks for cooling to mK in a dilution refrigerator. In fig. 3.17a  $\delta\sigma_{xx}$  is plotted in terms of conductance quanta. The assumption is confirmed. The WAL peak persists to remarkable 45 K. Obviously, the Dirac-like band structure again gives rise to special transport properties, as predicted by [SA02].

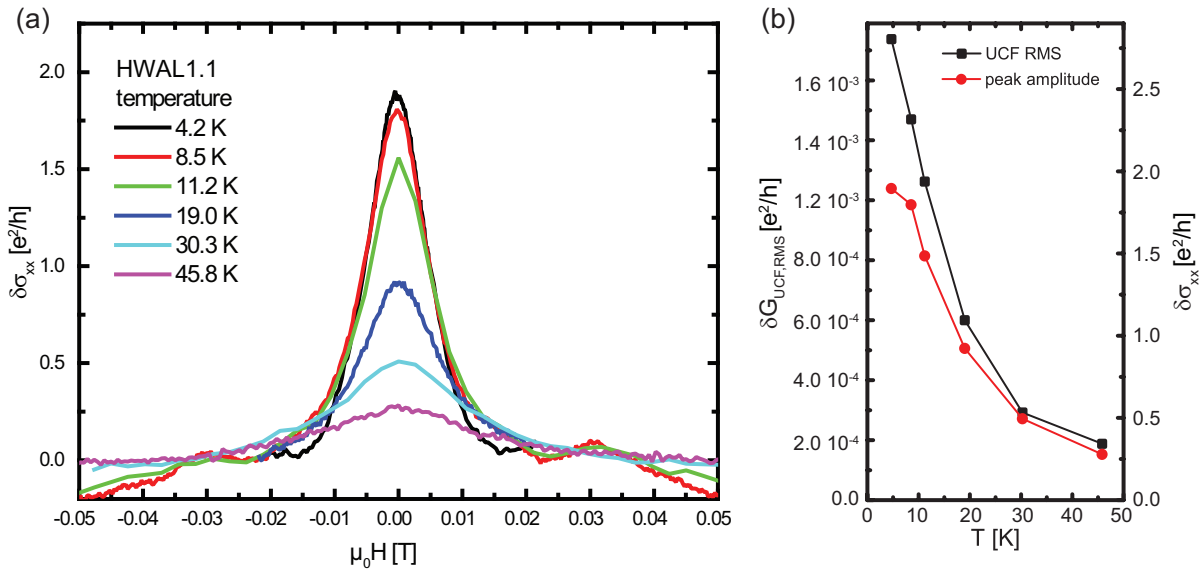


**Fig. 3.17:**  $\delta\sigma_{xx}$  in  $e^2/h$  on HWAL1.1 for various temperatures (a) Magnetic field sweeps (b) Extracted  $\delta\sigma_{xx}$  values compared to the RMS amplitude of the previously analyzed UCF.

The comparison of the UCF root mean square with the peak height shows a similar temperature dependence (fig. 3.17b), and therefore indicates a common critical length scale - the phase coherence length  $l_\Phi$ . It is noteworthy that  $\delta\sigma_{xx}$  seems reach saturation at low temperatures whereas the UCF amplitude is still increasing.

On sample HWAL2 discussed in section 3.3.4.4, the temperature dependence was also determined in a different way. Temperature sweeps for two constant magnetic fields were performed. Special attention needs to be put into very slow temperature changes in order to minimize errors due to different temperatures at the sensor and the sample. The

temperature behavior of this sample is depicted in fig. 3.18.

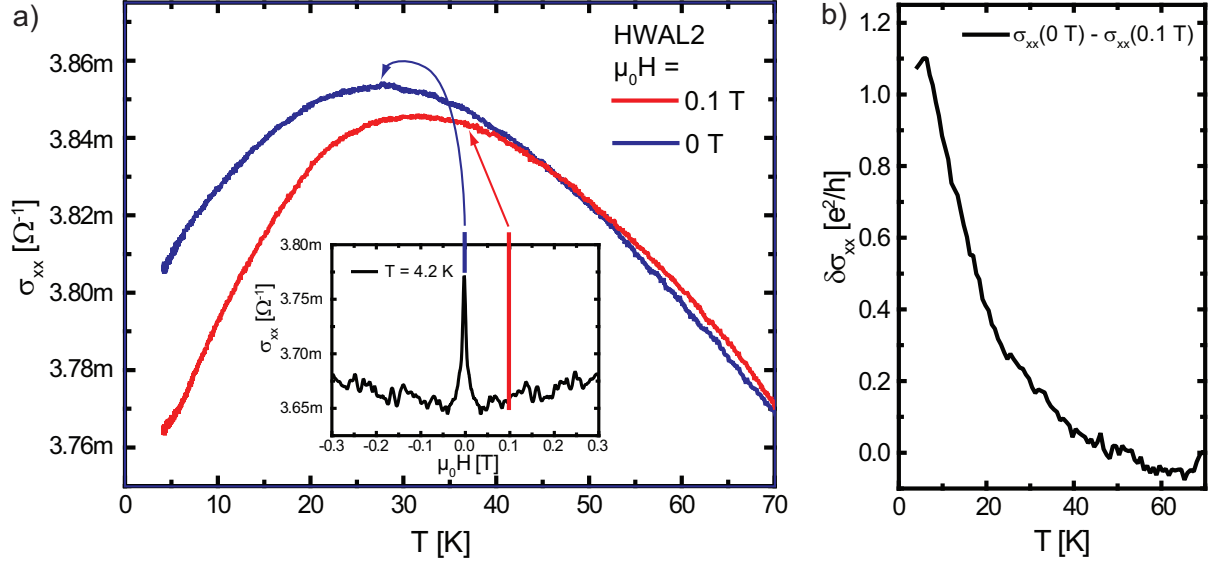


**Fig. 3.18:** Evolution of the weak anti-localization peak for temperature sweeps (a) Conductivity measurement for (blue) 0 and (red) 0.1 T; inset: magnetic field sweep for  $T = 4.2$  K (b) Conductivity correction  $\delta\sigma_{xx}$  obtained from the subtraction of the (blue) and (red) curve from (a).

Sitting on the WAL peak, the blue curve was measured at 0 T. The red curve was taken for broken down spin symmetry at 0.1 T. Thus the difference is a measure for the conductivity correction due to WAL (see fig. 3.18b). As expected, the WAL is stable in temperatures as high as 45 K - similar to the HWAL1.1 (see fig. 3.17b).

### 3.3.4.3 Measurements in In-plane Magnetic Field

So far, measurements observing WAL and UCF in perpendicular magnetic fields have been discussed. By applying the magnetic field in-plane, more information can be obtained and possible bulk effects can be ruled out. If applied in parallel to the plane of the sample, the Lorentz force points in the restricted z-direction and cannot change the electron's trajectory. If the effects depend mainly on the motion and scattering of electrons, an in-plane magnetic field should not change the conductivity at all. On the other hand, when the splitting due to the Zeeman effect plays a role, the conductivity must change. The same is true if bulk properties are present, because the z-direction is then available for transport.

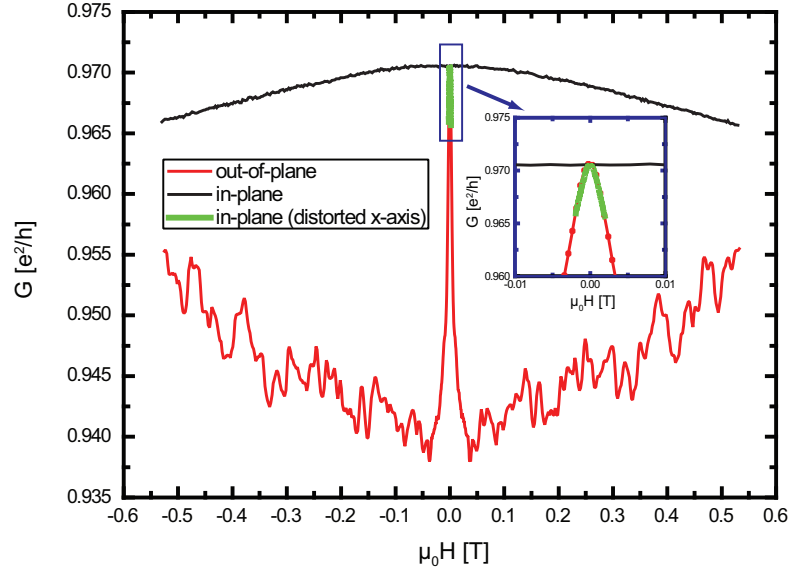


**Fig. 3.19:** Conductance of sample HWAL2 for a magnetic field applied in-plane (black) and out-of-plane (red). (green) corresponds to the in-plane measurement with shrunk x-axis.

In fig. 3.19 the in-plane and out-of-plane measurements on the same sample are depicted. The curves were offset because in the setup used the two configurations cannot be achieved in one cool down. For comparison, the offset of the in-plane curve has been subtracted shifting it to the same value for zero magnetic field. Obviously, the in-plane measurement does not show any sign of WAL nor the existence of UCF. However, it is not constant. But the magnetic field is not necessarily applied perfectly in-plane. So, assuming a tilt of the sample of  $0.2^\circ$ , the applied field exhibits an out-of-plane component as  $B_\perp = B_\parallel \sin(0.2^\circ)$ . The result is an effective "shrinking" of the magnetic field axis and is drawn by the light green curve in the inset of fig. 3.19. It coincides well with the out-of-plane measurement. The small tilt is presumably due to imperfect gluing of the sample into the chip carrier.

#### 3.3.4.4 Localization and Fermi Energy

Sample HWAL2 has been fabricated in order to examine the Fermi wavelength behavior (the process used is the same as for HGM2 in the MHM chapter and is described in table A.4). The geometry has been kept constant with an  $(0.3 \cdot 30) \mu m$  channel. The difference



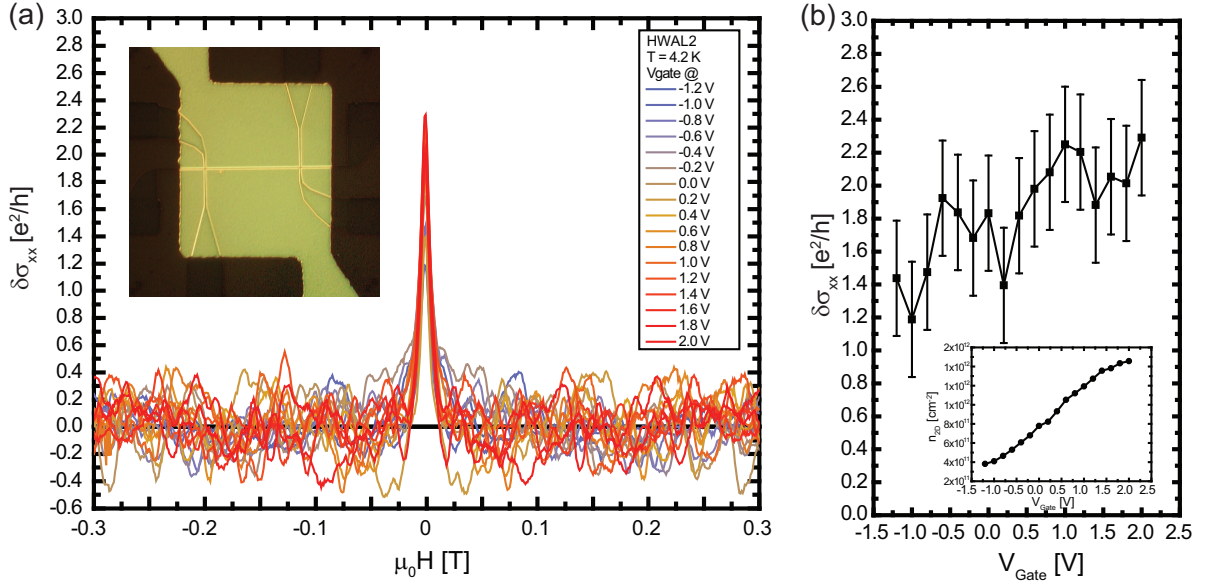


**Fig. 3.20:** Measurements on sample HWAL2 for  $T = 4.2\text{ K}$  (a) Magnetic field sweeps for stepped gate voltage; (inset) Micrograph of top gate with underlying channel (b)  $\delta\sigma_{xx}$  depending on gate voltage (inset) carrier concentration for investigated range of gate voltage.

is the applied gate electrode, facilitating variations in Fermi energy by applying a gate voltage. Moreover, the quantum well was slightly smaller. But this investigation will be dealt with later, when comparing an inverted and normal sample.

The magnetic field behavior mimics the one of sample HWAL1.1, with WAL peak, parabolic background and UCF. Furthermore, for zero gate voltage, the background conductivity was in the same order of magnitude as for the sample without gate.

Examining the sample, first the function of the gate was tested by standard Hall measurements. The carrier concentration calculated by the slope of the  $R_{xy}$ -curve is depicted in the inset of fig. 3.20b. For gate voltages ranging from -1.2 to 2.0 V the carrier concentration  $n_{2D}$  was between  $4.0 \cdot 10^{11}$  to  $1.5 \cdot 10^{12}\text{ cm}^{-2}$ . Measurements were restricted to this range because of starting saturation in  $n_{2D}$ , which is a sign for starting hysteresis effects in gate control [HBS<sup>+</sup>06].  $\delta\sigma_{xx}$  was obtained by fits to a Lorentzian function for each gate voltage (see fig. 3.20a). The extracted peak height is plotted in fig. 3.20b and exhibits an arguable positive linear dependence for increasing gate voltage. However, the UCF led to error bars in the same magnitude as this linear progression. Therefore no

clear conclusion for the dependence on Fermi wavelength can be stated at this point.

As mentioned before, UCF are statistical processes depending on the random impurity configuration. The long channel can be separated into independently oscillating resistors with length  $l_\phi$ . When measuring over a large number of oscillating resistors, the UCF are averaged out. On the contrary, WAL as a geometrical phase effect stays constant.

### 3.3.5 WAL and UCF for an Ensemble on Inverted HgTe QW

One way to average UCF out would be increasing the length of the current channel. However, this is accompanied with an increase of the resistance leading to higher noise in the measurement. A better approach was found in measuring over an ensemble of long parallel 1D channels.

This change in sample layout also inheres a drawback: the Hall voltage cannot be assessed anymore. That is why a small Hall bar has been implemented in order to be able to measure the carrier concentration and mobility on the same sample. The fabrication process is shown in table A.4. Due to proximity effect the dose of the EBL exposure for the ensemble structure was supposed to be adjusted. Though, a dose test showed that the low acceleration voltage of 2.5 kV efficiently suppresses the proximity effect even for these dense structures (see fig. 3.21a).

Fig. 3.21b shows the sample design of HWAL3 with the ensemble of 39 parallel strips each having a width of 370 nm and a length of 38  $\mu\text{m}$ . The fabricated Hall structure was designed with the same width for characterization purposes and is shown in the lower right corner. The SEM pictures were taken at a dummy structure on the wafer which is used to check the process steps. There was no interfering electron bombardment on the measured sample. The top gate covers the ensemble and Hall structure. The carrier concentration and mobility were measured simultaneously with the conductance of the ensemble. Of note, all measurements were performed in an eight-point configuration. That means the current was applied via the ensemble and Hall bar, while simultaneously measuring the conductivity of the ensemble on two extra contacts and the longitudinal and transverse conductivities of the Hall bar. This ensures a consistent characterization

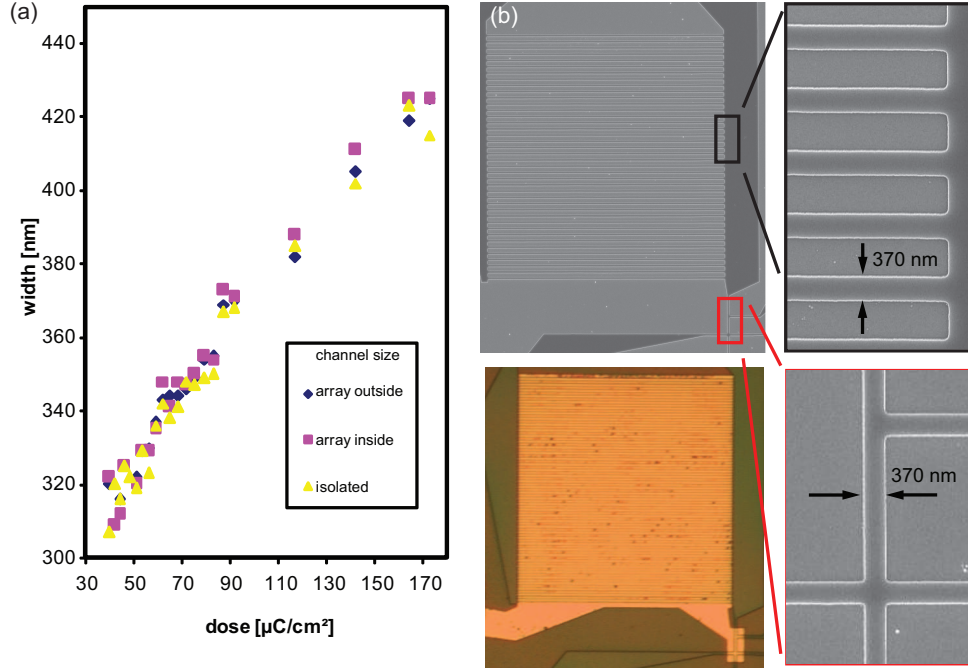


**Fig. 3.21:** (a) Dose test for lines in the middle, outside the ensemble and for an isolated structure (b) SEM pictures of HWAL3 with details of the structure and the applied top gate.

because variances in the fabrication process affect both structures in the same way.

As intended by the design, UCF were averaged out successfully (black curve in fig. 3.22) compared to the longitudinal conductivity on the Hall bar structure (red curve) which exhibits strong UCF. This structure facilitates detailed analysis. The curve of the single channel was offset by  $0.5 \cdot 10^{-3} \Omega^{-1}$  for comparison.

The characterization obtained by the Hall bar shows that temperature has no significant influence on the carrier concentration and mobility of the sample - the curves almost coincide (fig. 3.22b,c). Moreover, applied gate voltages control the carrier concentration linearly in the investigated voltage range.

As a next step, the peak value was quantitatively examined in dependence of temperature and Fermi energy. In fig. 3.23a, temperature dependent measurements of  $\delta\sigma_{xx}$  at constant gate voltage are shown. Using Lorentzian functions for analysis, the height and full width half maximum (FWHM) of the peak have been achieved for 36 magnetic field sweeps, varying temperature and gate voltage. The results are depicted in fig. 3.23b. The peak height exhibits an increase for higher Fermi energies at all temperatures, while the

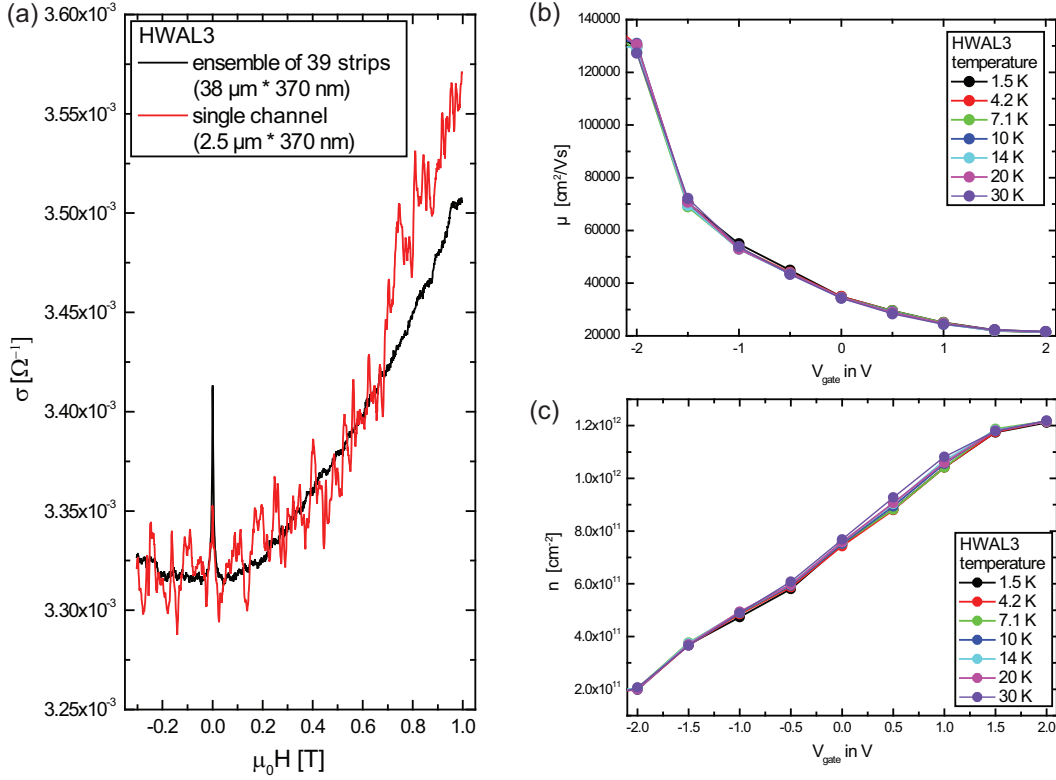


**Fig. 3.22:** (a) Comparison of  $\sigma_{xx}$  for the ensemble and the single channel on sample HWAL3; characterization at the Hall bar structure of (b) mobility and (c) carrier concentration.

FWHM is lowest for high Fermi energies - providing a very distinct peak. For increasing temperature, the progressions stay the same while the absolute value of  $\delta\sigma_{xx}$  decreases and FWHM increases.

The progression of  $\delta\sigma_{xx}$  and FWHM in dependence of temperature are depicted in fig. 3.24 for varied gate voltages. The conductivity correction decreases for all curves similarly. Assuming a function  $\delta\sigma_{xx} = C \cdot T^a$  for the temperature dependence, the factor  $a$  lies in between -0.5 and -0.7. In the case of FWHM the power seems to be between 0.1 and 0.5, again assuming a power law.

The next section deals with the investigation of the role of spin-orbit interaction (SOI) on the weak anti-localization peak in HgTe.

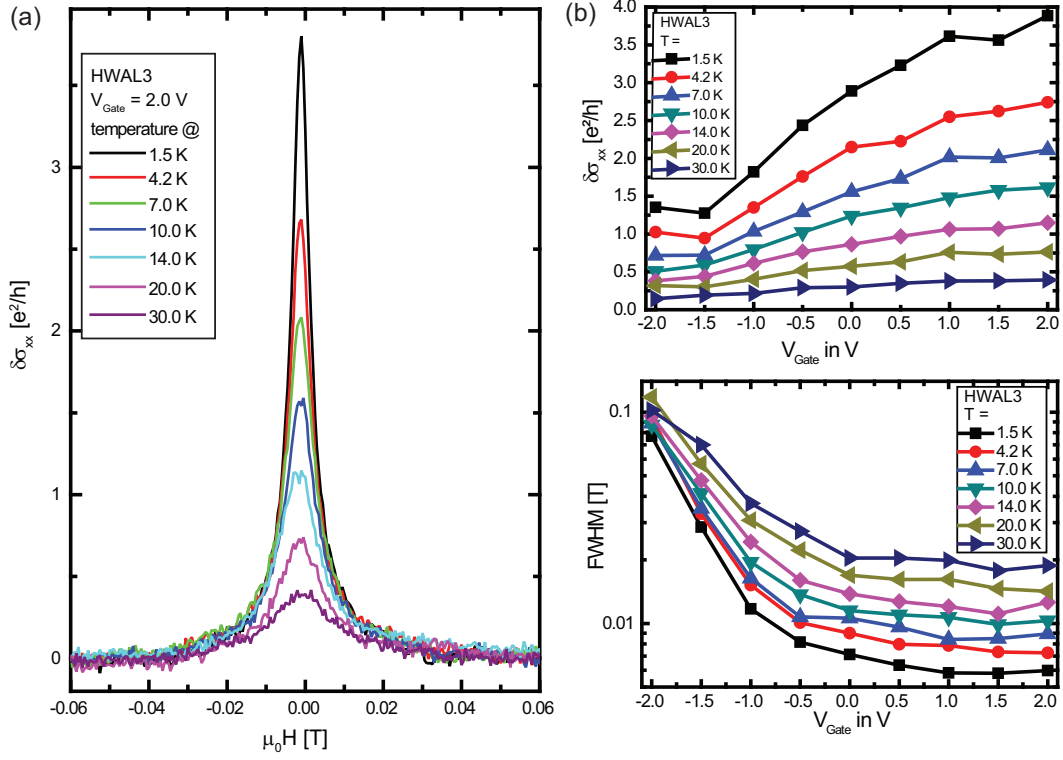


**Fig. 3.23:** Analysis of the WAL peak on sample HWAL3; (a) Exemplary measurements of  $\delta\sigma$  at  $V_{Gate} = 2$  V in magnetic field sweeps for different temperatures. (b) analysis of the peak height and full width half maximum depending on temperature and gate voltage.

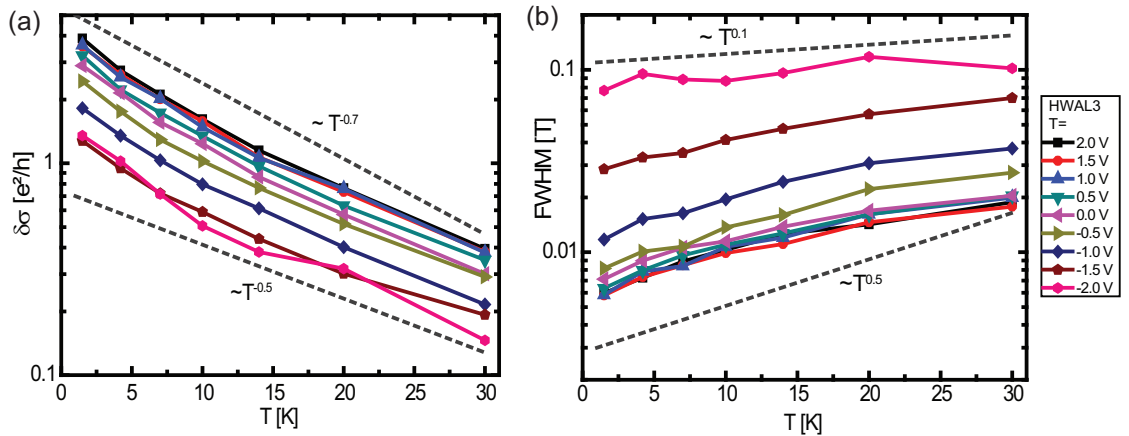


**Fig. 3.24:** Temperature dependence of (a)  $\delta\sigma$  and (b) FWHM for several gate voltages.

### 3.3.6 WAL and UCF for Zero Rashba

As mentioned before, the reason for WAL is the coupling of the spin and the orbital motion of an electron. In heterostructures, electrical fields perpendicular to the plane arise due to potential differences at the interfaces. The caused SOI effect is called the Rashba effect with the spin splitting energy  $\Delta_R$ . Obviously, an externally applied electric field (e.g. gate) tunes the intrinsic field - potentially to zero. In this section the role of Rashba will be investigated. For that purpose a substrate with bottom doping was used. Having iodine as a dopant the accompanied charge is positive. This is crucial because the applied gate voltage not only affects the Rashba strength but also the carrier concentrations. Thus, for top doping, the  $\Delta_R = 0$  case exists for negative gate voltages. This is the regime where the channel is depleted and prohibits electrical measurements. In addition, the experiment should allow for a direct detection of the zero Rashba case. The measurement of Shubnikov-de Haas oscillations have been proven before to be an accurate method to determine the properties of the quantum well including the Rashba SOI strength.

Again, for consistent measurements, the design of the mesa consists of an ensemble structure and a separate Hall bar in the close vicinity. The top gate above the insulator was covering both structures to rule out differences due to slight process variations (see fig. 3.25). The geometry of the Hall bar is  $(10.0 \cdot 30.0) \mu m$  (width and length) - wide

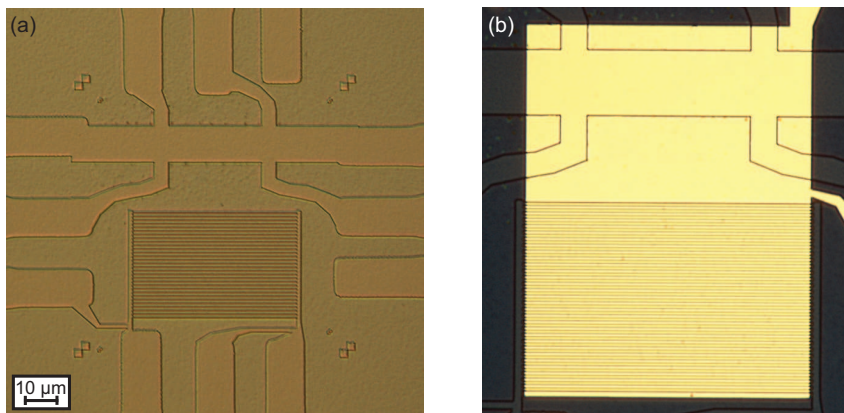


**Fig. 3.25:** Sample design of HWAL4 (a) Etched mesa consisting of ensemble and wide Hall bar (b) Applied insulator and top gate.

enough to prevent edge channel scattering. The ensemble consists of 30 wires with width and length of  $45 \mu\text{m}$  and  $370 \text{nm}$ . Keeping the width constant (crucial parameter as seen in fig. 3.13b) the design of the ensemble was altered to fit the macro-Hall bar inside the lithography field while keeping the number of squares as high as possible.

The following measurements were carried out at  $4.2 \text{K}$ . First, the longitudinal resistance was measured and shows very clear Shubnikov-de Haas oscillations (fig. 3.26a). The Rashba spin-orbit splitting energy  $\Delta_R$  was determined by comparing the SdH oscillations directly with the density of states calculations (derived from the Kane model). The result is depicted in fig. 3.26b.

As intended by the sample design, the Rashba spin orbit strength could be tuned to zero in the conducting region ( $V_{\text{Gate}} = 3.0 \text{V}$ ). The conductivity correction  $\delta\sigma_{xx}$  in magnetic field sweeps shows a WAL peak over the investigated gate voltage range - including the zero Rashba value (fig. 3.26c). The obtained  $\delta\sigma_{xx}$  versus gate voltage is plotted in fig 3.26d. The error bars have been extracted from the RMS of the background. A decrease in  $\delta\sigma_{xx}$  exists, coinciding with the decrease in  $\Delta_R$ . However, the localization phenomena does not vanish for  $\Delta_R = 0$ . Therefore Rashba SOI cannot be the sole cause for the observed effect. Furthermore, the Dresselhaus contribution, stemming from the broken inversion symmetry in the zinc-blende crystal structure, has been determined before to be in the order of  $1 \text{meV}$  [KBMH08]. Thus, since a change of  $\Delta_R$  from  $3 \text{meV}$  to  $0 \text{meV}$  results in a maximum change of  $0.02 e^2/h$  ( $0.09 e^2/h$  to  $0.07 e^2/h$ ), Dresselhaus also can be ruled out as the only cause for this weak anti-localization phenomenon. It must be noted that - compared to sample HWAL3 - the peak height is at least one order of magnitude smaller. These two samples differ by their quantum well width (HWAL3 has a quantum well width of  $8.0 \text{nm}$  and HWAL4  $7.0 \text{nm}$ , respectively).

The samples investigated so far were nominally inverted ( $\mathcal{M} < 0$ ). Thus a sample in the normal regime ( $\mathcal{M} > 0$ ) with otherwise comparable properties shall give insights whether a considerable change in  $\mathcal{M}$  features an impact on the WAL signal.

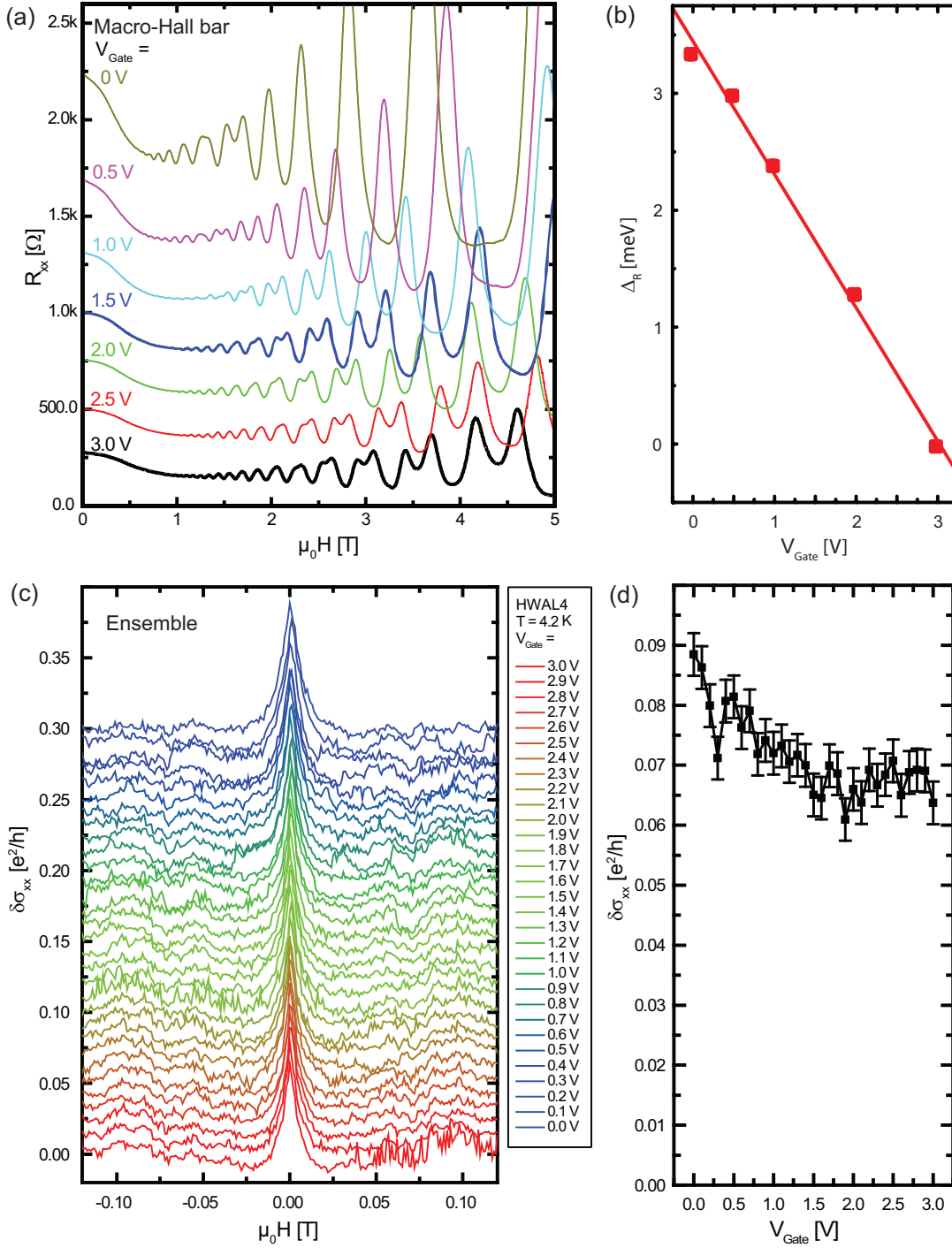


**Fig. 3.26:** Measurements on HWAL4 at 4.2 K (a) SdH-oscillations for several gate voltages (b) Rashba spin-orbit energy splitting  $\Delta_R$  in dependence of gate voltage (c)  $\delta\sigma_{xx}$  of the ensemble in magnetic field sweep (d) Peak height  $\delta\sigma_{xx}(0T)$  with error bars from background RMS.



### 3.3.7 WAL for Normal Quantum Well

After ruling out the typical causes for weak anti-localization, the influence of the Dirac mass  $\mathcal{M}$  will be further investigated.

A HgTe heterostructure with a quantum well  $d_{QW}$  such that  $\mathcal{M} > 0$  was used. The chosen substrate has been extensively examined (see the normal quantum well in fig. 3.6). The comparison of Shubnikov-de Haas oscillations with density of states calculations confirmed a Dirac mass of  $\mathcal{M} = +10 meV$ .

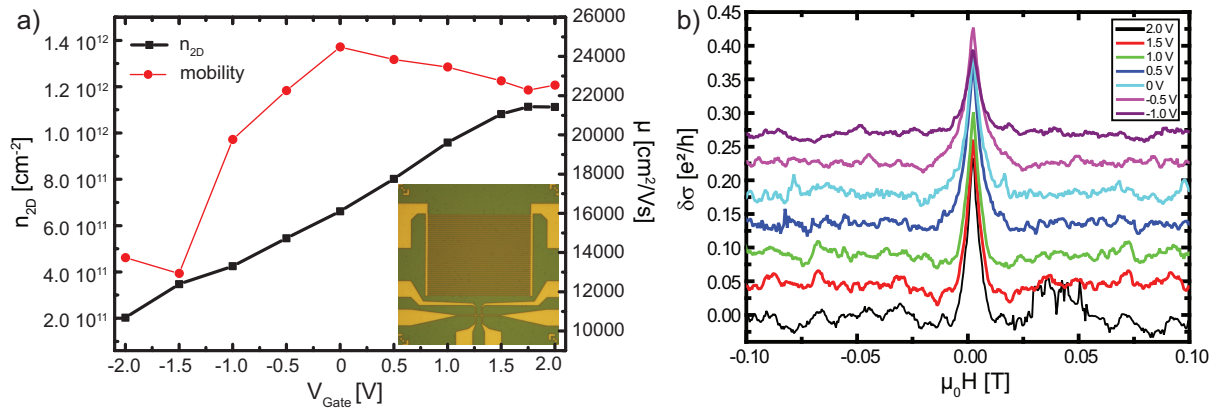


**Fig. 3.27:** (a) Carrier concentration and mobility depending on gate voltage for HWAL5 (inset) micrograph of etched mesa; (b) conductivity correction for magnetic field sweeps.

The sample design is comparable to HWAL3, because the determination of  $\Delta_R$  (as in HWAL4) is not necessary. Instead, the accurate measurement of the mobility and carrier concentration on a Hall bar with the same width is favorable. The sample HWAL5 consists of an ensemble of 39 strips with (width · length) of  $(370 nm \cdot 50 \mu m)$  and a separated Hall bar for characterization purposes (see fig. 3.27a inset). The separation of the two structures was rendered possible due to advances in process development, enabling more contacts on one sample. The carrier concentration and mobility were in the same order of magnitude as the samples before. Therefore, the sample is well suited to investigate the impact of the Dirac mass.

As depicted in fig. 3.27b the measurements of  $\delta\sigma_{xx}$  in magnetic field sweeps also exhibit a WAL peak around  $0 T$ , which is comparable to the conductivity correction in HWAL4 and an order of magnitude lower than HWAL3. A reason for this could be

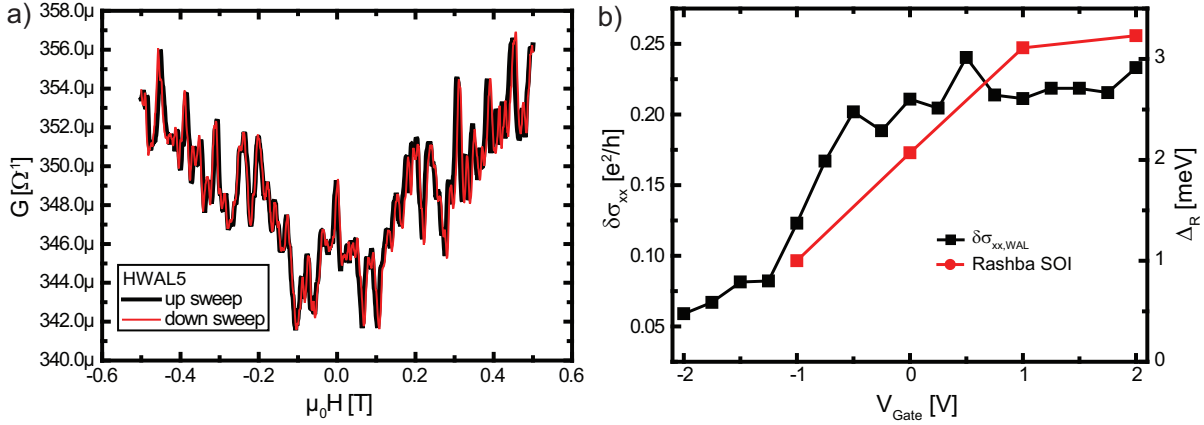


**Fig. 3.28:** (a) Conductance measurement on the Hall bar structure with pronounced UCFs; (b) (black) WAL peak height depending on gate voltage (red) Rashba strength for Q2398, determined on another sample.

dephasing effects in this sample, destroying phase coherence. However, these can be ruled out, because the UCF measured in the longitudinal conductance of the Hall bar (fig. 3.28a) are reproducible in up and down sweeps and are as pronounced as in the HWAL1.1 measured before (fig. 3.14).

By analyzing the magnetic field sweeps, the peak height of HWAL5 depending on gate voltage was determined. The extracted  $\delta\sigma_{xx}$  (black curve in fig. 3.28b) shows an increase for higher gate voltages with a saturation behavior from about  $-0.5$  V on. The maximum peak height of  $\delta\sigma_{xx} = 0.23 e^2/h$ . The Rashba spin orbit strength was determined on the large Hall bar of the same substrate described in section 3.2.3. The result is the red line in fig. 3.28b. Both curves show a similar progression with a saturation for higher gate voltages. The shift in the red curve is explained due to different processing, leading to an effective shift in the gate voltage. Therefore, in this sample, the WAL peak correlates strongly with  $\Delta_R$ .

### 3.3.8 Conclusion

In the last part of this work the weak anti-localization peak existent in HgTe heterostructures has been investigated in temperature dependence and by means of Rashba SOI,

mobility [ $cm^2/Vs$ ]	HWAL3	HWAL5
Macro-HB	$3.63 \cdot 10^5$	$1.30 \cdot 10^5$
Micro-HB	$3.49 \cdot 10^4$	$2.45 \cdot 10^4$

**Tab. 3.2:** Comparison of mobilities for wide and narrow Hall bars of the same material ( $V_G = 0V$ ).

Dresselhaus SOI and Dirac mass  $\mathcal{M}$ . A sample structure which allows for averaging UCF out was found to be crucial for detailed analysis. Simultaneous measurements of Rashba effect and WAL on the same chip showed that neither Rashba nor Dresselhaus terms are the sole cause for the pronounced WAL peak in the inverted HgTe heterostructure HWAL3.

Summarizing the results, the normalized conductivity corrections are drawn in fig. 3.29. Here  $\delta\sigma_{xx}$  is plotted against the carrier concentration. The latter was taken from the Hall slopes on the Hall bars. It must be noted that the width of the Hall bar on HWAL4 differed from the strip width, contrary to the other two samples. It is an important fact that the mobility in narrow samples is reduced compared to wide ones (see table 3.2). The presumable reason for this is scattering at the channel boundaries.

That could also be the explanation, why the WAL peak is hardly observable at 4.2 K

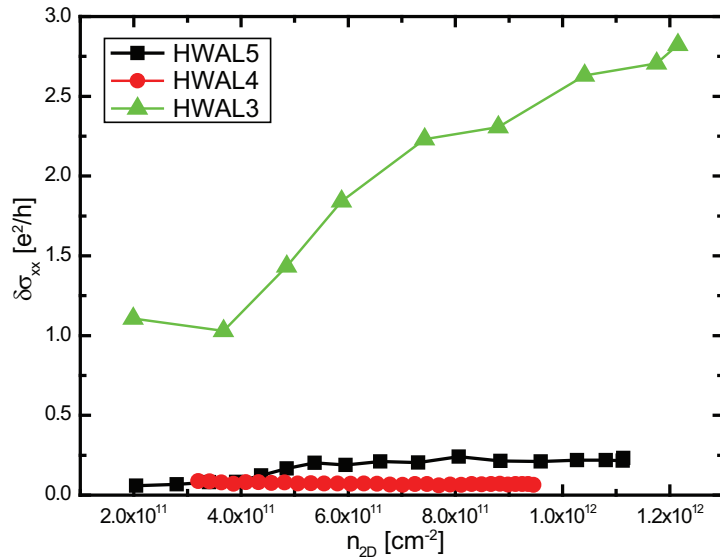


**Fig. 3.29:**  $\delta\sigma_{xx}$  of the WAL peak measured on the ensembles of HWAL3, 4 and 5 in respect to the carrier concentration at  $T = 4.2 K$ .

for macroscopic samples in HgTe. In the case of elastic boundary scattering, the mean free path is reduced while the phase coherence length stays constant. Since  $l_e < l_\Phi$  is crucial for the observation of interference, the smaller width could lead to enhanced interference effects in agreement with the width dependence in fig. 3.13.

Back to fig. 3.29, several conclusions can be drawn. Since all substrates exhibit similar Rashba and Dresselhaus contributions to the spin orbit strength and exhibit very different signal heights, these do not play the dominant role for the WAL effect in HgTe. Especially, HWAL4 with  $\Delta_R \approx 0$  proved this statement. However, the bottom doped sample and the top doped sample follow somewhat the progression of  $\Delta_R$ . But comparing the samples HWAL4 and HWAL5 with the inverted quantum well HWAL3 (which exhibits similar mobilities and carrier concentrations), there is only one conclusion to draw: the main impact factor on WAL in HgTe is the Dirac mass  $\mathcal{M}$ .

Motivated by these experimental results, the Department of Mesoscopic Physics of the University of Würzburg, namely G. Tkachov and E. Hankiewicz, succeeded to develop a theoretical description for the weak anti-localization effect in HgTe quantum wells [TH11]. The results obtained by this theory are consistent with the measurements performed during this work and is based on the Dirac-like band structure with the k-dependent band gap  $E_{Gap}(k) = 2\mathcal{M}_k = 2(\mathcal{M} - \mathcal{B}k^2)$ . Moreover, the theory predicts this particular transport of Dirac fermions in condensed matter for topological insulators.

# Appendix A

## Fabrication Processes

### A.1 Macro-Hall Bar on InAs 2DEG

<b>pretreatment of the MBE-grown samples</b>	
cleaning	60 sec Aceton + 1 min ultrasonic bath
water desorption	rinse in IPA
<b>contacts</b>	
AR300-80	spincoating: 40 sec at 5000 rpm hotplate: 2 min at 120 °C 1 min cool down
AR-U4040	spincoating: 40 sec at 5000 rpm (about 1.6 μm) hotplate: 15 min at 90°C
mask aligner	20 sec exposure contacts of mask "Hall bar"
development	45 sec AR300-26 1:4 in DI-water stopping 60 sec in DI-water
AR300-49	180 sec etching AlGaSb (contains TMAH)
sulfuric passivation	mix $(NH_4)_2S$ 2:17 with DI-water (extractor hood!) use $HNO_3$ drop wise to achieve pH 9.2 (use pH-meter) immerse 30 sec, rinse 120 sec in DI-water
e-gun evaporation	10/100 nm Ti/Au
lift-off	30 min Aceton at 50 °C 1 min ultrasonic bath and rinse in IPA
<b>definition of the Hall bar</b>	
AR300-80	spincoating: 40 sec at 5000 rpm hotplate: 2 min at 120 °C 1 min cool down
AR-U4040	spincoating: 40 sec at 5000 rpm (about 1.6 μm) hotplate: 15 min at 90°C
mask aligner	20 sec exposure mesa of mask "Hall bar"

development	45 sec AR300-26 1:4 in DI-water
InAs etching	stopping 60 sec in DI-water adjust saturated succinic acid solution to pH 4.5 using $\text{NH}_4\text{OH}$ mix 12.8 : 1 with $\text{H}_2\text{O}_2$
stopping	150 sec wet etching rinse > 60 sec in DI-water
<b>applying magnet</b>	
AR-P 5460	spincoating: 40 sec at 5000 rpm hotplate: 5 min at 150°C
AR-U 4040	spincoating: 40 sec at 5000 rpm hotplate: 15 min at 90°C
mask aligner	20 sec primary exposure magnet structure hotplate: 5 min at 100°C
mask aligner development1	40 sec flood exposure 30 sec AR300-26 1:4 in DI-water stopping 60 sec in DI-water
development2	70 sec AR300-47 1:1 DI-water (for Co-polymer) stopping 60 sec in DI-water
DC sputtering	30 nm $\text{Ni}_{80}\text{Fe}_{20}$ 265 sec at 50 W 5 nm Ru: 50 sec at 50 W (exemplary)
lift-off	30 min acetone at 50 °C 1 min ultrasonic bath and rinse in isopropanol
<b>backend, contacting chip carrier</b>	
fixation	GI-Varnish + hotplate 5 min at 90°C Hybond: ultrasonic bonding (Au-wire)

Tab. A.1: Macro Hall bar process on InAs 2DEG stack.

## A.2 Micro-Hall Bar on InAs 2DEG

<b>pretreatment of the MBE-grown samples</b>	
cleaning	60 sec Aceton + 1 min ultrasonic bath
water desorption	rinse in IPA
<b>contacts and alignment marks</b>	
AR300-80	spincoating: 40 sec at 5000 rpm hotplate: 2 min at 120 °C 1 min cool down
AR-U4060	spincoating: 40 sec at 5000 rpm (about 580 nm) hotplate: 15 min at 90°C
mask aligner development	12 sec exposure of mask "micro-hall-bar" 45 sec AR300-26 1:4 in DI-water stopping 60 sec in DI-water
AR300-49	180 sec etching AlGaSb (contains TMAH)

sulfuric passivation	mix $(NH_4)_2S$ 2:17 with DI-water (extractor hood!) use $HNO_3$ drop wise to achieve pH 9.2 (use pH-meter) immerse 30 sec, rinse 120 sec in DI-water
e-gun evaporation	10/100 nm Ti/Au
lift-off	30 min Aceton at 50 °C 1 min ultrasonic bath and rinse in IPA
<b>definition of the Hall bar</b>	
AR-P679.03	spincoating 40 sec at 7000 rpm (about 120 nm) hotplate: 60 min at 200 °C
EBL: open marks	EHT: 5 keV; Ap. 30 $\mu m$ ; steps: 10 nm; dose: 100 $\frac{\mu C}{cm^2}$
development	60 sec IPA; stopping 60 sec DI-water
hotplate	2 min at 70°C
EBL ly 0:	EHT: 2.5 keV; Ap. 30 $\mu m$ ; steps: 10 nm; dose: 60 $\frac{\mu C}{cm^2}$
EBL ly 1:	EHT: 2.5 keV; Ap. 60 $\mu m$ ; steps: 25 nm; dose: 60 $\frac{\mu C}{cm^2}$
development	60 sec IPA; stopping 60 sec DI-water
CAIBE etching	1 min $Cl_2$ -assisted (AccV: 300 V; BeamV: 400 V; rate: 2.3 nm/sec)
resist stripping	2 hours NMP at 120 °C, rinse in ACE, IPA and DI-water 2 hours MIBK, rinse in ACE, IPA and DI-water
<b>deposition of the magnet</b>	
AR-P639.04	spincoating 40 sec at 4000 rpm (about 80 nm) hotplate: 60 min at 200°C
EBL: open marks	EHT: 5 keV; Ap. 30 $\mu m$ ; steps: 10 nm; dose: 100 $\mu C/cm^2$
development	60 sec isopropanol; stopping 60 sec DI-water
hotplate	2 min at 70°C
ly 2: magnet	EHT: 2.0 keV; Ap. 10 $\mu m$ ; steps: 10 nm; dose: 45 $\frac{\mu C}{cm^2}$ intra-proximity correction via PROXY
development	60 sec IPA; stopping 60 sec DI-water
DC sputtering	30 nm $Ni_{80}Fe_{20}$ 265 sec at 50 W 5 nm Ru: 50 sec at 50 W (exemplary)
lift-off	30 min acetone at 50 °C 1 min ultrasonic bath and rinse in isopropanol
<b>backend, contacting chip carrier</b>	
fixation	GI-Varnish + hotplate 5 min at 90°C Hybond: ultrasonic bonding (Au-wire)

Tab. A.2: Micro-Hall bar-process on InAs-2DEG stack.

### A.3 Macro-Hall Bar on HgTe 2DEG

<b>pretreatment of the MBE-grown samples</b>	
cleaning	60 sec Aceton + 1 min ultrasonic bath
water desorption	rinse in IPA
<b>definition etch mask</b>	
AR-U4040	spincoating: 40 sec at 5000 rpm (about 1.4 $\mu\text{m}$ ) hotplate: 2 min at 80°C
mask aligner	10 sec exposure mesa of mask "Hall bar"
development	45 sec AR300-26 1:4 in DI-water stopping 60 sec in DI-water
e-gun evaporation	15 nm Ti
lift-off	30 min acetone at 50 °C dip in ultrasonic bath and rinse in IPA
<b>dry etching</b>	
Ar sputtering	3 min etching (ExtrV -1 keV/AccV +1 keV, 10 mA, rate 50 nm/min)
Stripping mask	10 sec in HF 1:10 DI-water (etches caplayer) 2 min rinse in DI-water
<b>deposition gate electrode</b>	
PECVD	110 nm $\text{Si}_3\text{N}_4/\text{SiO}_2$ superlattice
AR-U4040	spincoating: 40 sec at 5000 rpm (about 1.6 $\mu\text{m}$ ) hotplate: 2 min at 80°C
mask aligner	15 sec exposure of mask with gate structure
development	45 sec AR300-26 1:4 in DI-water stop 60 sec in DI-water
e-gun evaporation	10 nm Ti + 100 nm Au
lift-off	10 min acetone at 50 °C syringe + Aceton, rinse in IPA
<b>backend, contacting chip carrier</b>	
fixation	GI-Varnish + hotplate 3 min at 80°C Indium bonding

Tab. A.3: Macro Hall bar process on HgTe 2DEG stack for characterization.



## A.4 Micro-Hall Bar on HgTe 2DEG

<b>pretreatment of the MBE-grown samples</b>	
cleaning water desorption	60 sec Aceton + 1 min ultrasonic bath rinse in IPA
<b>definition inner etch mask</b>	
AR-P679.03  EBL ly 0: marks + HB development  e-gun evaporation lift-off	spincoating: 40 sec at 7000 rpm (about 110 nm) hotplate: 60 min at 80°C EHT: 2.5 keV; Ap. 30 $\mu\text{m}$ ; step: 10 nm; dose: 55 $\frac{\mu\text{C}}{\text{cm}^2}$ 60 sec isopropanol stopping 60 sec DI-water 15 nm Ti (less hardly visible in mask aligner) 30 min acetone at 50 °C dip in ultrasonic bath and rinse in IPA 10 min MIBK at 60 ° C; rinse in IPA and DI-water
<b>definition outer etch mask</b>	
AR-U4060  mask aligner development e-gun evaporation lift-off	spincoating: 40 sec at 5000 rpm hotplate: 2 min at 80 °C 15 sec exposure of contact-mask 45 sec AR300-26 1:4 in DI-water; stop 60 sec in DI-water 15 nm Ti 30 min acetone at 50 °C dip in ultrasonic bath and rinse in IPA
<b>dry etching</b>	
Ar sputtering  Stripping mask	3 min etching (ExtrV -1 keV/AccV +1 keV, 10 mA, rate 50 nm/min) 10 sec in HF 1:10 DI-water 2 min rinse in DI-water
<b>deposition of nanomagnet</b>	
AR-P639.04  EBL: open marks development hotplate ly 2: magnet  development DC sputtering  lift-off	spincoating 40 sec at 4000 rpm (about 80 nm) hotplate: 60 min at 80 °C EHT: 5 keV; Ap. 30 $\mu\text{m}$ ; steps: 10 nm; dose: 100 $\frac{\mu\text{C}}{\text{cm}^2}$ 60 sec IPA; stopping 60 sec DI-water 1 min at 60°C EHT: 2.0 keV; Ap. 10 $\mu\text{m}$ ; steps: 10 nm; dose: 45 $\frac{\mu\text{C}}{\text{cm}^2}$ intra-proximity correction via PROXY 60 sec IPA; stopping 60 sec DI-water 30 nm $Ni_{80}Fe_{20}$ 265 sec at 50 W 5 nm Ru: 50 sec at 50 W (exemplary) 30 min acetone at 50 °C 1 min ultrasonic bath and rinse in isopropanol
<b>variant: gate electrode</b>	
PECVD	110 nm $Si_3N_4/SiO_2$ superlattice
AR-U4040	spincoating: 40 sec at 5000 rpm (about 1.6 $\mu\text{m}$ )

mask aligner development	hotplate: 2 min at 80°C 15 sec exposure of mask with gate structure 45 sec AR300-26 1:4 in DI-water; stop 60 sec in DI-water
E-gun evaporation lift-off	10 nm Ti + 100 nm Au 10 min acetone at 50 °C syringe + Aceton, rinse in IPA
<b>backend, contacting chip carrier</b>	
fixation	GI-Varnish + hotplate 3 min at 80°C Indium bonding

Tab. A.4: Micro-Hall bar-process on HgTe-2DEG stack.

## A.5 Micro-SQUID Fabrication

<b>pretreatment of the Si-substrate</b>	
cleaning water desorption	60 sec Aceton + 1 min ultrasonic bath rinse in IPA
<b>deposition of the superconducting layer stack</b>	
DC-Sputtering	40 sec at 200 W pre-sputtering of Nb target to remove dirt 15 nm Nb: 40 sec at 400 W 10 nm Al: 87 sec at 50 W 10 nm Ru: 100 sec at 50 W
<b>definition of micro-SQUID etch mask</b>	
AR-669.04	spincoating 40 sec at 6000 rpm (about 150 nm) hotplate: 60 min at 200 ° C
AR-679.03	spincoating 40 sec at 6000 rpm (about 150 nm) hotplate: 60 min at 180 ° C
EBL	EHT: 30 keV; Ap. 30 $\mu\text{m}$ ; steps: 5 nm; doses: 200 nm lines $600 \frac{\mu\text{C}}{\text{cm}^2}$ , single pixel lines $5 \frac{\mu\text{C}}{\text{cm}}$
development E-gun evaporation lift-off	60 sec IPA; stopping 60 sec DI-water 30 nm Ti 30 min acetone at 50 °C 5 min ultrasonic bath and rinse in isopropanol 2 h MIBK @ 60 ° C, rinse in IPA and DI-water
<b>definition of contacts</b>	
AR-U5350	40 sec at 5000 rpm hotplate: 5 min at 105 ° C
mask aligner development E-gun evaporation lift-off	4 sec exposure of contact-mask 30 sec AR300-26 1:8 in DI-water; stop 60 sec in DI-water 10/120/15 nm Ti/Au/Ti 30 min acetone at 50 °C dip in ultrasonic bath and rinse in IPA

<b>dry etching - option I</b>	
Ar-Sputtering RIE	6 min etching (ExtrV -1 keV/AccV +1 keV, current: 10 mA) 5 min 70 W, 50 sccm $CHF_3$ , 5 sccm $O_2$ , $55 \cdot 10^{-3}$ mbar
<b>dry etching - option II</b>	
CAIBE	150 sec Ar-sputtering AccV 300V, BeamV 400 V, Ar1: 10 sccm, Ar2: 6 sccm
<b>variant: deposition of magnet</b>	
AR-639.04  EBL  development DC-Sputter-Deposition  lift-off	spincoating 40 sec at 4000 rpm (about 80 nm) hotplate: 60 min at 200 ° C EHT: 2.0 keV; Ap. 30 $\mu$ m; steps: 10 nm; dose: 50 $\mu C/cm^2$ intra-proximity correction via PROXY 60 sec IPA; stopping 60 sec DI-water 30 nm $Ni_{80}Fe_{20}$ 265 sec at 50 W 5 nm Ru: 50 sec at 50 W (exemplary) 30 min acetone at 50 ° C 1 min ultrasonic bath and rinse in isopropanol 10 min MIBK at 60 ° C; rinse in IPA and DI-water
<b>backend, contacting chip carrier</b>	
fixation	GI-Varnish + hotplate 5 min at 90°C Hybond: ultrasonic SQUID-process on p-doped Si-wafer

Tab. A.5: Micro-SQUID-process on doped Si-substrate.



# Appendix B

## Substrates and Samples

InAs Substrates				
$InAs/Al_xGa_{1-x}Sb$	$n [cm^{-2}]$		$\mu [cm^2/Vs]$	
	4.2 K	RT	4.2 K	RT
Ga3588 (x=0.2)	$1.0 \cdot 10^{12}$	$2.9 \cdot 10^{12}$	$2.1 \cdot 10^5$	$3.0 \cdot 10^4$
Ga4777 (x=0.35)	$8.9 \cdot 10^{11}$	$5.5 \cdot 10^{12}$	$1.5 \cdot 10^5$	$2.0 \cdot 10^4$
Ga4982 (x=0.35)	$1.5 \cdot 10^{12}$	N/A	$1.5 \cdot 10^5$	N/A

**Tab. B.1:** Carrier concentration  $n$  and mobility  $\mu$  of used InAs 2DEGs

InAs Samples			
Name	Fabrication name	Substrate	Description
In2DEG1	GA4982.2DEG	GA4982	wet-etched macro-HB
In2DEG2.1	BBMUHB2	GA3588	wet-etched micro-HB
In2DEG2.2	BBMUHB-a2	GA3588	dry-etched micro-HB
InAs1.1	GGB05	GA4777	Macro-HB; CoFe $w = 50 \mu m$
InAs1.2	GGB03	GA4777	Macro-HB; CoFe $w = 50 \mu m$
InAs2	GGB07	GA3588	Macro-HB; CoFe $w = 20 \mu m$
InAs3.1	MUHB_c4al	GA3588	Micro-HB $A_{HC} = 4 \mu m^2$ ; CoFeB $w = 0.5 \mu m$
InAs3.2	MUHB_c4br	GA3588	Micro-HB $A_{HC} = 4 \mu m^2$ ; CoFeB $w = 1.0 \mu m$
InAs3.3	MUHB_c4ar	GA3588	Micro-HB $A_{HC} = 4 \mu m^2$ ; CoFeB $w = 1.5 \mu m$
InAs4	MUHB_c4bl	GA3588	Micro-HB $A_{HC} = 16 \mu m^2$ ; CoFeB $w = 0.5 \mu m$

**Tab. B.2:** InAs samples used within this work.

HgTe Substrates											
sample	cap nm	iface nm	doping arb. units	spacer nm	well nm	spacer nm	iface nm	doping arb. units	buffer nm	n $cm^{-2}$	$\mu$ $cm^2/Vs$
Q2212	25	9	0.05	10	6.5	10	9	0.05	100	$4.9 \cdot 10^{11}$	$2.31 \cdot 10^5$
Q2268	25	9	0.08	10	8.0	10	9	0.08	100	$7.3 \cdot 10^{11}$	$1.83 \cdot 10^5$
Q2306	25	NA	NA	NA	8.0	10	9	0.28	100	$7.2 \cdot 10^{11}$	$0.96 \cdot 10^5$
Q2339	25	9	0.14	40	8.0	NA	NA	NA	100	$6.2 \cdot 10^{11}$	$3.63 \cdot 10^5$
Q2366	15	NA	NA	NA	7.0	70	9	0.14	100	$6.9 \cdot 10^{11}$	$2.13 \cdot 10^5$
Q2386	15	NA	NA	NA	6.5	100	9	0.1	100	$2.98 \cdot 10^{11}$	$2.79 \cdot 10^5$
Q2395	25	9	0.1	60	7.0	NA	NA	NA	150	$5.4 \cdot 10^{11}$	$1.22 \cdot 10^5$
Q2396	25	9	0.1	60	6.5	NA	NA	NA	150	$5.0 \cdot 10^{11}$	$1.98 \cdot 10^5$
Q2397	25	9	0.1	60	6.0	NA	NA	NA	150	$5.4 \cdot 10^{11}$	$1.30 \cdot 10^5$
Q2398	25	9	0.1	60	5.0	NA	NA	NA	150	$5.5 \cdot 10^{11}$	$1.30 \cdot 10^5$

**Tab. B.3:** nominal growth parameter of used HgTe substrates. Carrier concentration and mobility are given for  $T = 4.2 K$ .

HgTe Samples			
Name	Fabrication name	Substrate	Description
HGM1	Q2212_MUHB300nm	Q2212	MHM, $A_{HC} = 0.09 \mu m^2$ ; Py 300 nm
HGM2	Q2306_2	Q2306	MHM, $A_{HC} = 0.045 \mu m^2$ ; Py 100 nm
HWAL1.1	Q2268_300nm	Q2268	symmetric QW with $d_{QW} = 8.0 nm$
HWAL1.2	Q2268_500nm	Q2268	symmetric QW with $d_{QW} = 8.0 nm$
HWAL2	Q2212_300nmwgate	Q2212	symmetric QW with $d_{QW} = 6.5 nm$
HWAL3	Q2339_WAL1	Q2339	top-doped QW with $d_{QW} = 8.0 nm$
HWAL4	Q2366_WALnoRashba	Q2366	bottom-doped QW with $d_{QW} = 7.0 nm$
HWAL5	Q2398_WAL-N	Q2398	top-doped QW with $d_{QW} = 5.0 nm$

**Tab. B.4:** HgTe samples used within this thesis.

# Appendix C

## Magnetic Materials

material	$M_S$ kA/m	A pJ/m
Fe	1710	10
Co	1430	10
Ni	484	10
Py	800	13

**Tab. C.1:** Material parameters for the most common ferromagnetic materials; taken from [Sch91, Hoc03].





# Abbreviations

<b>2DEG</b>	Two-Dimensional Electron Gas
<b>BIA</b>	Bulk Inversion Asymmetry
<b>DC</b>	Direct Current
<b>DOS</b>	Density Of States
<b>DW</b>	Domain Wall
<b>EBL</b>	Electron Beam Lithography
<b>HB</b>	Hall Bar
<b>LL</b>	Landau Level
<b>MHM</b>	Micro-Hall Magnetometry
<b>PCB</b>	Printed Circuit Board
<b>Py</b>	Permalloy
<b>SdH</b>	Shubnikov-de Haas
<b>SIA</b>	Structural Inversion Asymmetry
<b>SOI</b>	Spin-Orbit Interaction
<b>QC</b>	Quantization Criterion
<b>QHE</b>	Quantum Hall Effect
<b>QSHE</b>	Quantum Spin Hall Effect
<b>QW</b>	Quantum Well
<b>SEM</b>	Scanning Electron Microscopy
<b>SQUID</b>	Superconducting-Quantum-Interference-Device
<b>UCF</b>	Universal Conductance Fluctuations
<b>WAL</b>	Weak Anti-Localization



# Bibliography

- [Aha00] A. Aharoni, *Introduction to the Theory of Ferromagnetism*, vol. 109, Oxford University Press, USA, 2000.
- [Al85] BL Altshuler, *Fluctuations in the extrinsic conductivity of disordered conductors*, JETP Letters **41** (1985), no. 12.
- [ATAF80] PW Anderson, DJ Thouless, E. Abrahams, and DS Fisher, *New method for a scaling theory of localization*, Physical Review B **22** (1980), no. 8, 3519.
- [Bat08] Martin Batzer, *Herstellung und Charakterisierung von Micro-SQUIDs aus Niob*, Diplomarbeit, Universität Würzburg, 2008.
- [BBF<sup>+</sup>88] MN Baibich, JM Broto, A. Fert, F.N. Van Dau, F. Petroff, P. Etienne, G. Creuzet, A. Friederich, and J. Chazelas, *Giant magnetoresistance of (001) Fe/(001) Cr magnetic superlattices*, Physical Review Letters **61** (1988), no. 21, 2472–2475.
- [BBNK97] S. Bhargava, H.R. Blank, V. Narayanamurti, and H. Kroemer, *Fermi-level pinning position at the Au–InAs interface determined using ballistic electron emission microscopy*, Applied Physics Letters **70** (1997), 759.
- [Ber82] G. Bergmann, *Weak anti-localization—An experimental proof for the destructive interference of rotated spin 1/2*, Solid State Communications **42** (1982), no. 11, 815–817.
- [Ber84] ———, *Weak localization in thin films: a time-of-flight experiment with conduction electrons*, Physics Reports **107** (1984), no. 1, 1 – 58.
- [Ber87] ———, *Electron scattering by electron holograms: The physical interpretation of the Coulomb anomaly in disordered electron systems*, Phys. Rev. B **35** (1987), 4205–4215.
- [BFT<sup>+</sup>01] V. Bouchiat, M. Faucher, C. Thirion, W. Wernsdorfer, T. Fournier, and B. Panetier, *Josephson junctions and superconducting quantum interference devices made by local oxidation of niobium ultrathin films*, Applied Physics Letters **79** (2001), 123.
- [BGS<sup>+</sup>89] G. Binasch, P. Grünberg, F. Saurenbach, W. Zinn, et al., *Enhanced magnetoresistance in layered magnetic structures with antiferromagnetic interlayer exchange*, Physical Review B **39** (1989), no. 7, 4828–4830.

- [BHZ06] B.A. Bernevig, T.L. Hughes, and S.C. Zhang, *Quantum spin Hall effect and topological phase transition in HgTe quantum wells*, *Science* **314** (2006), no. 5806, 1757.
- [Bib00] M. Bibus, *Herstellung und Charakterisierung von Nanostrukturen aus InAs/AlGaSb*, Diplomarbeit, Rheinisch-Westfälische Technische Hochschule Aachen, 2000.
- [BLT<sup>+</sup>11] B. Büttner, CX Liu, G. Tkachov, EG Novik, C. Brüne, H. Buhmann, EM Hankiewicz, P. Recher, B. Trauzettel, SC Zhang, et al., *Single valley Dirac fermions in zero-gap HgTe quantum wells - Supplementary Material*, *Nature Physics* **7** (2011), no. 5, 418–422.
- [BO97] SJ Bending and A. Oral, *Hall effect in a highly inhomogeneous magnetic field distribution*, *Applied Physics Letters* **81** (1997), no. 8, 3721–3725.
- [BRN<sup>+</sup>10] C. Brüne, A. Roth, EG Novik, M. König, H. Buhmann, EM Hankiewicz, W. Hanke, J. Sinova, and LW Molenkamp, *Evidence for the ballistic intrinsic spin Hall effect in HgTe nanostructures*, *Nature Physics* **6** (2010), no. 6, 448–454.
- [Bro64] W.F. Brown, *Some magnetostatic and micromagnetic properties of the infinite rectangular bar*, *Journal of Applied Physics* **35** (1964), no. 7, 2102–2106.
- [Brü07] C. Brüne, *Wachstum und Charakterisierung von HgTe Halbleiterheterostrukturen*, Diplomarbeit, Diplomarbeit, Universität Würzburg, 2007.
- [BSJ<sup>+</sup>08] K.I. Bolotin, K.J. Sikes, Z. Jiang, M. Klima, G. Fudenberg, J. Hone, P. Kim, and H.L. Stormer, *Ultrahigh electron mobility in suspended graphene*, *Solid State Communications* **146** (2008), no. 9-10, 351 – 355.
- [Büt05] B. Büttner, *Herstellung und Charakterisierung von NiMnSb Nanostrukturen*, Diplomarbeit, Diplomarbeit, Universität Würzburg, 2005.
- [BVH88] CWJ Beenakker and H. Van Houten, *Flux-cancellation effect on narrow-channel magnetoresistance fluctuations*, *Physical Review B* **37** (1988), 6544–6546.
- [BVH89] ———, *Billiard model of a ballistic multiprobe conductor*, *Physical Review Letters* **63** (1989), no. 17, 1857–1860.
- [BvH91] CWJ Beenakker and H. van Houten, *Quantum transport in semiconductor nanostructures*, *Solid State Physics* **44** (1991), 1–228.
- [CB06] J. Clarke and A.I. Braginski, *The SQUID handbook*, vol. 1, Wiley Online Library, 2006.
- [CEKP<sup>+</sup>91] C. Chapelier, M. El Khatib, P. Perrier, A. Benoit, and D. Mailly, *Superconducting Devices and Their Applications, SQUID 91*, edited by H. Koch and H Lübbig, 1991.
- [CGDB<sup>+</sup>07] A. Candini, GC Gazzadi, A. Di Bona, M. Affronte, D. Ercolani, G. Biasiol, and L. Sorba, *Focused ion beam patterned Hall nano-sensors*, *Journal of Magnetism and Magnetic Materials* **310** (2007), no. 2, 2752–2754.

- 
- [CNGP<sup>+</sup>09] AH Castro Neto, F. Guinea, NMR Peres, KS Novoselov, and AK Geim, *The electronic properties of graphene*, Reviews of Modern Physics **81** (2009), 109–162.
- [CP02] YG Cornelissens and FM Peeters, *Response function of a Hall magnetosensor in the diffusive regime*, Journal of Applied Physics **92** (2002), 2006.
- [CTP86] KK Choi, DC Tsui, and SC Palmateer, *Electron-electron interactions in GaAs-Al<sub>x</sub>Ga<sub>1-x</sub>As heterostructures*, Physical Review B **33** (1986), no. 12, 8216.
- [CYY00] KA Cheng, CH Yang, and MJ Yang, *Nanometer-size InAs/AlSb quantum wires: Fabrication and characterization of Aharonov–Bohm quantum rings*, Journal of Applied Physics **88** (2000), 5272.
- [Dat95] S. Datta, *Electronic transport in mesoscopic systems*, Cambridge University Press, 1995.
- [Dru00] P. Drude, *Zur Elektronentheorie der Metalle*, Annalen der Physik **306** (1900), no. 3, 566–613.
- [GDJ<sup>+</sup>07] C. Gourdon, A. Dourlat, V. Jeudy, K. Khazen, H.J. Von Bardeleben, L. Thevenard, and A. Lemaître, *Determination of the micromagnetic parameters in (Ga, Mn) As using domain theory*, Physical Review B **76** (2007), no. 24, 241301.
- [GDL<sup>+</sup>97] AK Geim, SV Dubonos, JGS Lok, IV Grigorieva, JC Maan, L.T. Hansen, and PE Lindelof, *Ballistic hall micromagnetometry*, Applied Physics Letters **71** (1997), 2379.
- [GGPJ<sup>+</sup>98] F. Goschenhofer, J. Gerschütz, A. Pfeuffer-Jeschke, R. Hellmig, CR Becker, and G. Landwehr, *Investigation of iodine as a donor in MBE grown Hg<sub>1-x</sub>Cd<sub>x</sub>Te*, Journal of Electronic Materials **27** (1998), no. 6, 532–535.
- [GJFD<sup>+</sup>02] J. Gallop, PW Josephs-Franks, J. Davies, L. Hao, and J. Macfarlane, *Miniature dc SQUID devices for the detection of single atomic spin-flips*, Physica C: Superconductivity **368** (2002), no. 1-4, 109–113.
- [GLK79] LP Gorkov, AI Larkin, and DE Khmel'nitskii, *Particle conductivity in a two-dimensional random potential*, JETP Lett **30** (1979), no. 4, 228.
- [GN07] A.K. Geim and K.S. Novoselov, *The rise of graphene*, Nature Materials **6** (2007), no. 3, 183–191.
- [GNY<sup>+</sup>07] AK Geim, KS Novoselov, O.V. Yazyev, S.G. Louie, S. Ghosh, W. Bao, D.L. Nika, S. Subrina, E.P. Pokatilov, C.N. Lau, et al., *Nobel Prize for graphene*, Nature Materials **6** (2007), 183–192.
- [GP06] W.J. Gallagher and S.S.P. Parkin, *Development of the magnetic tunnel junction MRAM at IBM: From first junctions to a 16-Mb MRAM demonstrator chip*, IBM Journal of Research and Development **50** (2006), no. 1, 5–23.
- [Gra05] P. Grabs, *Herstellung von Bauelementen für Spininjektionsexperimente mit semimagnetischen Halbleitern*, Dissertation, Universität Würzburg, 2005.

- [Hal79] E.H. Hall, *On a new action of the magnet on electric currents*, American Journal of Mathematics **2** (1879), no. 3, 287–292.
- [Hal82] BI Halperin, *Quantized Hall conductance, current-carrying edge states, and the existence of extended states in a two-dimensional disordered potential*, Physical Review B **25** (1982), no. 4, 2185.
- [Hal88] FDM Haldane, *Model for a quantum Hall effect without Landau levels: Condensed-matter realization of the "parity anomaly"*, Physical Review Letters **61** (1988), no. 18, 2015–2018.
- [HBS<sup>+</sup>06] J. Hinz, H. Buhmann, M. Schäfer, V. Hock, CR Becker, and LW Molenkamp, *Gate control of the giant Rashba effect in HgTe quantum wells*, Semiconductor Science and Technology **21** (2006), 501.
- [Hei28] W. Heisenberg, *Zur Theorie des Ferromagnetismus*, Zeitschrift für Physik A Hadrons and Nuclei **49** (1928), no. 9, 619–636.
- [HK02] R. Hertel and H. Kronmüller, *Finite element calculations on the single-domain limit of a ferromagnetic cubea solution to  $\mu$ MAG Standard Problem No. 3*, Journal of Magnetism and Magnetic Materials **238** (2002), no. 2, 185–199.
- [HLN80] S. Hikami, A.I. Larkin, and Y. Nagaoka, *Spin–Orbit Interaction and Magnetoresistance in the Two-Dimensional Random System*, Progress of Theoretical Physics **63** (1980), no. 2, 707–710.
- [HMK02] K. Hasselbach, D. Mailly, and JR Kirtley, *Micro-superconducting quantum interference device characteristics*, Journal of Applied Physics **91** (2002), 4432.
- [Hoc03] S. Hoch, *Hall-Magnetometrie-Untersuchungen an mikro-und nanostrukturierten ferromagnetischen Filmen*, Dissertation, Ruhr-Universität Bochum, Universitätsbibliothek, 2003.
- [HS98] A. Hubert and R. Schäfer, *Magnetic domains: the analysis of magnetic microstructures*, Springer Verlag, 1998.
- [JL05] J. Jin and X.Q. Li, *Measurement of single electron spin with submicron Hall magnetometer*, Applied Physics Letters **86** (2005), 143504.
- [JLSM64] RC Jaklevic, J. Lambe, AH Silver, and JE Mercereau, *Quantum interference effects in Josephson tunneling*, Physical Review Letters **12** (1964), no. 7, 159–160.
- [KBMH08] M. König, H. Buhmann, L.W. Molenkamp, and T. Hughes, *The quantum spin hall effect: Theory and experiment*, Journal of the Physical Society of Japan **77** (2008), no. 3, 031007.
- [KDP80] K. Klitzing, G. Dorda, and M. Pepper, *New method for high-accuracy determination of the fine-structure constant based on quantized Hall resistance*, Physical Review Letters **45** (1980), no. 6, 494–497.

- 
- [Kit05] C. Kittel, *Einführung in die Festkörperphysik*, Oldenbourg Wissenschaftsverlag, 2005.
- [KWB<sup>+</sup>07] M. König, S. Wiedmann, C. Brüne, A. Roth, H. Buhmann, L.W. Molenkamp, X.L. Qi, and S.C. Zhang, *Quantum spin hall insulator state in HgTe quantum wells*, *Science* **318** (2007), no. 5851, 766.
- [LBH95] JL Leclercq, E. Bergignat, and G. Hollinger, *Surface chemistry of InAlAs after (NH<sub>4</sub>)<sub>2</sub>Sx sulphidation*, *Semiconductor Science and Technology* **10** (1995), 95.
- [LCKW01] J. Lohau, A. Carl, S. Kirsch, and EF Wassermann, *Magnetization reversal and coercivity of a single-domain Co/Pt dot measured with a calibrated magnetic force microscope tip*, *Applied Physics Letters* **78** (2001), 2020.
- [Lee86] P.A. Lee, *Universal conductance fluctuations in disordered metals*, *Physica A: Statistical Mechanics and its Applications* **140** (1986), no. 1-2, 169–174.
- [LGK<sup>+</sup>98] S. Liu, H. Guillou, AD Kent, GW Stupian, and MS Leung, *Effect of probe geometry on the Hall response in an inhomogeneous magnetic field: A numerical study*, *Journal of Applied Physics* **83** (1998), 6161.
- [Lik79] KK Likharev, *Superconducting weak links*, *Reviews of Modern Physics* **51** (1979), no. 1, 101.
- [LL35] L. Landau and E. Lifshitz, *On the theory of the dispersion of magnetic permeability in ferromagnetic bodies*, *Phys. Z. Sowjetunion* **8** (1935), no. 153, 101–114.
- [LS85] PA Lee and A.D. Stone, *Universal conductance fluctuations in metals*, *Physical Review Letters* **55** (1985), no. 15, 1622–1625.
- [LSF87] PA Lee, A.D. Stone, and H. Fukuyama, *Universal conductance fluctuations in metals: Effects of finite temperature, interactions, and magnetic field*, *Physical Review B* **35** (1987), no. 3, 1039.
- [LXvM<sup>+</sup>02] Y. Li, P. Xiong, S. von Molnár, S. Wirth, Y. Ohno, and H. Ohno, *Hall magnetometry on a single iron nanoparticle*, *Applied Physics Letters* **80** (2002), 4644.
- [Mih06] G. Mihajlovic, *InAs quantum well Hall devices for room-temperature detection of magnetic biomolecular labels*, Ph.D. thesis, Florida State University, 2006.
- [MJR97] FG Monzon, M. Johnson, and ML Roukes, *Strong Hall voltage modulation in hybrid ferromagnet/semiconductor microstructures*, *Applied Physics Letters* **71** (1997), 3087.
- [Moo65] GE Moore, *Cramming more components onto integrated circuits*, *Electronics* **38** (1965), no. 8, 114–117.
- [ND57] T. Noyes and WE Dickinson, *The Random-Access Memory Accounting Machine II. The Magnetic-Disk, Random-Access Memory*, *IBM Journal of Research and Development* **1** (1957), no. 1, 72–75.

- [NGM<sup>+</sup>05] K. S. Novoselov, A. K. Geim, S. V. Morozov, D. Jiang, M. I. Katsnelson, I. V. Grigorieva, S. V. Dubonos, and A. A. Firsov, *Two-dimensional gas of massless Dirac fermions in graphene*, *Nature* **438** (2005), no. 7065, 197–200.
- [NPJJ<sup>+</sup>05] EG Novik, A. Pfeuffer-Jeschke, T. Jungwirth, V. Latussek, CR Becker, G. Landwehr, H. Buhmann, and LW Molenkamp, *Band structure of semimagnetic Hg- $\{1-y\}$  Mn- $\{y\}$  Te quantum wells*, *Physical Review B* **72** (2005), no. 3, 035321.
- [OBH96] A. Oral, SJ Bending, and M. Henini, *Real-time scanning Hall probe microscopy*, *Applied Physics Letters* **69** (1996), 1324.
- [Onn11] H.K. Onnes, *Further experiments with liquid helium*, *Proceedings of the KNAW*, vol. 13, 1911, pp. 1910–1911.
- [PJ00] A. Pfeuffer-Jeschke, *Bandstruktur und Landau-Niveaus quecksilberhaltiger II-VI-Heterostrukturen*, Dissertation, Universität Würzburg, 2000.
- [PL98] FM Peeters and XQ Li, *Hall magnetometer in the ballistic regime*, *Applied Physics Letters* **72** (1998), 572.
- [PSH<sup>+</sup>87] S. Perkowitz, R. Sudharsanan, K. A. Harris, J. W. Cook, J. F. Schetzina, and J. N. Schulman, *Effective mass in an n-type HgTe-CdTe superlattice*, *Phys. Rev. B* **36** (1987), 9290–9292.
- [PTH83] MA Paalanen, DC Tsui, and JCM Hwang, *Parabolic magnetoresistance from the interaction effect in a two-dimensional electron gas*, *Physical Review Letters* **51** (1983), no. 24, 2226–2229.
- [PYW03] DY Petrovykh, MJ Yang, and LJ Whitman, *Chemical and electronic properties of sulfur-passivated InAs surfaces*, *Surface science* **523** (2003), no. 3, 231–240.
- [Rah05] M. Rahm, *Mikro-Hall-Magnetometrie an ferromagnetischen Nanoscheiben*, Dissertation, 2005.
- [RBB<sup>+</sup>09] A. Roth, C. Brüne, H. Buhmann, L.W. Molenkamp, J. Maciejko, X.L. Qi, and S.C. Zhang, *Nonlocal transport in the quantum spin Hall state*, *Science* **325** (2009), no. 5938, 294.
- [RM02] S.K. Range and J. Mullins, *Gravity Probe B: Examining Einstein*.
- [RPS<sup>+</sup>00] J. Raabe, R. Pulwey, R. Sattler, T. Schweinböck, J. Zweck, and D. Weiss, *Magnetization pattern of ferromagnetic nanodisks*, *Journal of Applied Physics* **88** (2000), 4437.
- [RTB07] A. Rycerz, J. Tworzydło, and CWJ Beenakker, *Anomalously large conductance fluctuations in weakly disordered graphene*, *EPL (Europhysics Letters)* **79** (2007), 57003.



- 
- [SA02] Hidekatsu Suzuura and Tsuneya Ando, *Crossover from Symplectic to Orthogonal Class in a Two-Dimensional Honeycomb Lattice*, Physical Review Letters **89** (2002), 266603.
- [SAT<sup>+</sup>97] O. V. Snigirev, K. E. Andreev, A. M. Tishin, S. A. Gudoshnikov, and J. Bohr, *Magnetic properties of thin Ni films measured by a dc SQUID-based magnetic microscope*, Phys. Rev. B **55** (1997), 14429–14433.
- [Sch91] M.E. Schabes, *Micromagnetic theory of non-uniform magnetization processes in magnetic recording particles*, Journal of Magnetism and Magnetic Materials **95** (1991), no. 3, 249–288.
- [Sch96] P.G. Schmidl, *Two Early Arabic Sources On The Magnetic Compass*, Journal of Arabic and Islamic Studies **1** (1996), no. 1997-98, 82.
- [SdHV<sup>+</sup>05] L. Schultz, O. de Haas, P. Verges, C. Beyer, S. Rohlig, H. Olsen, L. Kuhn, D. Berger, U. Noteboom, and U. Funk, *Superconductively levitated transport system-the Supra-Trans project*, Applied Superconductivity, IEEE Transactions on **15** (2005), no. 2, 2301–2305.
- [SNKT09] MJ Schmidt, EG Novik, M. Kindermann, and B. Trauzettel, *Optical manipulation of edge-state transport in HgTe quantum wells in the quantum Hall regime*, Physical Review B **79** (2009), no. 24, 241306.
- [Sta10] A. Stahl, Dissertation, Universität Würzburg, 2010.
- [SW48] E.C. Stoner and EP Wohlfarth, *A mechanism of magnetic hysteresis in heterogeneous alloys*, Philosophical Transactions of the Royal Society of London. Series A. Mathematical and Physical Sciences (1948), 599–642.
- [TBM<sup>+</sup>97] A. Thiaville, L. Belliard, D. Majer, E. Zeldov, and J. Miltat, *Measurement of the stray field emanating from magnetic force microscope tips by Hall effect microsensors*, Journal of Applied Physics **82** (1997), 3182.
- [TH11] G. Tkachov and EM Hankiewicz, *Weak antilocalization in HgTe quantum wells and topological surface states: Massive versus massless Dirac fermions*, Physical Review B **84** (2011), no. 3, 035444.
- [TKGL<sup>+</sup>00] L. Theil Kuhn, A.K. Geim, JGS Lok, P. Hedegård, K. Ylänen, JB Jensen, E. Johnson, and PE Lindelof, *Magnetisation of isolated single crystalline Fe-nanoparticles measured by a ballistic Hall micro-magnetometer*, The European Physical Journal D-Atomic, Molecular, Optical and Plasma Physics **10** (2000), no. 2, 259–263.
- [TTP<sup>+</sup>11] G. Tkachov, C. Thienel, V. Pinneker, B. Büttner, C. Brüne, H. Buhmann, LW Molenkamp, and EM Hankiewicz, *Backscattering of Dirac Fermions in HgTe Quantum Wells with a Finite Gap*, Physical Review Letters **106** (2011), no. 7, 76802.

- [WAT<sup>+</sup>87] MK Wu, JR Ashburn, C.J. Torng, P.H. Hor, RL Meng, L. Gao, Z.J. Huang, YQ Wang, and CW Chu, *Superconductivity at 93 K in a new mixed-phase Y-Ba-Cu-O compound system at ambient pressure*, Physical Review Letters **58** (1987), no. 9, 908–910.
- [Wei07] P. Weiss, *L'hypothèse du champ moléculaire et la propriété ferromagnétique*, J. de Phys. **6** (1907), 661–690.
- [Wer09] W. Wernsdorfer, *From micro-to nano-SQUIDs: applications to nanomagnetism*, Superconductor Science and Technology **22** (2009), 064013.
- [WHB<sup>+</sup>95] W. Wernsdorfer, K. Hasselbach, A. Benoit, B. Barbara, D. Mailly, J. Tuailon, JP Perez, V. Dupuis, JP Dupin, G. Guiraud, et al., *High sensitivity magnetization measurements of nanoscale cobalt clusters*, Journal of Applied Physics **78** (1995), no. 12, 7192–7195.
- [WHM<sup>+</sup>95] W. Wernsdorfer, K. Hasselbach, D. Mailly, B. Barbara, A. Benoit, L. Thomas, and G. Suran, *DC-SQUID magnetization measurements of single magnetic particles*, Journal of Magnetism and Magnetic Materials **145** (1995), no. 1-2, 33–39.
- [Wil62] L.P. Williams, *Ampère's electrodynamic molecular model*, Contemporary Physics **4** (1962), no. 2, 113–123.
- [Zim79] J.M. Ziman, *Principles of the Theory of Solids*, Cambridge University Press, 1979.
- [ZPJO<sup>+</sup>01] XC Zhang, A. Pfeuffer-Jeschke, K. Ortner, V. Hock, H. Buhmann, CR Becker, and G. Landwehr, *Rashba splitting in n-type modulation-doped HgTe quantum wells with an inverted band structure*, Physical Review B **63** (2001), no. 24, 245305.
- [ZTSK05] Yuanbo Zhang, Yan-Wen Tan, Horst L. Stormer, and Philip Kim, *Experimental observation of the quantum Hall effect and Berry's phase in graphene*, Nature **438** (2005), no. 7065, 201–204.

# List of Figures

2.1	Magnetization progression of a magnet without history . . . . .	18
2.2	Landau domain structure with a closed loop . . . . .	22
2.3	Width-dependent coercive field progression . . . . .	25
2.4	Sketch of the geometry used for calculations of the stray field . . . . .	27
2.5	Calculated $B_z$ -component of the stray field for varied parameters . . . . .	28
2.6	Layer composition of the InAs 2DEG . . . . .	34
2.7	Layer composition of the HgTe quantum well . . . . .	35
2.8	Sketch of the Hall effect and geometry of a Hall bar . . . . .	39
2.9	Quantum Hall effect and SdH oscillations on InAs 2DEG . . . . .	42
2.10	Density of states in magnetic field and Landau level fan chart . . . . .	44
2.11	Basic principle of a sensor based on micro-Hall magnetometry . . . . .	46
2.12	Hall response function . . . . .	47
2.13	Current and equipotential lines in a Hall cross . . . . .	48
2.14	Ballistic effects in a Hall cross and last plateau . . . . .	49
2.15	Process flow for the fabrication of MHM sensors on InAs 2DEG. . . . .	54
2.16	Process flow for the fabrication of MHM sensors on HgTe 2DEG. . . . .	56
2.17	Sketch of the sample holder . . . . .	57
2.18	Sketch of the setup used for cryogenic temperatures . . . . .	58
2.19	Hall Magnetometry on Macro-Hall bar . . . . .	60
2.20	Micrograph of dry-etched sample and measurement of last plateau . . . . .	62
2.21	MHM measurements on InAs for magnets with different widths . . . . .	63
2.22	MHM measurements for two different active areas . . . . .	64
2.23	MHM measurement for 4.2 K and at room temperature . . . . .	65
2.24	MHM sensor and measurement on HgTe . . . . .	67
2.25	Temperature dependent MHM measurement on HgTe . . . . .	68
2.26	MHM on 200 nm wide HgTe Hall bar . . . . .	69
2.27	Geometry of a micro-SQUID . . . . .	73
2.28	Integration path around the superconducting loop. . . . .	75
2.29	Currents in a micro-SQUID . . . . .	78
2.30	Critical current of a micro-SQUID . . . . .	79
2.31	Fabrication process of micro-SQUIDs . . . . .	84
2.32	Micro-SQUID measurement setup . . . . .	85
2.33	Micro-SQUID measurement for perpendicular magnetic field . . . . .	87
2.34	Micrograph with deployed magnet on a micro-SQUID . . . . .	88

2.35	Hysteresis measurement on micro-SQUID in in-plane magnetic field . . . . .	89
3.1	Band structures of HgTe, CdTe and their ternary compound $\text{Hg}_{0.32}\text{Cd}_{0.68}\text{Te}$ . . .	94
3.2	Progression of subbands depending on QW width . . . . .	96
3.3	Comparison of band structures derived by Kane model and effective model . . .	97
3.4	Manifestations of Dirac cones in condensed matter . . . . .	100
3.5	Illustration of a magnetic field sweep and gate voltage sweep by means of a calculated LL fan chart . . . . .	103
3.6	Quantum Hall measurements on samples close to $d_c$ . . . . .	106
3.7	$\sigma_{xy}$ and $\rho_{xx}$ measurements for the zero-gap sample at two magnetic field . . . .	108
3.8	Progression of $\sigma_{xy}$ and its derivative yielding a contour plot . . . . .	109
3.9	Contour plot of $\partial\sigma_{xy}/\partial E$ with calculated LL dispersions . . . . .	110
3.10	SdH measurements and corresponding DOS aside factor N depending on gate voltage . . . . .	112
3.11	Zero-field conductivity at Dirac point . . . . .	114
3.12	Investigation of longitudinal conductance of quasi one-dimensional transport on HWAL1.1 . . . . .	117
3.13	Longitudinal conductance of 300 nm and 500 nm HgTe-channel . . . . .	119
3.14	Universal conductance fluctuations for sample HWAL1.1 . . . . .	121
3.15	Temperature dependent UCF on HWAL1.1 . . . . .	123
3.16	Various electron paths from point A to point B with one path exhibiting a self crossing point X. . . . .	125
3.17	$\delta\sigma_{xx}$ in $e^2/h$ on HWAL1.1 for various temperatures . . . . .	130
3.18	Evolution of the weak anti-localization peak in temperature sweeps . . . . .	131
3.19	Conductance of sample HWAL2 for an in-plane magnetic field . . . . .	132
3.20	Measurements on sample HWAL2 for $T = 4.2 K$ . . . . .	133
3.21	Dose test and SEM micrographs for sample HWAL3 . . . . .	135
3.22	$\sigma_{xx}$ , mobility and carrier concentration of HWAL3 . . . . .	136
3.23	Analysis of the WAL peak on sample HWAL3 . . . . .	137
3.24	Temperature dependence of (a) $\delta\sigma$ and (b) FWHM for several gate voltages. . .	137
3.25	Sample design of HWAL4 . . . . .	138
3.26	Measurements on HWAL4 at 4.2 K . . . . .	140
3.27	Characterization of sample HWAL5 . . . . .	141
3.28	Analysis of the WAL peak on HWAL5 . . . . .	142
3.29	Comparison of $\delta\sigma_{xx}$ for HWAL3, 4 and 5 . . . . .	143

# List of Tables

2.1	Signal height, noise and signal to noise ratio at room temperature and 4.2 K for samples InAs3.2 and InAs4 . . . . .	65
2.2	The sensitivity of the two sensors for $T = 4.2$ K . . . . .	90
3.1	Samples used for WAL investigations . . . . .	128
3.2	Comparison of mobilities for wide and narrow Hall bars of the same material ( $V_G = 0$ V). . . . .	143
A.1	Macro Hall bar process on InAs 2DEG stack. . . . .	146
A.2	Micro-Hall bar-process on InAs-2DEG stack. . . . .	147
A.3	Macro Hall bar process on HgTe 2DEG stack for characterization. . . . .	148
A.4	Micro-Hall bar-process on HgTe-2DEG stack. . . . .	150
A.5	Micro-SQUID-process on doped Si-substrate. . . . .	151
B.1	InAs substrates used within this thesis. . . . .	153
B.2	InAs samples used within this work. . . . .	153
B.3	HgTe growth parameters . . . . .	154
B.4	HgTe samples used within this thesis . . . . .	154
C.1	Parameters of ferromagnets . . . . .	155

## Publications:

- B. Büttner, C. X. Liu, G. Tkachov, E. G. Novik, C. Brüne, H. Buhmann, E. M. Hankiewicz, P. Recher, B. Trauzettel, S. C. Zhang, and L. W. Molenkamp, *Single valley Dirac fermions in zero-gap HgTe quantum wells* Nature Physics, **7**, 418 (2011), doi: 10.1038/nphys1914
- G. Tkachov, C. Thienel, V. Pinneker, B. Büttner, C. Brüne, H. Buhmann, L. W. Molenkamp, and E. M. Hankiewicz, *Backscattering of Dirac Fermions in HgTe Quantum Wells with a Finite Gap*, Physical Review Letters, **106**, 076802 (2011)
- B. Büttner, R. Schaller, G. Tkachov, E. M. Hankiewicz, C. Brüne, H. Buhmann, and L. W. Molenkamp, *Band inversion effect on weak anti-localization in HgTe quantum wells*, to be submitted

## Conference talk

- B. Büttner, F. Lochner, C. Brüne, C. Gould, G. Schmidt, L. W. Molenkamp, *Micro-Hall Magnetometry for the Investigation of Magnetic Nanoparticles*, Spring conference of the DPG, Berlin, 2008

# Acknowledgements

The results of the research presented within this thesis would not have been possible without the help of many other people. That is why I want to thank everyone who supported me and contributed in one way or another to this work:

- Prof. Laurens W. Molenkamp, head of the EP3, for giving me the opportunity to work in his chair and use the excellent equipment in the clean room and laboratories. Also for various discussions, leading towards new ideas and experiments.
- Prof. Georg Schmidt, Prof. Hartmut Buhmann and Dr. Charles Gould for supervising me and for always being ready to discuss experiments and develop new ideas and, at the same time, permitting me to work independently on the projects.
- Georg Große-Bölting for his work on MHM, Martin Batzer for his enthusiastic work on micro-SQUIDs, Felicitas Gerhard for the detailed investigations on the zero-gap sample, and Nicolas Raab for measuring WAL on the normal quantum well.
- Alena Astakhova for numerous theoretical calculations, CX Liu, G. Tkachov, E. Hankiewicz, P. Recher and B. Trauzettel for giving me deep insights into the theory and fruitful discussions.
- Andreas Riegler, my office mate, for numerous scientific and non-scientific discussions and the great atmosphere in the office. Florian Lochner, for supplying the InAs 2DEGs and helping me as an IT administrator.
- Volkmar Hock, the clean room wizard, for introducing me into the depths of semiconductor processing, and for many helpful advices. Tatiana Borzenko for teaching me all the specifics about electron beam lithography.
- Katrin Pappert, for many instructive discussions. Her, Markus König, Ralf Scheibner and many former PhDs for setting up the the transport labs and teaching me how to use the equipment.
- Stefan Mark, Radu-Gabriel Dengel, and Michael Rütth for the great teamwork in the lab and the clean room.
- Christoph Brüne, for supplying the HgTe-2DEGs. Him, Andreas Roth, Mathias Mühlbauer and Holger Thierschmann for insightful discussions and collaborations.

- Utz Bass, Petra Fries, Claus Schumacher, Michael Leufgen, Michael Lentze, Markus Michelfeit, and Prof. Jean Geurts for the entertaining coffee sessions, widening the perspective within and beyond physics.
- Roland Ebert for the assembly of the cryostat and for the extensive help with all questions about cryogenics. Him and G. Manger for the supply of liquid helium.
- Paula Römer-Roche for her caring support and for her understanding when I had so little time. Her and Christina Voll for being so patient and thorough in proof reading in a subject so far away from their fields.
- Last but not least, my parents for supporting me my entire life. Thanks for their understanding and encouragement during this - not always easy - time.



# Lebenslauf

Bastian Büttner

geboren am 23. Juli 1979 in Bad Neustadt an der Saale

- 1986 bis 1990 Besuch der Grundschule Bad Neustadt an der Saale
- 1990 bis 1999 Besuch des Rhön-Gymnasiums Bad Neustadt an der Saale  
Abschluß Abitur
- 1999 bis 2000 Zivildienst als Rettungsdiensthelfer beim Bayerischen Roten Kreuz
- 2000 bis 2006 Studium Nanostrukturtechnik an der  
Julius-Maximilians-Universität, Würzburg  
Abschluss Diplom-Ingenieur
- 2006 bis 2010 Doktorand am Lehrstuhl EP3 (Prof. L. W. Molenkamp)  
der Julius-Maximilians-Universität, Würzburg
- seit 2010 wissenschaftlicher Mitarbeiter bei der Fachgruppe  
Nanostrukturierte Materialien (Prof. G. Schmidt)  
der Martin-Luther-Universität Halle-Wittenberg

Ehrenwörtliche Erklärung  
gemäß §6 Abs. 3 und 5  
der Promotionsordnung der  
Fakultät für Physik und Astronomie  
der Universität Würzburg

Hiermit erkläre ich ehrenwörtlich, daß ich die Dissertation selbständig und ohne Hilfe eines Promotionsberaters angefertigt und keine weiteren als die angegebenen Quellen und Hilfsmittel benutzt habe.

Die Dissertation wurde bisher weder vollständig noch teilweise einer anderen Hochschule mit dem Ziel, einen akademischen Grad zu erwerben, vorgelegt.

Am 10. März 2006 wurde mir von der Julius-Maximilians-Universität Würzburg der akademische Grad 'Diplom-Ingenieur Nanostrukturtechnik' verliehen. Weitere akademische Grade habe ich weder erworben noch versucht zu erwerben.

Würzburg, den 16.03.2012

Bastian Büttner